Tiago Jorge Ferreira

Licenciado em Ciências da Engenharia Química e Bioquímica

Hybrid Ionic Liquids/Metal Organic Frameworks for CO_2/CH_4 Separation

Dissertação para a obtenção do Grau de Mestre em Engenharia Química e Bioquímica

Orientador: Doutora Isabel A. A. C. Esteves, Investigadora Auxiliar, FCT-UNL

Co-orientador: Doutor José M. S. S. Esperança, Investigador Principal, FCT-UNL

Co-orientador: Doutor Rui P. P. L. Ribeiro, Investigador Pós-Doc, FCT-UNL

Presidente: Doutor Mário Fernando José Eusébio, Professor Auxiliar, FCT-UNL
Arguente: Doutor José Paulo Barbosa Mota, Professor Catedrático, FCT-UNL
Vogal: Doutora Isabel A. A. C. Esteves, Investigadora Auxiliar, FCT-UNL

FACULDADE DE CIÊNCIAS E TECNOLOGIA
UNIVERSIDADE NOVA DE LISBOA

Outubro 2017

Tiago Jorge Ferreira

Licenciado em Ciências da Engenharia Química e Bioquímica

Hybrid Ionic Liquids/Metal Organic Frameworks for CO_2/CH_4 Separation

Dissertação para obtenção do Grau de Mestre em Engenharia Química e Bioquímica

Orientador: Doutora Isabel A. A. C. Esteves, Investigadora Auxiliar, FCT-UNL

Co-orientador: Doutor José M. S. S. Esperança, Investigador Principal, FCT-UNL

Co-orientador: Doutor Rui P. P. L. Ribeiro, Investigador Pós-Doc, FCT-UNL

Presidente: Doutor Mário Fernando José Eusébio, Professor Auxiliar, FCT-UNL
Arguente: Doutor José Paulo Barbosa Mota, Professor Catedrático, FCT-UNL
Vogal: Doutora Isabel A. A. C. Esteves, Investigadora Auxiliar, FCT-UNL

Outubro 2017

Agradecimentos

"*This is the end, beautiful friend*", já dizia o vocalista de uma das bandas mais famosas dos anos 60. Quem me conhece sabe que a minha pessoa não abre "as portas" facilmente, preferindo estranhar, para depois entranhar. Que é como quem diz que eu normalmente não me dou bem com as pessoas que não conheço, logo à primeira. Se é complexo, se é personalidade, não sei... Não considero ter especial jeito para agradecimentos, mas tentarei o meu melhor!

Esta tese de mestrado começou a 6 de Fevereiro deste ano. Desde então passaram 6 meses de trabalho, trabalho esse que fiz da melhor maneira possível e de que me orgulho. Esta aventura não teria sequer um início, se não fosse pelos meus orientadores. Por me terem aceitado para trabalhar neste tema, pela excelente e profissional orientação que me deram, pela elevada exigência requerida, pelas críticas construtivas e correções feitas, pelas conversas sobre a temática, pelas trocas de ideias, pela disponibilidade e acompanhamento do trabalho e também pela paciência revelada, quero deixar aqui o meu agradecimento especial à Doutora Isabel Esteves e aos Doutores José Esperança e Rui Ribeiro. Gostava de enveredar na área da investigação científica e esta experiência foi bastante motivadora para querer seguir esse caminho.

Um grande obrigado ao Mestre André Portela que, embora já não se encontre a trabalhar no grupo, me ajudou a dar os "primeiros passos", na medição de equilíbrios de adsorção e também na integração no grupo que, também graças a ele, ocorreu de forma mais tranquila e natural do que eu esperava. A sua ajuda e companheirismo sinto que foram inestimáveis. E, embora já lhe tenha dito isto pessoalmente, quero reforçar aqui o meu desejo de um excelente futuro profissional e pessoal. Um grande abraço.

Também quero agradecer à minha colega Vera Pessoa, que me ajudou numa fase inicial na preparação de alguns dos materiais alvos de estudo nesta tese e também me acompanhou em algumas medições de equilíbrio de adsorção.

Fica também aqui uma palavra de apreço aos meus companheiros de laboratório Elena Surra, Abimaelle Chibério, Inês Ferreira, Ana Martins e Pedro Melo pela boa-disposição e companheirismo no tempo passado no laboratório.

Um importante agradecimento tem de ser feito aqui ao técnico superior Nuno Costa. Sem ele, a caracterização textural dos materiais estaria certamente incompleta. Obrigado também pela paciência demonstrada, visto que o "chateei" várias vezes por causa dos resultados dessas caracterizações, pela ajuda na feitura das minhas primeiras pastilhas de FT-IR e pelo esclarecimento de dúvidas específicas sobre detalhes das técnicas de caracterização.

Quero agradecer também à Doutora Małgorzata Zakrzewska, do grupo de investigação do Professor Manuel Nunes da Ponte, por ter facultado um dos líquidos iónicos utilizados para este trabalho ($[C_6MIM][B(CN)_4]$).

Porque a realização desta tese é o culminar de um percurso de 5 anos, quero agradecer aos meus amigos já conhecidos antes da chegada a esta faculdade bem como aos que fiz aqui. Um obrigado aos meus amigos Beatriz de Moura, David Lopes, Rui Ribeiro e Rita Domingos pelas trocas de ideias e discussões relativas à temática da tese; ao Daniel Brízido, Diogo Boto e José Dias pelo interesse manifestado pelo tema da minha tese, apesar seguirem cursos bem diferentes da Engenharia Química.

Por ordem alfabética, fica também um obrigado à Ana Cortes, à Beatriz Nobre, à Bianca Visveshcumar, à Catarina Araújo, à Clarinda Costa, à Diana Kharina, à Filipa Marques, à Jessica Costa, à Margarida Freixo, à Mariana Liberal, à Mónica Cunha, à Neide Gomes, ao Pedro Mendes e à Sara Sequeira pela entreajuda, pelas conversas, pelos almoços, pelos momentos de boa-disposição, pela companhia, pelos trabalhos realizados com vocês, pelo tempo passado nesta faculdade. O vosso carinho e as vossas distintas (maneiras de ser) personalidades continuarão a ser por mim apreciadas.

Quero deixar uma nota de apreço muito especial à Daniela Agostinho. Tu sabes porquê... Conheci pessoas únicas neste curso, mas o carinho que nutro por ti não tem comparação. Não preciso de dizer mais nada. Obrigado pela companhia no piso 5 do Edifício Departamental, durante estes meses.

Também à minha família, que se encontra maioritariamente na Madeira: um muito obrigado à minha avó, aos meus primos, primas, tios e tias pela vossa preocupação, carinho e por me fazerem crescer como pessoa.

O meu último agradecimento vai para os meus pais. E a eles há muitas coisas para agradecer... Os sacrifícios que fizeram por mim, aos mais diversos níveis são indescritíveis e eu sou um sortudo por ter dois pais com diferentes, embora complementares, personalidades. O meu mundo muda com as vossas palavras, com as vossas memórias, com as vossas experiências e, acima de tudo, com as vossas ideias e formas de ver o mundo. Ainda bem que me têm proporcionado a possibilidade de ver e conhecer novos locais, novas culturas, tornando-me mais cidadão do mundo. Não há como agradecer isto. Amo-vos.

E embora não seja pessoa de andar a citar frases, dado o carácter pessoal dela, acabo esta secção com uma frase dita pela pessoa que mais me frustra e que simultaneamente não cessa de me surpreender: “deve ser nossa obrigação zelar pela perfeição”.

Dedicatória

Dedico esta tese de mestrado aos meus pais por tudo o que já fizeram por mim e por tudo o que continuam a fazer por mim no dia-a-dia.

Resumo

Nesta tese produziram-se nove novos materiais compósitos de ZIF-8, uma rede organometálica porosa (MOF), impregnado com diferentes líquidos iónicos (ILs). Estes novos compósitos, designados genericamente por IL@ZIF-8, foram preparados e caracterizados com o objetivo de serem considerados potenciais adsorventes a aplicar em processos de separação por adsorção, tais como o *upgrading* ou condicionamento de biogás a biometano.

Numa primeira fase, a mesma quantidade molar de nove ILs diferentes foi incorporada na estrutura do ZIF-8, garantindo uma comparação válida entre as amostras. O efeito da incorporação do IL na capacidade de adsorção dos materiais compósitos foi estudado, bem como a influência do catião e do anião do IL na capacidade de adsorção de CO_2 (dióxido de carbono) e CH_4 (metano) e respetivo efeito na seletividade ideal CO_2/CH_4.

A caracterização textural exaustiva a cada material compósito foi feita com recurso a picnometria de He, adsorção-dessorção de N_2 a 77 K, difração de raios-X de pó (PXRD), espectroscopia de infravermelho com transformada de Fourier (FT-IR) e microscopia eletrónica de varrimento (SEM).

Os resultados de equilíbrio de adsorção-dessorção de CO_2 e CH_4 nos compósitos mostram que o catião imidazólio com uma curta cadeia alquílica favorece a capacidade de adsorção para estes materiais. No entanto, quem tem um papel mais ativo de adsorção de gás é o anião e o melhor daqueles que foi testado é o acetato.

Em termos de seletividade ideal CO_2/CH_4, em traços gerais, as amostras que capturaram menos gás são as mais seletivas. O compósito C10@ZIF-8 é o material mais seletivo entre 1 e 3 bar; de 4 a 16 bar, C2OH@ZIF-8 é o material mais seletivo, com ganhos médios de quase 25% na seletividade em comparação com o ZIF-8 puro. O compósito C6B(CN)4@ZIF-8 apresenta boa capacidade de adsorção de gás, tendo ao mesmo tempo uma boa seletividade CO_2/CH_4. O efeito da quantidade de IL impregnada (*loading*) foi também estudado. Novas amostras C2OH@ZIF-8 e C6B(CN)4@ZIF-8 foram produzidas com diferentes *loadings* e caraterizadas com as mesmas técnicas anteriormente mencionadas. Os resultados obtidos de equilíbrio de adsorção para estas amostras foram inconclusivos.

Este trabalho abre assim as portas para um campo de investigação de novos materiais com resultados potencialmente interessantes em aplicações de adsorção, dada a multitude de ILs e MOFs existentes.

Palavras-chave: impregnação com IL, materiais IL@ZIF-8, adsorção, *upgrading* de biogás

Abstract

For this thesis nine new composite materials of ZIF-8, a porous organometallic network (MOF), impregnated with different ionic liquids (ILs) were produced. These new composites, generically named IL@ZIF-8, were prepared and characterized with the purpose of studying their potential use as adsorbents in adsorption separation processes such as biogas upgrading or biogas to biomethane conditioning.

Firstly, the same molar amount of nine different ILs was incorporated in ZIF-8 structure, assuring a valid comparison among samples. IL impregnation effect on the adsorption capacity of the composite materials was studied, as well as the influence of the cation and anion of the IL on the adsorption capacity of CO_2 (carbon dioxide) and CH_4 (methane) and respective effect on ideal CO_2/CH_4 selectivity.

An exhaustive textural characterization was performed for every composite, such as He pycnometry, N_2 adsorption-desorption at 77 K, Powder X-Ray Diffraction (PXRD), Fourier Transform Infrared Spectroscopy (FT-IR) and Scanning Electron Microscopy (SEM).

CO_2 and CH_4 adsorption-desorption equilibria results indicate that the imidazolium cation with shorter alkyl chains favours the adsorption capacity for these materials. However, it is the anion that has the key role in adsorption capacity; of all tested, the best one was acetate.

Generally speaking, CO_2/CH_4 ideal selectivities show that samples with less adsorption capacity are the most selective. C10@ZIF-8 composite is the most selective material between 1 and 3 bar; from 4 to 16 bar, C2OH@ZIF-8 is the most selective material, with average gains of almost 25% in selectivity when compared to pristine ZIF-8. C6B(CN)4@ZIF-8 presents good gas adsorption capacity, while at the same time showing good ideal CO_2/CH_4 selectivity.

IL loading effect was also tested, with new C2OH@ZIF-8 and C6B(CN)4@ZIF-8 samples with different loadings being manufactured and texturally characterized by the above-mentioned techniques. Adsorption equilibria results for these new samples were inconclusive.

This thesis opens new possibilities for the manufacture of good and selective adsorbent materials for adsorption applications, given the amount of existing MOFs and ILs.

Keywords: IL impregnation, IL@ZIF-8, adsorption, biogas upgrading

List of Contents

List of Figures

List of Tables

List of Abbreviations

ARE – Average Relative Error

CCS – Carbon Capture and Storage

CFC – Chlorofluorocarbon

EDS – Energy-Dispersive X-Ray Spectroscopy

EU – European Union

FT-IR – Fourier Transform Infrared Spectroscopy

GHG – Greenhouse Gas

HDI – Human Development Index

IL – Ionic Liquid

IL@MOF – Ionic Liquid impregnated in a MOF

IL@ZIF-8 – Ionic Liquid impregnated in ZIF-8

IUPAC – International Union of Pure and Applied Chemistry

MOF – Metal-Organic Framework

PSA – Pressure Swing Adsorption

PXRD – Powder X-Ray Diffraction

RTIL – Room-Temperature Ionic Liquid

SEM – Scanning Electron Microscopy

STP – Standard Temperature and Pressure

TGA – Thermogravimetric Analysis

TSA – Temperature Swing Adsorption

USD – United States Dollar

ZIF – Zeolitic Imidazolate Framework

List of Symbols

b – affinity constant

c – BET 'c' constant

c_A – concentration of generic component A

c_{Ai} – concentration of generic component A at the interface

H – Henry's constant

k_G – gas-phase mass transfer coefficient

k_L – liquid-phase mass transfer coefficient

m – weighed mass ('apparent' mass)

m_{abs} – absolute amount adsorbed

$m_{eq\,K}$ – equilibrium K value

m_{exc} – excess amount adsorbed

m_h – mass of sample holder

m_{net} – net amount adsorbed

m_s – mass of the adsorbent sample

MW – molecular weight (of the gas in question)

n – heterogeneity parameter

N_A – flux of generic solute A through phase interface

P – total pressure

p/p_0 – relative pressure

p_A – partial pressure of generic component A

p_{Ai} – partial pressure of generic component A at the interface

P_s – vapour pressure

q – specific amount adsorbed

q_{exc} – specific excess adsorption

q_{net} – specific net adsorption

q_s – maximum specific adsorbed amount

q_t – specific total adsorption

R^2 – coefficient of determination

$S_{CO2/CH4}$ – ideal CO_2/CH_4 selectivity

T_c – critical temperature

V_{cell} – cell volume

V_h – volume of the sample holder

V_p – total pore volume

V_{REF} – reference volume

V_s – solid volume

x_A – mole fraction of generic component A in the liquid phase

x_{Ai} – mole fraction of generic component A in the liquid phase at the interface

y_A – mole fraction of generic component A in the gas phase

y_{Ai} – mole fraction of generic component A in the gas phase at the interface

List of Greek Letters

Θ – scattering angle

ρ_g – density of bulk gas at the equilibrium pressure and temperature

ρ_g – density of bulk gas in the cell volume

ρ_h – density of sample holder

ρ_{REF} – density of bulk gas in the reference volume

ρ_s – density of adsorbent's solid matrix

$\overline{\rho}$ – mean density of liquid phase

1. Introduction

1.1. Motivation

The Mauna Loa Observatory, Hawaii, has been monitoring atmospheric CO_2 concentration since 1958, longer than in any place on the planet, and the first measurements were of 316 ppm [1]. This value is close to the tropospheric concentration of CO_2 before the Industrial Revolution (280 ppm) calculated by T.J. Blasing in 1985 [2]. In May 2013, it was reported that CO_2 levels near the Observatory would soon reach a daily concentration above 400 ppm. Data disclosed from the Mauna Loa Observatory show that, in April 2017, monthly average CO_2 levels were of 409 ppm, higher than the 407 ppm in 2016. Those same data indicate that, since 2016, monthly mean values have been consistently higher than 400 ppm all year long [3].

CO_2 is the main greenhouse gas (GHG) concerning the topic of global warming but other gases, though at lower but rising concentrations on the atmosphere like CH_4, N_2O and CFCs, can also contribute to this phenomenon and, consequently, lead to climate change [2, 4]. GHGs are so called because they allow incoming solar radiation to heat Earth's surface but absorb and re-emit in all directions most of the infrared radiation emitted by the planet's surface. Without these gases, Earth's average temperature would be -18 °C instead of the current 15 °C [5]. In contrast, increasing concentrations of GHGs contribute to global warming.

CO_2 is typically a product of combustion of carbonaceous fuels [6]. Fossil fuels are included in this category and their consumption, along with other sources, is the leading cause for GHGs emission [7]. In 2010, about 85% of the world's energy demand was satisfied by the burning of fossil fuels [8]. In 2014, the burning of fossil fuels dropped to 78% of the world's energy demand due to investment in renewable energy sources [9].

Some indicators relate CO_2 emissions directly with human population. At the time, population is rising, augmenting the energy demand in several sectors of society and increasing the CO_2 emissions [10]. It is worth noting that, even though 2015 and 2016 have been declared 'the warmest years on record' [11, 12], global emissions of CO_2 have had almost no growth since 2014 [13]. Other phenomena, like *El Niño*, can explain the rising of global temperature in 2015 and 2016 [11].

Nevertheless, global emissions are currently above 35 Gton CO_2/year [13]. It comes with no surprise that China, the United States of America, the European Union, India, the Russian Federation and Japan account for more than half of the global emissions of carbon dioxide [11]. These countries, including those who are European Union members, have all medium to very high Human Development Index (HDI) [14], very few are still considered developing countries [15] and they account for more than half of the planet's population, according to World Bank 2015 data [16]. For example China, the main emitter with more than 10 Gton CO_2/year in 2015 [11], is

along with India a newly industrialized country, and the two are the most populated countries on Earth (about 36.5% of human population) [16].

It is all but unexpected that, according to 2010 data, electricity and heat production, along with industry, make up for almost half of GHGs emission when considering the different economic sectors of society. Once agriculture, forestry and other land use are accounted as a whole, these three sectors sum 70% of global GHGs emissions. Transportation, buildings and others make up the rest of the list of GHGs emitting economic sectors [17].

Increasingly releasing GHGs will eventually lead to a chain of events that include global warming with consequent ice melting and oceans' rise. The latter can lead to flooding of low-lying territories which could put populations and biodiversity at risk, causing shore retreat. Other possible consequences are the change in the atmosphere due to warmer seas; warmer, more acid seas results in the loss of numerous life forms; changes in the water and nitrogen cycles can occur; wildfires can happen with more frequency and natural phenomena can be stronger; desertification can be sped up; plant cycles can change and less area for agriculture along with additional water consumption in this particular economic sector can happen, just to name some of them [18, 19]. Some of these changes are already happening with some unwanted frequency.

To attenuate the global and transversal repercussions of Mankind's GHGs emissions, there have been drawn up some utmost important documents regarding climate change since the 1990s. The first one was The United Nations Framework Convention on Climate Change (1992), one of the three 'Rio Convention' adopted, entering into force in 1994 [20]. Its main goal was to 'achieve (…) stabilization of greenhouse gas concentrations in the atmosphere at a level that would prevent dangerous anthropogenic interference with the climate system' [21]. Recognizing that there was a problem pertaining GHGs emissions to the atmosphere, the Kyoto Protocol was signed in 1997, entering into force in 2005. The Protocol set a binding emission reduction targets for its Parties, with developed countries having 'differentiated responsibilities' since they play a bigger role on the GHGs emissions [22]. The Copenhagen Accord came in 2009, endorsing the continuation of the Kyoto Protocol [23]. Finally, in 2015, the Paris Agreement was adopted; 195 countries accepted the document, agreeing to limit the increase of global average temperature below 2 °C [24].

Following what was agreed on the above-mentioned documents or simply due to the increase of awareness on climate change and its risks, several different policies have emerged. One example is the imposition of a tax on the emission of a certain GHG; not only several countries in the EU have already a carbon tax [25], but the impact of fuel or carbon/GHG tax in the United States of America or China is currently being studied [26, 27, 28].

A second strategy is the exploration and investment in renewable energy sources. In 2015, new investment in renewable power and fuels reached 285.9 billion USD, growing 4.7% in regard to 2014. An interesting fact is that China, the United States of America and Japan are the top 3 countries that invested the most in renewable power and fuels; the United Kingdom and India

complete the top 5. Also comparing with 2014, renewable power capacity grew when considering every kind of renewable energy as well as fuel ethanol production, while biodiesel production decreased. China leads in hydropower, solar photovoltaic, wind power and solar water heating capacities while the United States lead the biodiesel and fuel ethanol production. Amongst these renewable energies is biogas, a mixture of mainly CH_4 and CO_2, whose sector has been on an upward trend, with most of it being produced in the United States and in Europe [9]. Though it has a lower percentage of methane than natural gas, it is possible to upgrade (that is, to concentrate) methane in biogas so that it reaches natural gas standards. That can be done using different strategies, one of them being adsorption. Good adsorbents for this purpose would be in contact with an inlet of biogas and the outlet would have higher concentrations of methane, with CO_2 being adsorbed by an adsorbent material.

A third approach adopted is the implementation of CCS (carbon capture and storage) technologies [29]. CCS technologies fall typically in three categories: pre-combustion, post-combustion and Oxyfuel combustion [30]. Separation techniques can be included in one or more capture method and they are absorption/scrubbing (physical or chemical), cryogenic distillation, membranes, gas hydrates, chemical looping, chemical mineral trapping and adsorption [29, 30]. For the latter technique, microporous materials are typically used and then a temperature swing adsorption (TSA) or pressure swing adsorption (PSA) processes are employed [30]. One recent kind of the aforementioned materials are metal-organic frameworks (MOFs). MOFs are metal-organic crystalline materials built from the coordination of a metal ion or cluster linked to organic ligands [31]. Much research has been developed on CO_2 capture/separation with this family of materials [32]. Ionic liquids (ILs) are another kind of materials being used to capture/separate CO_2 with promising results [33]. In the past few years, it was hypothesized that MOFs could be impregnated with ILs, taking advantage of the behaviour of both materials shown in terms of CO_2 capture. The composite material obtained – IL@MOF – presents itself as a relevant case study when considering new materials for CCS or separation of gaseous mixtures [29]. There has been made ground-breaking work about ILs@MOF in terms of computational simulation [34] and creating the composite material itself [35]. Only four articles approach CO_2 adsorption [36].

This thesis' main goal is to open a new window of research in understanding the behaviour of several ILs incorporated in MOF *Zeolitic Imidazolate Framework-8* (ZIF-8; commercial name is Basolite® Z1200 from BASF SE) and to discern the difference in the adsorption capacity and ideal CO_2/CH_4 selectivity of the composite material relative to the pristine ZIF-8. The cation and anion effects of the IL were studied, as well as the effect of IL loading. Through different textural characterization techniques, such as He pycnometry, N_2 adsorption-desorption isotherm at 77 K, PXRD, FT-IR and SEM, it is possible to assess if the impregnation method of ZIF-8 was successful and determine the composite's properties such as pore volume and solid matrix density. Their performance in gas adsorption will point to the most selective composite material and, in a bigger picture, indicate if these proposed materials have potential for gaseous mixtures separation.

1.2. Thesis Structure

This thesis is comprised by five chapters:

- Chapter 1: Introduction

- Chapter 2: Theoretical Background

The chapter addresses the possible gaseous mixtures that can be separated by the composite materials designed in the thesis; the theory related with the phenomena of absorption and adsorption, along with the latest developments in this research field; finally, the methodologies for the adsorption equilibria measurements alongside purification/separation methods of gaseous mixtures are referred.

- Chapter 3: Materials and Methods

In this chapter, a listing of all employed chemical compounds is presented, along with an explanation of all the characterization techniques that were necessary to fully describe the developed composite materials. Also included is an explanation of the two units used for adsorption equilibrium measurements.

- Chapter 4: Experimental results and Discussion

Included in this chapter are the adsorption equilibria results obtained during this thesis as well as their analysis and respective discussions. It also contains data from the different characterization techniques described in Chapter 3. ZIF-8 data are compared with open literature results to evaluate their consistency.

- Chapter 5: Conclusions and future work

Finalizing this thesis is a summary of the work developed and its main conclusions. Suggestions for future work that could optimize the performance of these composite materials are left, as well as the proposal of new adsorption equilibria measurements.

2. Theoretical Background

2.1. Gaseous mixtures

Some gaseous mixtures have a proper designation, such as Mond gas [37], water gas [38], coal (or town) gas [39], syngas [40], and others. From an environmental and/or energetic standpoints, all gaseous mixtures have inherent interest but three of them stand out: flue gas, biogas and natural gas.

Flue gas in a broad sense is any kind of 'exhaust gas from a combustion process' [41] but is considered in the Chemical Engineer domain as mainly a mixture of N_2 (an inert gas that constitutes more than two-thirds of its composition) and CO_2. It also contains particulates, H_2O, O_2 and a small percentage of other gases. CO_2 from these streams is typically captured using amines; this capture method presents several drawbacks such as high energy consumption, cost increases, corrosion problems and degradation of the amines [29, 42]. Therefore, the need for new competitive capture systems [43] and impurities removal methods [44] is topical.

Biogas, a product of the anaerobic decomposition of organic matter, has in its composition 55 to 70% CH_4, 30 to 45% CO_2, small amounts of NH_3, H_2S and hydrocarbons. It may also contain H_2O, dust particles, siloxanes and trace amounts of other gases [45]. Due to the rapid development of biofuels, biogas is in a upward trend [46] that is reflected on the number of scientific papers published (according to a ScienceDirect search, 2011 saw 1690 articles about this topic, while in 2016 more than twice that number were found, totalling 3498 articles), on the number of Master's thesis regarding this subject [47, 48] and in the actual market. Biogas is, as flue gas, purified via amine absorption [49]. Therefore, new materials for CO_2 capture/separation can lead to a purer stream of CH_4 (biogas upgrading), bringing it to natural gas standards, that can posteriorly be used as an alternative fuel to petrol and diesel [50].

Lastly, natural gas resembles somewhat the composition of biogas with CH_4 composition around 75-90%, noteworthy amounts of C_2H_6, C_3H_8 and C_4H_{10}, 1-3% of other higher hydrocarbons along with impurities like H_2O, CO_2, N_2 and H_2S [51]. Again, amines are employed for CO_2 removal and the search for new materials and/or separation processes are being investigated. Currently, membrane technology is being tested [52] and shows improvements when compared to amines absorption. Imidazolium-based ILs are also being tested as materials capable of efficiently removing CO_2 [53].

2.2. Gas Absorption

2.2.1. Fundamentals

The term absorption used in Chemical Engineering refers to a unit operation where a gaseous mixture is contacted with an absorbent liquid so that one or more components of the mixture (absorbate) is dissolved into the liquid [54]. It is an alternative to distillation for the separation of low molar mass materials [55] and, as described, mass transfer occurs from the gas stream to the liquid (see Figure 2.1.). If mass transfer happens from the liquid stream to the gas, with liquid components separated through gas contact, the operation is called stripping [54]. Both operations are usually used for gas purification, production of gas solutions and product recovery [56].

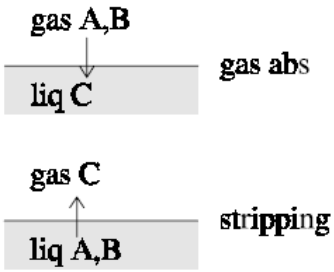

Figure 2.1. Mass transfer of generic component A in absorption and stripping operations [57].

Depending on the nature of the interactions established between absorbent and absorbate, the operation of absorption can be divided in three categories [58]:

- Physical solution: the absorbed component is more soluble in the liquid absorbent than the other gases in which it is mixed. In this case, the equilibrium concentration in the liquid phase is mainly a function of the partial pressure in the gas phase. An example of this kind of absorption is the recovery of light hydrocarbons from oil;
- Reversible reaction: a chemical reaction occurs between a component in the gas phase and a component in the liquid phase, forming a compound which will exert a substantial vapour pressure of the absorbed component. An example is the absorption of carbon dioxide making use of a monoethanolamine solution;
- Irreversible reaction: an essentially irreversible chemical reaction occurs between a component of the gas phase and a component of the liquid phase. The compound formed exerts negligible vapour pressure on the absorbed component. An example is the absorption of ammonia by sulphuric acid solution, forming ammonium sulphate.

The physical fundamentals essential to the absorption process are the solubility of the absorbed gas and the mass transfer rate [56].

At equilibrium, a component of a gaseous mixture in contact with a liquid has identical fugacities in both phases. Therefore, considering ideal solutions, Raoult's law can be applied, as described in Equation 2.1.

$$y_A = \frac{P_s}{P} x_A \qquad (\text{Eq. 2.1.})$$

with y_A as the mole fraction of generic component A in the gas phase, P_s as the vapour pressure, P as the total pressure and x_A as the mole fraction of generic component A in the liquid. If a gas component is moderately soluble but has little to none interaction between gas and liquid phases, Henry's law can be applicable, as described in Equation 2.2.

$$y_A = \frac{H}{P} x_A \qquad (\text{Eq. 2.2.})$$

with H as Henry's constant. Comparing Equations 2.1. and 2.2., it is easy to reach Equation 2.3.

$$y_A = m_{\text{eq K}}\, x_A \qquad (\text{Eq. 2.3.})$$

with $m_{\text{eq K}}$ as equilibrium K value, used to represent hydrocarbon vapor-liquid equilibria in absorption as well as distillation.

When Equation 2.1. or 2.2. is valid at constant temperature and pressure (the equivalent to constant m in Equation 2.3.), a plot of y=f(x) for a solute is linear from the origin. In other cases, this plot has a linear relationship over a limited region. Normally, for non-ideal solutions or non-isothermal conditions, a curving relationship between y and x is observed. When applied to an absorber design, this plot is usually called the equilibrium line.

One must not forget, for designing purposes, the rate at which the solute is transferred from the gas to the liquid phase. One of the first theoretical models describing the absorption phenomena proposed a gas-liquid-interface; at a certain distance from this interface, large fluid/bulk motions are assumed to exist distributing material rapidly and in equal manner so that no concentration gradients are formed. However, closer to the interface, the fluid motions are diminished and slow process of molecular diffusion becomes the most relevant mechanism of mass transfer, following Fick's first law. So, the rate-governing step of the absorption phenomena is the transfer of solute through the gas and liquid films contiguous to the phase interface.

The existence of these films is a premise of the mentioned theoretical model that tried to explain and correlate experimentally measured mass transfer coefficients, the film theory (proposed by Walter G. Whitman in 1923 [59]); it is considered the classical model that tries to approximate the real situation at the interface by having hypothetical 'effective' gas and liquid films [56]. It is an inaccurate representation of the conditions at the gas-liquid interface, but has proved itself to be a useful correlation tool for the design of absorption and stripping equipment [58]. Its assumption is that gas and liquid are in equilibrium at the interface and that thin films separate the interface from the bulk of the two phases.

A comparison between the actual situation at the interface and the film theory is diagrammatically presented in Figure 2.2.

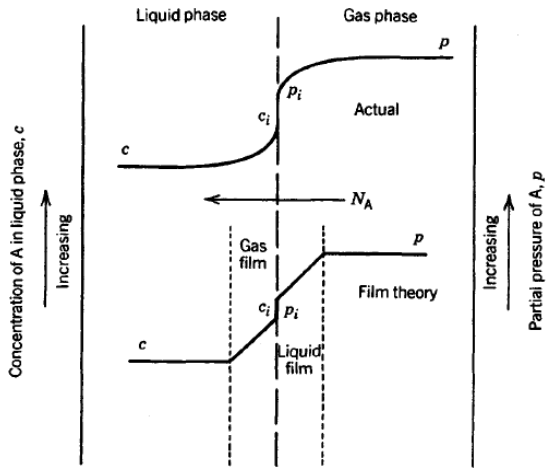

Figure 2.2. Difference between the actual mass transfer in absorption and film theory concept [58].

If a non-flowing closed system is considered, with the passage of time, a concentration profile would become straight horizontal since bulk gas and bulk liquid reached equilibrium. But in a flowing system, as liquid and gas pass each other, the bulk materials don't have the necessary contact time to reach equilibrium (e.g., at a certain height in an absorption tower working in counter-current conditions). Solute is therefore continuously transferred from the gas to the liquid phase and concentrations gradients appear when mass transfer takes action, only at a finite rate.

The rate equations for the gas and liquid films (Equation 2.4. and 2.5., respectively) show a direct proportion between said rate and the displacement from equilibrium.

$$N_{\mathrm{A}} = k_{\mathrm{G}}(p_{\mathrm{A}} - p_{\mathrm{Ai}}) = k_{\mathrm{G}} P(y_{\mathrm{A}} - y_{\mathrm{Ai}}) \qquad (\mathrm{Eq.\,2.4.})$$

$$N_{\mathrm{A}} = k_{\mathrm{L}}(c_{\mathrm{Ai}} - c_{\mathrm{A}}) = k_{\mathrm{L}}\bar{\rho}(x_{\mathrm{Ai}} - x_{\mathrm{A}}) \qquad (\mathrm{Eq.\,2.5.})$$

with N_A as the flux of generic solute A through phase interface, k_G as gas-phase mass transfer coefficient, p_A as partial pressure of generic component A, p_{Ai} as partial pressure of generic component A at the interface, y_{Ai} as mole fraction of generic component A in the gas phase at the interface, k_L as liquid-phase mass transfer coefficient, c_{Ai} as concentration of generic component A at the interface, c_A as concentration of generic component A, $\bar{\rho}$ as mean density of liquid phase and x_{Ai} as mole fraction of generic component A in the liquid at the interface. Both equations are composed of mass transfer coefficients (k_G and k_L for gas and liquid phases, respectively) and the associated driving force, which is $y_A - y_{Ai}$ and $x_{Ai} - x_A$ for gas and liquid phases, respectively.

Figure 2.3. has a representation of various concentrations and driving forces in a *y*=f(*x*) diagram. The point that represents the interfacial concentrations ($x_{\mathrm{Ai}}, y_{\mathrm{Ai}}$) must be part of the equilibrium curve because those two concentrations are at equilibrium. The point representing the bulk concentrations ($x_{\mathrm{A}}, y_{\mathrm{A}}$) can be anywhere above the equilibrium line for absorption and below said curve for stripping. The slope tie line (Equation 2.6.) connecting these two points is given by Equations 2.4. and 2.5.

$$\frac{y_{\mathrm{A}} - y_{\mathrm{Ai}}}{x_{\mathrm{A}} - x_{\mathrm{Ai}}} = -\frac{k_{\mathrm{L}}\bar{\rho}}{k_{\mathrm{G}}P} \qquad (\mathrm{Eq.\,2.6.})$$

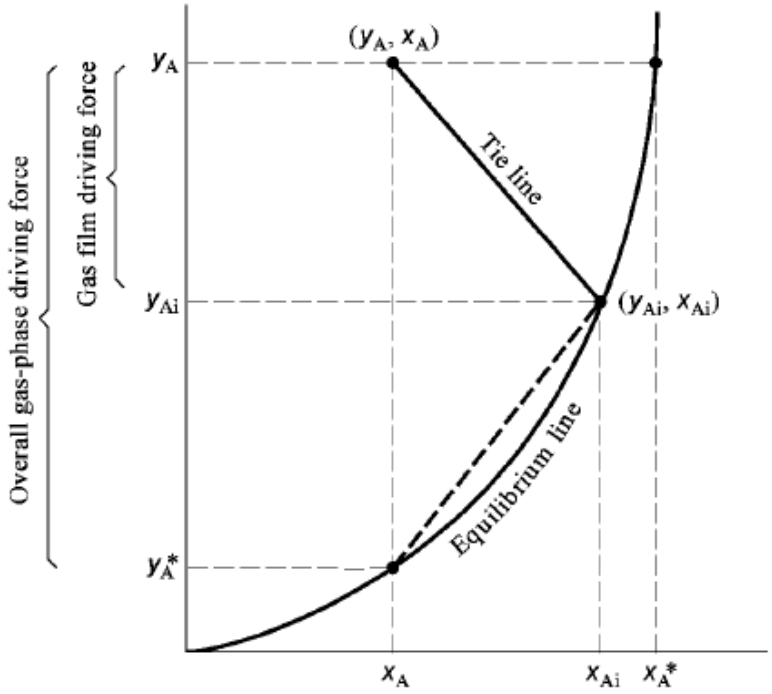

Figure 2.3. Equilibrium curve and driving forces in absorption phenomenon [56].

Relevant variables for the absorption (and stripping) process are temperature, pressure and liquid flowrate [55]. The following analysis of the effect of one of these degrees of freedom assumes that the other two are kept constant.

An increase in temperature will decrease the absorbate's solubility in the absorbent [55], as highlighted in Figure 2.4. Absorption consequently is an exothermic process.

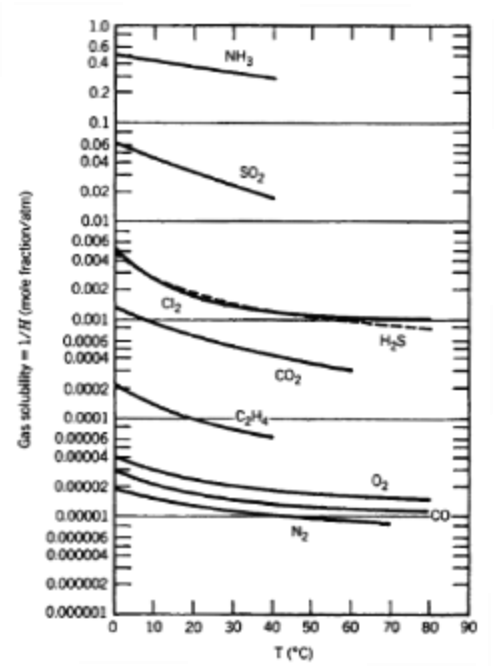

Figure 2.4. Solubility of some gases in water. Here, solubility is expressed as the reciprocal of Henry's law constant [58].

An increase in pressure grants a greater solubility of the absorbate in the liquid phase. There is a practical optimal pressure since high pressures are expensive to generate, due to the energy consumption of the gas compressor [55]. Figure 2.5. illustrates how CO_2 and CH_4 solubilities increase in an IL due to pressure increment.

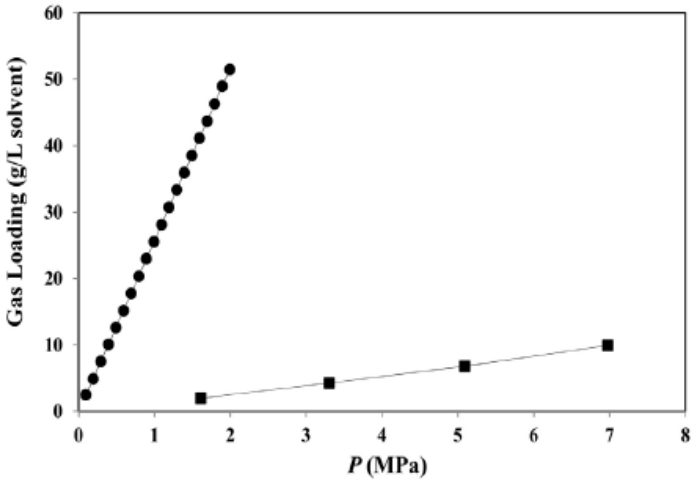

Figure 2.5. Solubility of CO_2 (circles) and CH_4 (squares) at 50 °C in 1-hexyl-3-methylimidazolium tricyanomethanide [60].

Lastly, an increase in the liquid flowrate will lead to an increase in gas absorption. This happens due to the increased interfacial area, which is related to the absorbent's flowrate. An increase in the interfacial area leads to an increase in mass transfer coefficients because a higher contact area between the two phases is available. Figure 2.6. shows the influence of both absorbent's flowrate and pressure in absorption rate whilst Figure 2.7. displays the influence of the same two variables on the percentage of CO_2 absorbed.

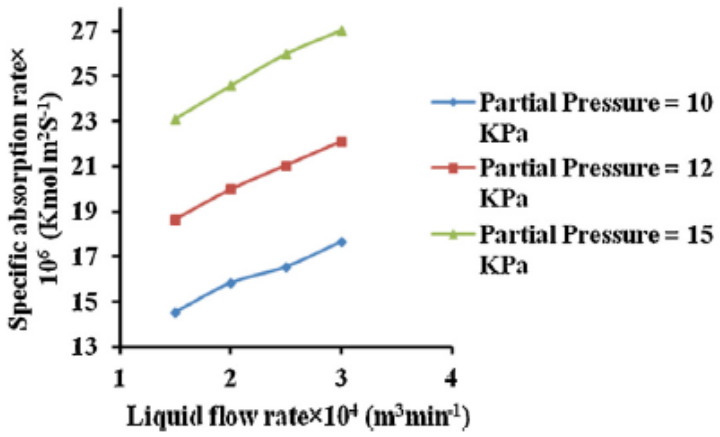

Figure 2.6. Effect of liquid flowrate and pressure on the absorption rate [61].

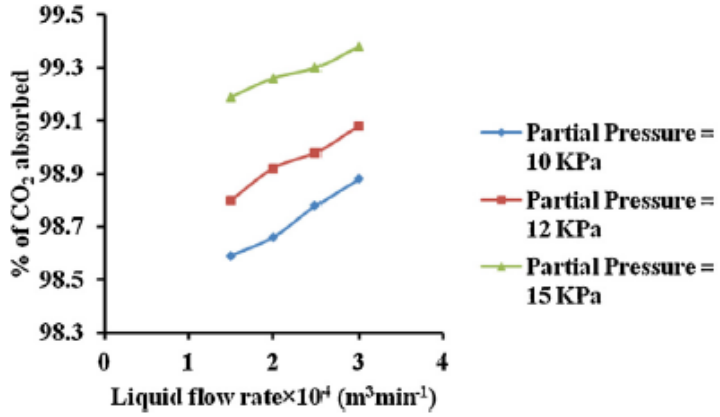

Figure 2.7. Effect of liquid flowrate and pressure on the percentage of CO_2 absorbed [61].

Gas flowrate could also be considered an important variable for gas absorption. Just like liquid flowrate, an increase in gas flowrate leads to higher mass transfer coefficients. Whilst an increment in gas flowrate prompts an increase in the absorption rate, it also causes a decrease in the gas phase resistance. Overall, an increase in gas flowrate has an increasing, but globally flat, effect on absorption rate, as depicted in Figure 2.8.

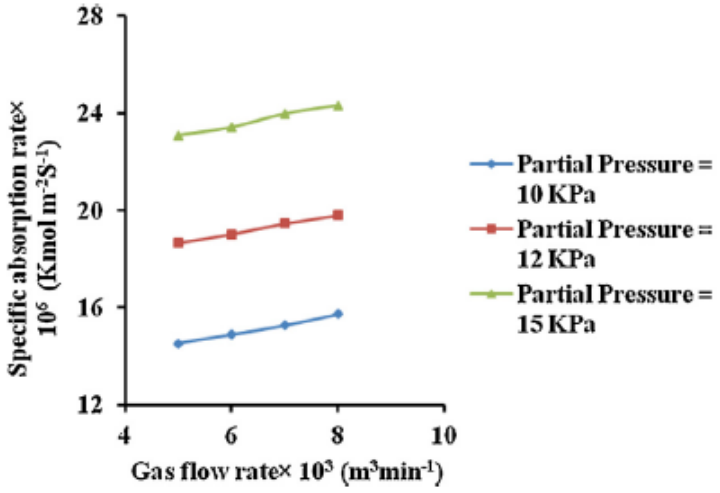

Figure 2.8. Effect of gas flowrate and pressure on absorption rate [61].

2.2.2. Absorbents

Gas absorption is always possible with any absorbent-absorbate pair, since the gas phase will always be, no matter how low, soluble in the liquid phase. The chemical industry has several combinations of absorbent-absorbate for several applications, listed in Table 2.1.

Table 2.1. Absorbent/absorbate systems commonly employed in the chemical industry [56].

Treated gas	Absorbed gas	Absorbent	Function
Coke oven gas	NH_3	H_2O	By-product recovery
Coke oven gas	Benzene and toluene	Straw oil	By-product recovery
Reactor gases in manufacture of formaldehyde from methanol	Formaldehyde	H_2O	Product recovery
Drying gases in cellulose acetate fibre production	Acetone	H_2O	Solvent recovery
Refinery gases	H_2S	Alkaline solutions	Pollutant removal
Products of combustion	SO_2	H_2O	Pollutant removal
Products of combustion	CO_2	Ethanolamines	By-product recovery
Ammonia synthesis gas	CO	Ammoniacal cuprous chloride solution	Contaminant removal
Roast gases	SO_2	H_2O	Production of calcium sulfite solution for pulping

- **Ionic Liquids (ILs)**

Among the novel alternative materials for CO_2 capture, ILs have shown great potential in this area of study. They can be used as solvents and employed in various applications, such as gas purification [29]. ILs are a subset of molten salts; the latter are salts that are in the solid state at STP conditions (0 °C, 1 bar), but enter the liquid state at elevated temperatures, whereas the former are any kind of molten salts that melt below 100 °C. This definition of IL is not exactly consensual since it is based on an arbitrary physical property (melting point). Some authors distinguish ILs and room-temperature ionic liquids (RTILs), the latter considered as having melting temperature below 25 °C [62]. Figure 2.9. shows the different categories of the aforementioned salts.

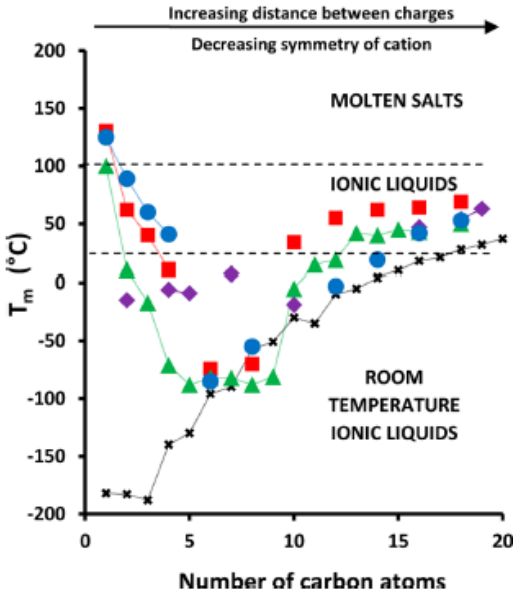

Figure 2.9. Melting point as a function of cation alkyl chain length in several 1-n-alkyl-3-methylimidazolium salt systems [62]. Notice the different categories delimited by the dashed lines.

All ILs are compounds made up of ionic species. They should remain in the liquid state at or below process temperature. The simplest IL contains at least one cation and one anion [29]. Figure 2.10. shows a small group of ions that make part of the 'ILs' world'.

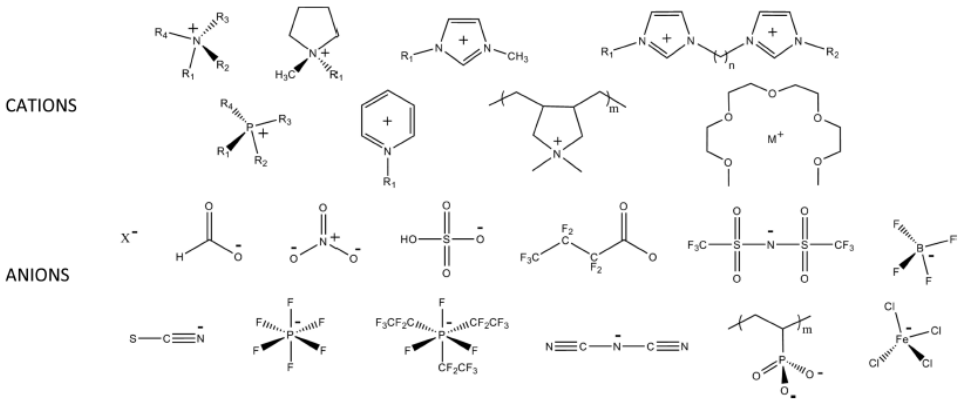

Figure 2.10. Some cations and anions present in ILs [62]. From left to right, the cations (top row) are: ammonium, pyrrolidinium, 1-methyl-3-alkylimidazolium, 1,3-bis[3-methylimidazolium-1-yl]alkane; (second row) phosphonium, pyridinium, poly(diallyldimethylammonium), metal (M+) tetraglyme. The anions contain (third row) halides, formate, nitrate, hydrogen sulfate, heptafluorobutyrate, bis(perfluoromethylsulfonyl)imide, tetrafluoroborate, (bottom row) thiocyanate, hexafluorophosphate, tris(pentafluoroethyl)trifluorophosphate, dicyanamide, poly(phosphonic acid), and tetrachloroferrate.

These compounds can also be categorized in a different manner [29]:

- Room-temperature ILs, which are organic salts that melt near room temperature. They possess bulky and low-symmetry cations with a delocalized charge, whilst the anions are more symmetrical and smaller than the cations;
- Task-specific ILs, that contain a functional group which is covalently combined into the cation, the anion or both ions of the IL;
- Poly(IL)s, which are solids at room temperature and present high CO_2 sorption capacity;
- ILs based on Jessop's 'switchable solvent' concept, where a non-IL becomes an IL in the presence of CO_2. That formed IL can turn back to a non-IL if the CO_2 is stripped out with N_2 [63].

In general, ILs are characterized as having suitable properties for several applications, such as non-flammability, negligible volatility, high thermal and electrochemical stability as well as high ionic conductivity [64]. Their high design flexibility allows to tune physical or chemical properties for a desirable application. Owing to their properties, they are used in the study of chemical reactions, catalysis, extractions, gas absorption; they also are promising materials as electrolytes for electrochemical devices, fuel cells or dye-sensitized solar cells [65].

ILs demonstrate good solvency for a wide range of substances, which can be ultimately seen as a drawback due to possible contamination. Low and uncontrolled purity percentages are also a concern in the manufacture of these compounds. In CO_2 capture, the IL viscosity can largely increase [62], and low absorption capacity at lower pressures is verified while using these materials from flue gas emitted by power plants [66]. Cost issues are also relevant: some ILs can still be costly due to their synthesis. Low gas diffusion coefficients are observed when using pure ILs [66].

2.3. Gas Adsorption

2.3.1. Fundamentals

Adsorption is a millennial phenomenon whose first applications, unknowingly making use of adsorbent materials, can be traced to civilizations like the ancient Egyptians, Greeks and Romans [67]. In more contemporary times (1773), C.W. Scheele made the first quantitative study regarding gas uptake by a charcoal [67, 68]. Large-scale adsorption processes first appeared in the 1920's in Germany and in the United States of America almost simultaneously; the German process was developed by Bayer AG with the purpose of removing alcohol and benzene from a gas stream while the USA-located process was implemented by the Union Carbide Corporation with the intent of recovering ethane and other higher hydrocarbons from natural gas [58].

The term adsorption refers to the enrichment of one or more components (adsorbates) of either a gas or liquid in an interfacial layer, e.g., at the surface of a solid (adsorbent) [58, 67]. Customarily, the adsorbent is a solid but can also be a liquid if the fluid phase's components only stick to its surface [68]. When the fluid molecule approaches the solid surface, a balance is created between intermolecular attractive and repulsive forces [67]. That force field creates a low potential energy region close to the adsorbent's surface and, with that, molecular density near the surface is normally greater than in the bulk fluid [56]. It ought to be noted that if there are already molecules adsorbed to the adsorbent's surface, interactions adsorbate-adsorbent and adsorbate-adsorbate are established [67]. In a multicomponent mixture, the composition of the bulk fluid will be different from the composition on the surface layer since the components will have different affinities with the adsorbent. The relation between the affinities of different species is named selectivity and it is a parameter of great importance in adsorption applications [56]. When the adsorbate leaves the adsorbent's surface, the opposite phenomenon of adsorption occurs and is named desorption. In reality, both phenomena occur simultaneously but at different rates. If one examines the number of molecules adsorbed and those desorbed at a given time interval, the dynamic equilibrium observed is called adsorption equilibrium [68]. Figure 2.11. illustrates adsorption and desorption processes and selectivity towards adsorbates.

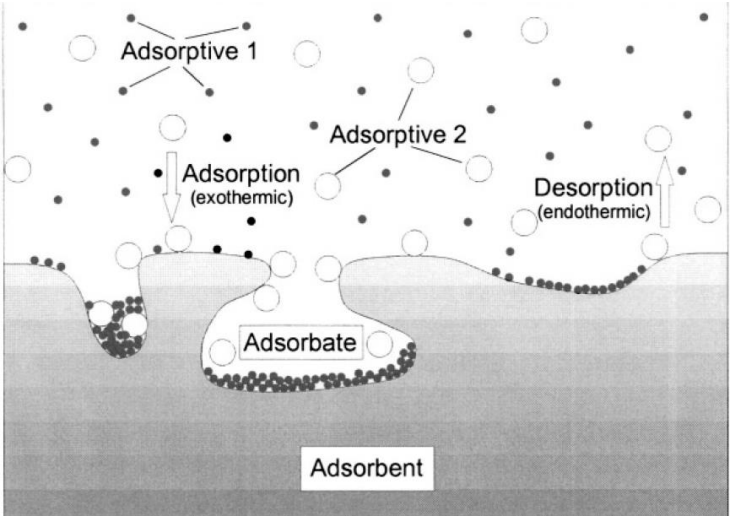

Figure 2.11. Adsorption and desorption phenomena [68]. Note that Adsorptive 1 has a higher affinity with the surface than Adsorptive 2. An adsorptive compound is an adsorbable substance in the fluid phase.

It seems apparent by now that the adsorption phenomenon is different from the absorption one. Consider a person and a cake, where the former is the support where sorption will transpire and the latter are the molecules in the fluid phase. In this representation, absorption is the equivalent of the person eating the cake, whilst adsorption corresponds to said person being splashed in the face with the cake. In more scientific terminology, adsorption is a surface phenomenon that can happen at a given temperature and pressure, whereas absorption is a bulk (or volume) phenomenon which may or may not happen at any temperature and pressure [68].

Depending on the nature of the forces that bind the adsorbate(s) to the adsorbent's surface, adsorption can be classified as [68]:

- Physical adsorption or physisorption, in which the adsorbate is weakly bound to the surface (van der Waals and/or dispersion forces because of the induced dipole-dipole interactions). Desorption is normally reversible and no chemical reactions ensues in this kind of adsorption;
- Physico-chemical adsorption, a mixed kind of adsorption characterized by weak bounds between adsorbent and adsorbates but, due to catalytic properties of the former, changes in the latter can follow (e.g., dissociation or moderately strong associations of adsorbed molecules);
- Chemical adsorption or chemisorption, where strong, chemical bounds between adsorbates and adsorbent are a feature, mainly because of electron transfer. The adsorbed molecules suffer chemical reaction and the desorption phenomenon is irreversible.

Table 2.2. summarizes the difference in the key aspects between physical and chemical adsorption.

Table 2.2. Differences regarding physical and chemical adsorption [55, 56, 68].

Parameter	Physical adsorption	Chemical adsorption
Selectivity of adsorbed fluid	Low	High
Kinetics	Rapid; Controlled by resistance to mass transfer	Slow
Quantity adsorbed	High (at low temperatures)	Low (at low temperatures)
Forces of adsorption	No electron transfer (but possible polarization of adsorbates)	Electron transfer that leads to a bond formation between adsorbates and adsorbent
Desorption	Reversible	Irreversible
Structure of adsorbate	Monolayer Multilayer	Monolayer
Heat of adsorption	Low, same order as heat of vaporization	Large, many times greater than the heat of vaporization
Temperature range	Only significant at relative low temperatures	Possible over a broad range of temperature

Regarding the adsorption capacity, factors related with the adsorbent (e.g., specific surface area) and with the adsorbate (e.g., the nature of the gas) must be considered. An increase in the specific surface area will lead to an increment in active adsorption centres and, consequently, a higher adsorption capacity. About the adsorbate, adsorption is related to its critical temperature (T_c). Compounds with higher T_c will be more adsorbed because attractions between adsorbent and

adsorbate can happen on a higher temperature range. This is why CO_2 (T_c = 31.1 °C) shows a higher adsorption capacity than CH_4 (T_c = -82.6 °C).

Nevertheless, the two variables that are of vital essence are temperature and pressure. Both influence the adsorption capacity and the amount adsorbed is generally plotted as a function of one the variables while the other is kept constant. When pressure is constant, an isobar of adsorption equilibrium is obtained. In contrast, when temperature is kept constant, the obtaining data correspond to an isotherm of adsorption equilibrium and the adsorption capacity differs with pressure. Figure 2.12. and Figure 2.13. show a typical adsorption isobar and isotherm, respectively.

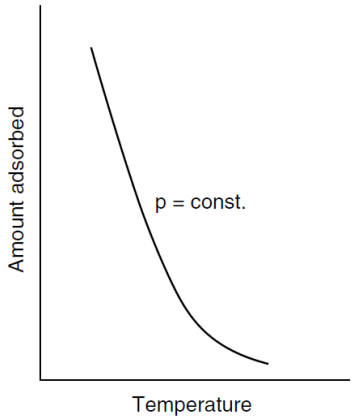

Figure 2.12. Generic isobar [69].

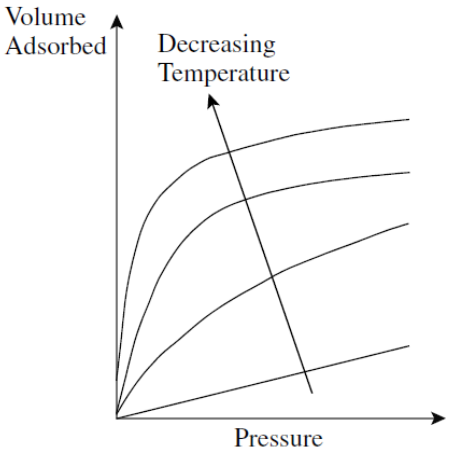

Figure 2.13. Generic isotherms [55].

As seen in Figure 2.13., pressure increments lead to an increase in volume (or amount) of fluid adsorbed while a temperature raise originates a decrease in volume (or amount) adsorbed. Adsorption, like absorption, is therefore an exothermic phenomenon.

Lastly, if the amount of adsorbed fluid is maintained constant, plotting pressure as a function of temperature, the obtained representation is named an isostere.

Normally, adsorption data are expressed through isotherms, existing different types (for physical adsorption) of these depending on the outline they make. These are presented in Figure 2.14.

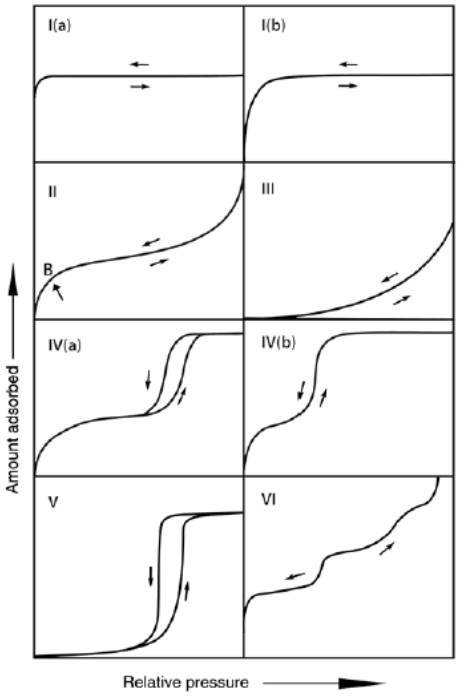

Figure 2.14. Different types of physical adsorption isotherms, according to IUPAC [70]. The arrow pointing towards increasing relative pressure shows the adsorption curve; the arrow pointing to the decrease of relative pressure shows the desorption curve.

Physical adsorption isotherms can then be defined as [70]:

- Type I, associated to microporous materials with somewhat small external surface. They are reversible and concave to relative pressure axis. They present a limiting adsorption capacity that is related to the micropore volume access. The steep uptake at very low pressures is due to strong interactions between the adsorbent and adsorbate in narrow micropores that fill quite easily. Type I(a) is verified in materials that have narrow micropores (< 1 nm) while Type I(b) is seen in materials that have broader micropores (< 2.5 nm);
- Type II, related to nonporous or macroporous adsorbents. They are reversible and the shape is related to monolayer to multilayer adsorption. Point B, identified in Figure 2.14., is where normally the monolayer is completely covered. After point B, a different kind of curvature is observed and it is related with the overlap of the monolayer, thus the starting point of multilayer adsorption;
- Type III, where the inexistence of point B hinders the identification of the multilayer formation. Weak adsorbent-adsorbate interactions are verified with the adsorbed molecules clustered in the most favourable sites of the nonporous or macroporous adsorbent;
- Type IV, observed in mesoporous materials. The adsorption is dictated by adsorbent-adsorbate interactions as well as interactions between molecules in the condensed state.

The initial behaviour of Type II isotherms is found, with the monolayer-multilayer forming in the mesopores walls. Then, pore condensation occurs: gas condenses to a liquid-like phase in a pore at a given pressure that is inferior to the saturation vapour pressure of the bulk liquid. This type of isotherm has a final saturation plateau that sometimes is merely an inflexion point. In Type IV(a), hysteresis follows capillary or pore condensation. This happens whenever the mesopore width surpasses a certain critical value that is intrinsic to the adsorbent and is temperature dependent. If mesopores have a smaller width, then reversible isotherms are obtained: Type IV(b);

- Type V, in where weak adsorbent-adsorbate interactions are perceived (like Type III isotherms) at low relative pressures. At high relative pressures, molecular clustering followed by pore filling happens. They may describe the adsorption capacity of some microporous or mesoporous materials;
- Type VI, that have a stepwise, reversible going that corresponds to a layer-by-layer adsorption in a uniform albeit nonporous materials. The step-height is equivalent to the capacity of each layer and sharpness of the step is adsorbent and temperature-dependent.

Visible on Figure 2.14. is the possible existence of hysteresis on an adsorption equilibrium isotherm. Hysteresis is a tendency of a system to preserve its properties even in the absence of the stimulus that created them. The value of said property will lag behind changes in the effect causing it. Types IV and V physical adsorption isotherms present hysteresis (that corresponds to the desorption branch on mesoporous materials). This phenomenon materializes in the multilayer range, appearing when the amount adsorbed is not the same on the adsorption and desorption branches at a certain pressure [67], and are associated to capillary condensation [70].

Like the physical adsorption isotherms, hysteresis loops present several different shapes, as presented in Figure 2.15. These loops are defined by IUPAC and all represent a specific kind of pore structure as well as a subjacent adsorption mechanism [70].

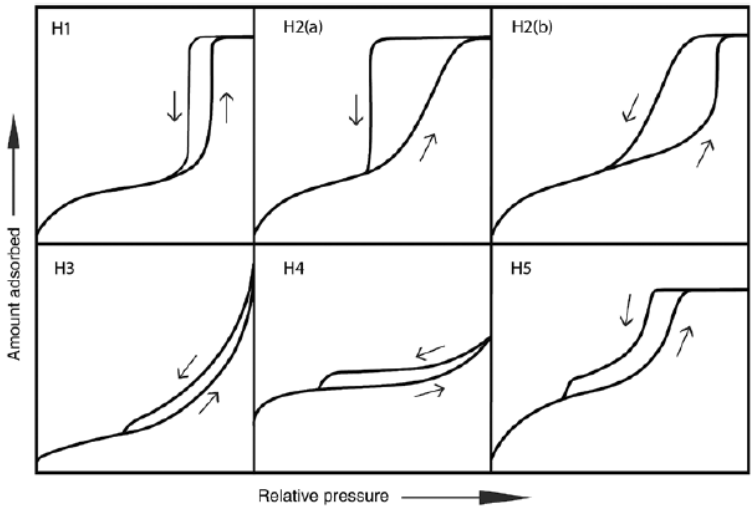

Figure 2.15. Different types of hysteresis loops [70]. Upward arrows show adsorption branch; downward arrows represent the desorption path.

Adsorption-related processes are used industrially for separation/purification/drying of fluid streams, removal of unwanted compounds, capture/storage of substances, just to name a few [68]. Table 2.3. specifically presents some adsorption-based industrial separations.

Table 2.3. A list of some adsorption-based separations [58].

Adsorbate	Other compounds in the feed	Adsorbent	Main use
Paraffins	O_2	Zeolite	Gas separation
CO_2	H_2	Zeolite or activated carbon	Gas separation
p-xylene	o-xylene, m-xylene	Zeolite	Liquid separation
Fructose	Glucose	Zeolite	Liquid separation
CO_2	C_2H_4	Zeolite	Gas purification
H_2O	Air	Silica, alumina, zeolite	Gas purification
Chlorinated organics	H_2O	Activated carbon	Liquid purification
Sulphur compounds	Organic compounds	Zeolite	Liquid purification

For biogas upgrading, which is essentially a CO_2/CH_4 separation, either zeolites or activated carbons are used in a Pressure Swing Adsorption (PSA) process. Adsorption/desorption of CO_2 occurs at different pressure steps and "swing" means that vessels work cyclically in countercurrent in terms of feed/pressurizing and depressurizing. The later stage works as the regenerating step of the adsorbent being employed. Before the desired gas separation takes place, all H_2S present in biogas streams must be removed since its adsorption is irreversible, which leads to adsorbent's poisoning. H_2O is also removed [71]. Figure 2.16. shows a common PSA schematic for biogas upgrading.

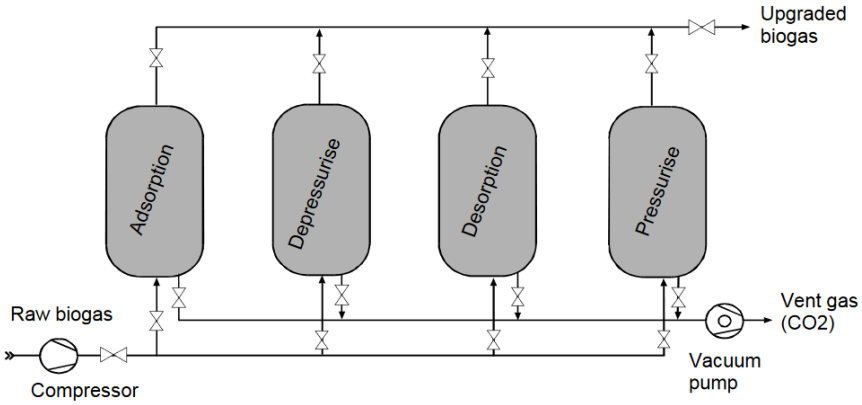

Figure 2.16. Upgrading biogas with a PSA process [72].

A PSA plant normally consists of at least two adsorbent-containing vessels. Each vessel undergoes the complete set of steps and vessel linkage is made so as to decrease the energy demand when gas compression is required between steps. Every vessel works in four different steps: adsorption, depressurizing, regeneration and pressurization (see Figure 2.16.). In the adsorption phase, the raw biogas is compressed and fed to the bottom of the adsorption column,

passing through it; CO_2, N_2 and O_2 are adsorbed by the adsorbent, leaving the top of the vessel enriched with CH_4 up to 97%. Before the adsorbent is completely saturated, biogas is redirected to another pressurized column and regeneration of the saturated vessel commences. The pressure inside the referred saturated column is decreased: the vessel is firstly depressurized by balancing it with another vessel which is already regenerated; pressure is then lowered to atmospheric pressure and, at this point, the gas leaving the column contains high concentrations of CH_4 that is recycled to the inlet of crude biogas; finally, vacuum is created inside the vessel. At this point, the gaseous mixture leaving the vessel mainly consists of CO_2, but also some CH_4. This mixture can be used for several purposes. Therefore, CH_4 losses exist during the upgrading process and should be minimized. Before the now-regenerated column is again used for adsorption, pressure is increased bringing the cycle full circle. The vessel is first pressurized by balancing it with a vessel that has been in the adsorption phase and, after that, the final pressure accumulation is attained with feed gas [72]. The upgraded gas, now designated biomethane, can be used for different applications. If it is meant to be used in the natural gas distribution grids, it must meet the standard of 97% of CH_4.

There are three different mechanisms that are considered the foundations of adsorption separation: steric, equilibrium and kinetic. The steric mechanism is related to the pore size of the adsorbent: small molecules are allowed in while larger ones are excluded. The equilibrium mechanism is based on the fluid's affinity with the adsorbent: stronger adsorbing species are favourably adsorbed. The kinetic mechanism is associated with the rate of diffusion of a fluid into the pore: faster diffusing species are preferentially adsorbed [73].

2.3.2. Adsorbents

Briefly, adsorption is the result of the interactions taken between adsorbates and adsorbent. The latter's presence is *ipso facto* fundamental to trigger the adsorption phenomenon and are typically chosen from a range of porous materials. These materials are preferred over non-porous ones mainly due to higher specific surface areas and higher micropore volume. These parameters are both related to high adsorptive capacities. The chosen material ought to perform well on a kinetics and equilibria basis: fast kinetics are favoured as well as a good capacity. If these criteria are met, one is dealing with a material in where adsorbate molecules don't take too much time reaching its interior and no large amounts of solid are required to obtain a desired throughput. These requirements are normally met by materials that have high specific surface areas and micropore volume (pores fill at relatively low pressures) and that have a somewhat extended pore network (mesopores) for the transport of adsorbate to its interior [73].

A rather arbitrary classification of pore size was defined by IUPAC [73] as:

- Micropores, with a pore diameter of less than 2 nm;
- Mesopores, with a pore diameter between 2 and 50 nm; and
- Macropores, with a pore diameter above 50 nm.

Normally, industrial adsorbents possess specific surface areas well over 100 m^2/g and are highly porous [67]. A variety of adsorbents are employed in the chemical industry and are commonly regenerated (i.e., desorption step is taken) instead of being used once and then discarded. The regeneration allows the recovery of the adsorbates in processes where they may be valuable and, logically, that permits the reuse of the adsorbent for further cycles [58].

- **Activated alumina**

It is a porous form of aluminium oxide (Al_2O_3) that suffers dehydration and recrystallization at high temperatures (activation process) [74]. This adsorbent is generally used in drying processes, e.g. the removal of water from a gas stream. High functional groups density provides active sites for polar molecules adsorption [73].

- **Silica gel**

A partially dehydrated form of polymeric colloidal solution of silicic acid, it has a general chemical formula of $SiO_2 \cdot nH_2O$. The term gel indicates the nature of the material on the preparation step and not the condition of the final product [73, 74]. Possessing a hydrophilic surface, it is commonly used for water removal from air and drying of gases, as well as the adsorption of hydrogen sulphide, alcohols and oil vapours [73].

- **Activated carbon**

These materials are normally obtained from the thermal decomposition of carbonaceous material and consequent activation process (700-1100 °C) with steam or CO_2 that will lead to pore formation. These treatments will determine pore size as well as total pore volume. These materials possess an almost nonpolar surface. This explains why these adsorbents normally utilized in applications that involve organic compounds rather than water [74].They are quite versatile because they possess high specific surface areas and micropore volume, usually revealing a bimodal pore size distribution (micro and macropores), and sometimes even a trimodal distribution, that allows access to adsorbate molecules into the adsorbent's interior. The activation process can be optimized in such way that it mainly leads to micropore formation. They have a complex structure, part amorphous, part graphite-like microcrystalline. It is the latter that has a deciding role in the capacity of adsorption, since it presents slit-shaped channels where adsorbate molecules can enter. Depending on the application, commercial activated carbons present a varied range of properties [73].

- **Zeolites**

Zeolites are porous crystalline aluminosilicates with generic chemical composition of $M_{x/n}[(AlO_2)_x(SiO_2)_y] \cdot zH_2O$, where *x* and *y* are integers and *y*/*x* is a ratio equal to or greater than one, *n* is the valence number of the alkali or earth alkali element and *z* is the number of water molecules per unit cell [75]. Atoms are arranged in such fashion that they form crystal lattice containing pores of molecular dimensions in where adsorbates can accommodate. Micropore structure is defined by the crystal lattice, that are uniform; hence why no pore size distribution is verified. This is the main difference between zeolites and other kinds of adsorbents [74]. Adsorption happens inside the crystals and the access is restricted due to pore size. This stands out as another dissimilarity between zeolites and other adsorbents: the separation of mixtures is due to the difference of molecular size of the compounds that are to be separated [58].

- **Metal-Organic Frameworks (MOFs)**

Since the 1990s that much work has been done on the field of organic-inorganic hybrid materials, and MOFs (metal-organic frameworks) are a subset of these materials [76]. They are considered novel porous crystalline materials and are composed of metal or small clusters of metal sites and are connected to organic functional groups that serve as linkers [77]. The potential of these materials is related to their properties: mild synthesis conditions, effective design methods (easily tuneable), varied metal compositions, a multitude of organic functional groups that can be directly incorporated in the framework, thermal stability, large pores and cavities and extremely high specific surface areas [76]. While most MOFs usually have a static framework, some of them have the unique ability to show phenomena of structural transition such as 'breathing' or 'gate-opening effects' [78]. The pore diameter can enlarge or shrink due to applied or removed external stimuli, like pressure, temperature or addition of gas/solvent molecules [79]. MOFs are formed with the use of reticular synthesis, a process that permits the assembly of rigid building blocks into ordered structures (networks) that are held together by strong bonding. This process allows the building blocks to retain their structural integrity [31].

Most of the metal ions or metal clusters are usually transition metals, presenting different geometries because of their different coordination numbers. The organic ligands can be cyanides, halides and neutral/anionic organic molecules [79]. Linkers and metal centres can form 1, 2 or more dimension structures, as presented in Figure 2.17., that can have flexibility upon the interaction with guest molecules ('breathing' phenomenon).

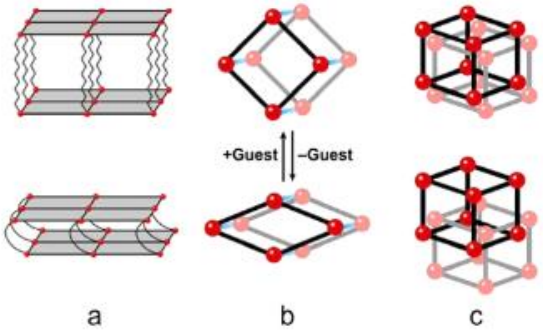

Figure 2.17. MOFs structure when interacting with guest molecules. (a) 2D; (b) 1D; (c) 3D. Red spheres denote metals; dark lines represent the organic linkers [80].

Due to their properties, MOFs have potential of application in the fields of gas purification/separation, catalysis, molecular sensing, hydrogen storage, among other green and renewable energy-targeted applications [77, 79].

- **The particular MOF subclass of ZIFs**

When compared to zeolites, MOFs present a somewhat lower thermal stability [79]. This subclass of MOFs has, however, remarkably high thermal stability. Named zeolitic imidazolate frameworks (ZIFs), they are a novel class of porous crystals that form 3-dimensions structures where the tetrahedral metal ions or metal clusters are bridged by imidazolate. The angle made by metal-imidazolate-metal is of 145 °, the same created by Si-O-Si in zeolites [81]. Figure 2.18. shows the similarities.

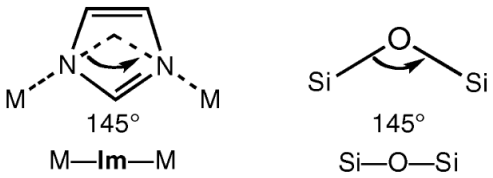

Figure 2.18. Comparison of angles in ZIFs and zeolites [81]. M stands for metal; Im stands for imidazolate *[81]*.

The distance between the metal centres in ZIFs is about twice the distance of the Si-Si distance in zeolites with similar topology. Ergo, the pore volume of ZIFs is larger than that of a corresponding zeolite, which entails a larger adsorption capacity. Other advantages over zeolites are minimal water adsorption and easy regeneration The primary disadvantage ZIFs present, when compared with zeolites, is that pore apertures cannot be as easily modified [82]. ZIFs present characteristics of MOFs as well as zeolites, so it comes with no surprise that they exhibit a combination of properties of both materials such as high specific surface areas, unimodal micropores, high crystallinities, elevated chemical and thermal stabilities, among others. This blend of properties makes ZIFs a potential candidate for gas separation [83].

2.4. IL@MOF Composites

Until now, it seems clear that ILs and MOFs seem to be good CO_2 capture/separation materials. But little is known about the incorporation of ILs on the MOF pores, which opens a new field of interesting and possibly fruitful research. The IL-impregnation of MOFs can be seen as an attempt to combine the 'best of the two worlds' while possibly minimizing the shortcomings of these two distinct materials. For instances, ILs present some drawbacks like high viscosity and high costs that can be minimized through impregnation on a porous solid while favouring mass transfer and separation efficiency [29]. Figure 2.19. shows the evolution of published articles with respect to IL@MOF materials. This analysis discards any papers related to IL@MOF-incorporated membranes. As evidenced in Figure 2.19., the published articles can be categorized as computational study, experimental study (some present both kind of studies) and, most recently, review articles. Computational studies try to understand different IL-MOF interactions while they may also point to the best IL for a given application. Experimental studies normally focus on the manufacture of IL@MOF for a specific application; ergo, it is customary a textural characterization of these materials through several standard techniques. Review articles highlight the state of art towards these composites.

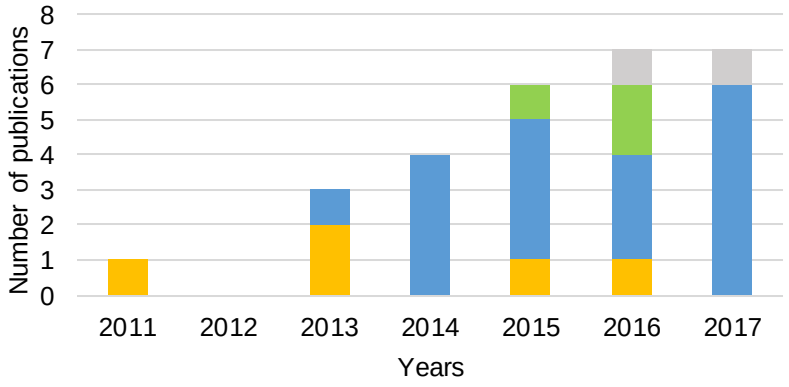

Figure 2.19. Publications regarding IL@MOF materials as of July 2017, discarding membrane-related articles. **Yellow** bars denote only computational studies; **blue** bars indicate only experimental studies; **green** bars stand for computational and experimental studies in a paper and **grey** bars represent review articles.

2.4.1. Computational Studies

These studies normally try to enlighten the interactions between the IL and the MOF structure. Chen et al. (2011) were the first in trying to figure out these interactions. Through their simulations, they concluded that bulky cations, e.g., $[BMIM]^+$, could be found on the open pores of IRMOF-1 while the anion would be located near the metal cluster site, strongly interacting with the framework. The anion proved to be the most favourable site for CO_2 adsorption. Finally, they

uncovered that a higher ratio of IL in the composite material increased the selectivity of CO_2 present in a CO_2/N_2 mixture [34].

Vincent-Luna et al. (2013) reported that the incorporation of ILs on Cu-BTC increased the CO_2 capacity at low pressures, when compared to the pristine MOF, whereas the methane and nitrogen adsorption remained unchanged [84].

In Cu-BTC MOF, Gutiérrez-Sevillano et al. (2013) reported that the addition of ILs would block some of its structure's cages. That blocking would reduce the adsorption of polar molecules near the open metal centres. That is to say, ILs could reduce the attack of water molecules to the metallic centres, granting a superior stability to the framework [85].

IRMOFs may not be a great support system for the incorporation of ILs, according to Abroshan and Kim (2015). Their simulations show that the elongated anions can interact with multiple zinc atoms, destabilizing the MOF structure in an easier fashion than spherical anions [86].

Dispersion of the IL seems a rather important factor when trying to enhance gas separation performance, according to Xue et al. (2016). The research group concluded that MOFs will provide good IL dispersion due to the presence of metals in the framework. MOFs with 3D pore structure could enhance even more the separation performance of these materials [87].

2.4.2. Experimental Studies

Several articles have synthesized different IL@MOF materials for different applications such as catalysis, removal of pollutants, gas adsorption and ionic conduction. Logically, some characterization techniques differ according to the target application. Hereafter, only gas adsorption-related original research will be disclosed.

IL@MOF composites were carbonized by Aijaz et al. (2014) and their CO_2 and H_2 adsorption capacity were tested at a pressure range of 0-1 bar. Two composites were prepared: [EMIM][$N(CN)_2$]@MIL-100 (Al) and [EMIM][$B(CN)_4$]@MIL-100 (Al). This is the first work that use these composites materials as precursors for large specific surface area nanoporous carbons. The carbons obtained from these composites presented higher gas uptake than the carbonized MIL-100 (Al) [88].

In the study of da Silva et al. (2015), Cu-BTC was impregnated with different concentrations of [BMIM][PF_6] and [BMIM][NTf_2]. They found out that high IL concentrations (10% wt) had a detrimental effect on the textural properties of the MOF whilst low concentrations (5% wt) did not improve CO_2 uptake. The group concluded that Cu-BTC is not a proper support for IL impregnation due to its small pore windows [89].

Kinik et al. (2016) incorporated [BMIM][PF_6] into ZIF-8 for the study of CO_2 separation performance. The composite material showed less gas uptake than the pristine ZIF-8, which can be explained by the reduction of available adsorption sites as well as pore volume that results from the partial pore occupation by the IL. The group's standout result was the increase, up to 0.4 bar, of CO_2 uptake per gram of ZIF-8 thanks to the IL impregnation. This can be justified by the creation of new and stronger adsorption sites for CO_2 at low pressures. IL-MOF interactions thereby affect the gas affinity of these materials at low pressures whereas the available pore volume is the crucial factor for adsorption at high pressures. The referred IL-MOF interactions lead to at least a doubling of CO_2/CH_4 and CO_2/N_2 selectivities when compared to pure ZIF-8. This article proves that IL@MOF composites can be promising gas separation materials [90]. Nonetheless, the group only used one IL for impregnation. No comparison with other ILs were made and, by extent, no conclusions if the impregnated IL is good for adsorption capacity/selectivity is made in this paper.

The most recent paper regarding CO_2 separation with IL@MOF materials presents a study in which Sezginel et al. (2016) impregnated Cu-BTC with [BMIM][BF_4] in different concentrations (5, 20 and 30 wt%). Adsorption equilibrium isotherms were then measured for CH_4, H_2, N_2 and CO_2 and later compared with the pristine Cu-BTC. Gas uptake by the composites materials decreased comparatively to the pure Cu-BTC, with increasing concentrations of IL impregnation leading to more notable decreases in adsorption gas capacity. An explanation for this evidence is the reduction of the specific surface area that comes from IL incorporation, which leads to a reduction of adsorption sites. Decreases were more evident for gas molecules that have stronger interactions with the MOF (CO_2, CH_4, N_2 and then H_2). At low pressures, the decrease in gas adsorption does not possess the same profile for all studied gases; that is, the degree of gas uptake is solely dependent on the gas identity. With that said, whilst a decrease in adsorption sites took place, new adsorption sites with different affinities for each gas were developed upon IL incorporation on the MOF. A comparison at 1 bar for all IL loadings is presented, revealing that increasing concentrations impair gas adsorption; in particular, CO_2, at 30% IL loading, has an almost 50% drop in capacity, while H_2, N_2 and CH_4 have 40%, 30% and 20% drops, respectively. Selectivities were calculated between 0-1 bar of pressure for all possible combinations of gases pairing. An increase in selectivity is a recurring pattern in that range, except for CO_2/CH_4 selectivity, especially when considering the highest IL loading [91]. The normalized selectivities highlight that the most interesting pressure range in terms of selectivity increase is 0-1 bar and, in addition, that higher IL loadings also lead to higher selectivities values.

It is considered relevant to point out that no mention to IL solubility is made in any of these papers.

2.5. Methodologies for Adsorption Equilibrium Measurements

It appears evident that, in order to know the adsorption capacity of an adsorbent, one needs to measure the adsorption equilibrium. Though there are several measuring techniques, ordinarily it comes down to two methods: the volumetric/manometric one or the gravimetric one.

- **Volumetric/Manometric method**

It is the oldest method to determine the adsorption capacity of adsorbents [68]. Gas pressure is measured in a calibrated and constant volume, at a certain temperature [67]. A volumetric apparatus, in a general way, consists of a gas storage vessel and an adsorption chamber/cell. These two are connected by a tube holding up a valve. Also important is the existence of a fluid supply, exhaustion and temperature and pressure indicators [68]. So, two distinct steps take place: fluid loading and fluid expansion [92]. The inlet of fluid is allowed in the storage vessel; this should increase the pressure inside the system. Then the valve that separates the storage vessel from the adsorption chamber/cell is opened, expanding the fluid that will then be adsorbed by a previously degassed adsorbent. A drop in the pressure is expected when fluid expansion is performed: not only does gas now occupy a larger volume, but the adsorption phenomenon is triggered. That will lead to a decrease in pressure until it finally reaches a plateau when adsorption equilibrium is achieved. A mass balance indicates how much fluid was adsorbed; said balance has the change in pressure from the storage vessel to the adsorption chamber/cell into account. Desorption of a fluid can be attained by simple depressurization of the system [68, 92]. The volumetric/manometric method is simple and can be merely seen as measurements of pressure and temperature in gas phase. However, several grams of sorbent material are required, thermodynamic equilibrium can't be confirmed directly unless mass measurements are coupled with the volumetric apparatus, wall sorption may take place and uncertainties in the adsorbed mass accumulate in a step-up pressure experiment [68]. All in all, volumetric measurements lack on information regarding the kinetics of the process and data retrieved may not be as precise as in the gravimetric method. The experimental data points are limited due to the errors accumulation and the pressure and temperatures available are dependent of the accuracy of the probes.

- **Gravimetric method**

It is a relatively new method for testing the adsorption capacity of an adsorbent. By means of highly sensitive balances, the adsorbate's mass can be directly accounted. Historically, gravimetric adsorption equilibrium measurements were only made possible circa 1965, when the first microbalances were commercially manufactured. Inside the microbalance, the vessels containing the adsorbent will always be surrounded by the fluid and, so, only the difference between the sample's weight and the buoyancy force exerted can be registered. One can consider it as 'apparent weight' readings [68]. The method proves to be highly accurate when

performing adsorption equilibrium measurements; kinetics of adsorption can be studied, adsorption equilibrium can be observed and the apparatus can endure extreme pressures. On the other hand, these systems are quite complex, sensitive to electromagnetic disturbances, and microbalances are very expensive [68].

3. Experimental Work

This chapter is divided into three parts:

- Materials section, where a brief explanation for all compounds used on the formulation of IL@ZIF-8 materials is given;
- IL@ZIF-8 materials sample preparation, with a description of the experimental procedure followed;
- IL@ZIF-8 materials characterization, which takes into account the adsorption equilibrium measurement techniques employed for the determination of adsorption isotherms as well as all textural characterization techniques used.

3.1. Materials

For this thesis, several IL@ZIF-8 composites were prepared always using ZIF-8 as the pristine MOF. ZIF-8 (Basolite® Z1200, 2-methylimidazole zinc salt: $C_8H_{10}N_4Zn$) was purchased from Sigma-Aldrich as produced by BASF SE. ZIF-8 was chosen due to its pore size (11.6 Å, with a pore aperture of 3.4 Å); crystalline and highly porous framework structure; large and accessible pore volume; chemically stable in the presence of water and some aromatic compounds, like benzene, that are common natural gas impurities; hydrophobic nature; high thermal and chemical stability; high specific surface area and, last but not least, its commercial availability [93].

Nine ILs were chosen and the motive was always related to the cation/anion nature and structure. All but one IL have imidazolium-based cations and the reasoning behind the choice was that imidazolium-based ILs can dissolve significant CO_2 amounts [94]. The exception was one IL with a phosphonium-based, large cation to test the influence of its structure. Going back to the employed imidazolium-based cations, they possess different alkyl chains and the effect of their size was deemed important for this study. Small, intermediate and large alkyl chains were tested (C2, C6 and C10, respectively).

The choice of anions was more diverse. While the bis(trifluoromethylsulfonyl)imide anion was the predominant one since it favours the solubility of CO_2 [33], cyano-based ILs were also chosen since previous studies indicate they can outperform bis(trifluoromethylsulfonyl)imide-based ILs should the same imidazolium cation be considered [95]; hence this is why $[B(CN)_4]^-$ and $[N(CN)_2]^-$ anions were tested. Anion size was also tested with an IL possessing chloride as its anion. Finally, an IL with acetate as its anion was tested because very strong interactions with CO_2 are expected.

Table 3.1. shows the identification of all ILs used, their manufacturers and purpose.

Table 3.1. ILs used in the formation of IL@ZIF-8 composites. Nomenclature and chemical formulas were taken from Ionic Liquids Database – ILThermo.

Ionic liquid	Chemical formula	Designation	Designation adopted herein	Purpose of study	Source (Purity %)
1-ethyl-3-methylimidazolium bis(trifluoromethylsulfonyl)imide	$C_8H_{11}F_6N_3O_4S_2$	$[C_2MIM][NTf_2]$	C2	Alkyl chain size effect	IoLiTec (99%)
1-decyl-3-methylimidazolium bis(trifluoromethylsulfonyl)imide	$C_{16}H_{27}F_6N_3O_4S_2$	$[C_{10}MIM][NTf_2]$	C10	Alkyl chain size effect	IoLiTec (98%)
1-benzyl-3-methylimidazolium bis(trifluoromethylsulfonyl)imide	$C_{13}H_{13}F_6N_3O_4S_2$	$[BzMIM][NTf_2]$	Bz	Alkyl chain size effect	IoLiTec (98%)
1-(2-hydroxyethyl)-3-methylimidazolium bis(trifluoromethylsulfonyl)imide	$C_8H_{11}F_6N_3O_5S_2$	$[C_2OHMIM][NTf_2]$	C2OH	Extra OH group effect (by comparison to $[C_2MIM][NTf_2]$)	Alternative Fluids for Green Chemistry Laboratory (99%)
1-hexyl-3-methylimidazolium tetracyanoborate[1]	$C_{14}H_{19}BN_6$	$[C_6MIM][B(CN)_4]$	C6B(CN)4	Anion nature effect	Merck (98%)
1-hexyl-3-methylimidazolium dicyanamide	$C_{12}H_{19}N_5$	$[C_6MIM][N(CN)_2]$	C6N(CN)2	Anion nature effect	IoLiTec (98%)
1-hexyl-3-methylimidazolium chloride	$C_{10}H_{19}ClN_2$	$[C_6MIM][Cl]$	C6Cl	Anion size effect	IoLiTec (98%)
1-ethyl-3-methylimidazolium acetate	$C_8H_{14}N_2O_2$	$[C_2MIM][Ac]$	C2Ac	Anion nature effect	IoLiTec (98%)
Trihexyl(tetradecyl)phosphonium bis(trifluoromethylsulfonyl)imide	$C_{34}H_{68}F_6NO_4PS_2$	$[P_{66614}][NTf_2]$	P66614	Cation size and nature effect	Alternative Fluids for Green Chemistry Laboratory (98%)

Appendix A contains the solubilities of CH_4 and CO_2 in the ILs mentioned on Table 3.1. as reported in the open literature.

[1] Kindly granted by Professor Manuel Nunes da Ponte, Full Professor, LAQV-REQUIMTE, FCT/UNL, Lisbon, Portugal.

Table 3.2. shows the ZIF-8 and IL structures according to the designation adopted for this thesis.

Table 3.2. ILs and ZIF-8 structures. IL structures were taken from Ionic Liquids Database – ILThermo. The ZIF-8 structure was taken from reference [96]. The yellow sphere represents the free volume within the framework.

Designation adopted for this thesis	Structure	Designation adopted herein	Structure
C2	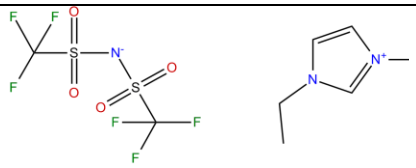	C6N(CN)2	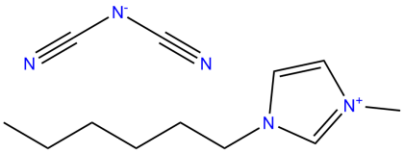
C10	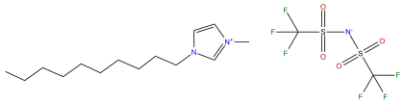	C6Cl	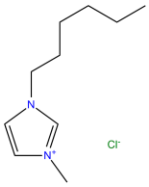
Bz	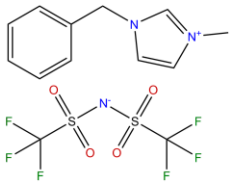	C2Ac	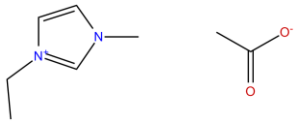
C2OH	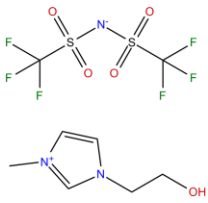	P66614	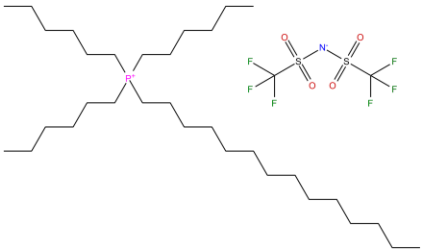
C6B(CN)4	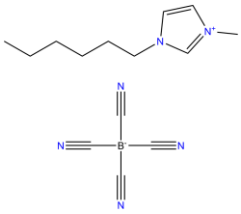	ZIF-8	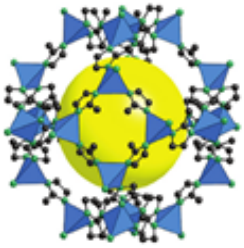

The chosen method of IL impregnation requires the use of a solvent. Acetone (99.8%, Carlo Erba) was used mainly because it is the most common solvent described on the background articles about IL@MOF materials.

The gases used for the adsorption measurements were CH_4 (99.95% purity, Praxair) and CO_2 (99.998% purity, Praxair). He was also used for the calibration of the volumetric unit, gas leaks detection (≥99.999% purity, Air Liquide) and He picnometry (>99% purity, Praxair).

3.2. IL@ZIF-8 Composites Preparation

Before describing the process of sample preparation, it ought to be explained that IL impregnation can be achieved by two different methods:

1) ionothermal synthesis, where the MOF is synthesized and ILs are used as solvents, and
2) post-synthesis methods (also called postimpregnation), where the MOF is already synthesized when the IL impregnation is carried out [65]. Since there was already commercial ZIF-8 in the laboratory, a post-synthesis strategy was followed. Figure 3.1. shows the three types of post-synthesis methods for IL@MOF composites preparation [65].

Solution of ILs	**Postsynthetic modification**	**Capillary action**
• A solvent is used in order to dissolve the IL in order to introduce it, through stirring, into the MOF structure. • Most common strategy for IL impregnation in MOFs.	• Also known as the Ship-in-a-bottle technique, the IL is sinthesized inside the MOF structure. • Good strategy for incorporating ILs larger than the pore diameter of the MOF, but may be difficult to account for the IL amount impregnated.	• Incorporation of IL happens by diffusion. The mixture obtained is heated in order to favour IL diffusion. • Can be used for several kinds of ILs and MOFs.

Figure 3.1. Post-synthesis methods for IL@MOF preparation.

The solution of IL was the adopted strategy due to its simplicity and for being the most frequent approach of impregnation. Concerns about how much and if the IL stays well impregnated were also considered factors.

In order to obtain reasonable comparisons within the prepared composites and between them and the pristine MOF, the number of moles of IL is the same in all samples. Therefore, 15 wt% loading of the C2 IL for 1 g of ZIF-8 was chosen as reference. Knowing its molar mass, it is possible to determine the IL moles necessary to accomplish the expected IL loading into the MOF. Only simple calculations are required, as demonstrated below:

$$m_{IL} = 0{,}15 \times (m_{ZIF\text{-}8} + m_{IL}) \Leftrightarrow 0{,}85\ m_{IL} = 0{,}15 \times 1{,}00\ g \Leftrightarrow m_{IL} = 0{,}176\ g$$

with m_{IL} as IL weight and $m_{ZIF\text{-}8}$ as ZIF-8 weight. Using C2 molar mass:

$$n_{IL} = 0{,}176\ g\ /\ (391{,}31\ g\ mol^{-1}) \Leftrightarrow n_{IL} = 4{,}5 \times 10^{-4}\ mol$$

with n_{IL} as IL moles.

These calculated moles were maintained constant for all ILs used and, knowing their molar mass, the multiplication of these two numbers gives the mass of IL one needs in order to keep the amount of substance (and not mass!) constant in all samples. Table 3.3. provides the added IL masses.

Table 3.3. Desired IL loadings in mass and weight percentage.

IL designation	Moles ($\times 10^{-4}$ mol)	Molar mass (g/mol)	IL mass (g)	Expected loading (wt %)
C2	4.5	391.31	0.1761	15.0
C10	4.5	503.52	0.2266	18.5
Bz	4.5	453.38	0.2040	16.9
C2OH	4.5	407.31	0.1833	15.5
C6B(CN)4	4.5	282.15	0.1270	11.3
C6N(CN)2	4.5	233.31	0.1050	9.5
C6Cl	4.5	202.72	0.0912	8.4
C2Ac	4.5	170.21	0.0766	7.1
P66614	4.5	764.00	0.3438	25.6

Later, different loading percentages were tested for select ILs; the added IL mass and respective loading percentage are later revealed in its proper section.

The protocol adopted is partially based on reference [90]. The IL mass is weighed on a Sartorius BL 120S model analytical balance (maximum weight of 120 g) onto a vial with a magnetic stirrer. Approximately 10 mL of acetone is added. The sample is stirred on a VWR VMS-C7 model magnetic hotplate stirrer, at room temperature and for a minimum of 1 minutes to confirm dissolution of the IL in acetone. The vial is closed with a lid. On another vial, 1 g of previously degassed ZIF-8 (by heating it up to 100 °C at least 3 hours) is weighed and the content of the IL vial is added to the ZIF-8 vial. With a lid on, the vial is stirred on a magnetic hotplate stirrer at room temperature overnight. On the next day, the lid is removed and stirring continues for 4-5 hours. After that, the sample is heated at a higher temperature than the solvent's boiling point. For example, a sample containing acetone is heated at 65 °C (acetone's boiling point is 56 °C). The sample is heated until it looks dry. Afterwards, the sample is passed to a smaller vial where a 'wet mass' is measured. There will be some sample loss during this process because the vial's walls shall also contain sample traces, as seen in Figure 3.2.

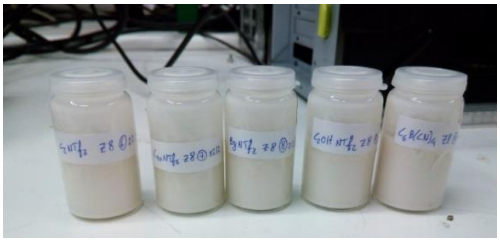

Figure 3.2. Illustration of some IL@ZIF-8 prepared samples. Notice how the vials' walls also contain sample traces.

Finally, the sample is degassed at 100 °C on a Nabertherm LE14/11/B150 model muffle furnace, in order to remove any moisture or impurities, as well as leftover solvent, for 3-4 hours. This temperature was set specifically for this MOF (by thermogravimetric analysis, TGA) and ensures that the solid is clean safely without degradation, as the ILs used are stable at this degassing temperature. The sample is then weighed in order to obtain its 'dry mass' and compare with the 'wet mass' previously obtained. Appendix B contains a step-by-step protocol developed for this thesis; Appendix C presents all mass measurements necessary during the protocol's following and Appendix D covers the differences between expected (theoretical) and actual IL loadings.

3.3. IL@ZIF-8 Composites Characterization

3.3.1. He Pycnometry

Pycnometry is a technique that is based on the intrusion of fluids (like He or Hg), used to obtain the volume of the solid matrix of the adsorbent through the measurement of the fluid's pressure [97]. For the prepared IL@ZIF-8 materials, He was used as a probe molecule under the assumption and approximation that it is not adsorbed by the solid material. The density of the solid matrix is obtained from its volume and mass. He pycnometry was performed on the gravimetric unit available in the research group, the same unit used to measure adsorption equilibria; the details of the apparatus will be later given in a more proper section. Notwithstanding, it is important to state that a gravimetric high-precision balance ISOSORP 2000 (Rubotherm GmbH) was used. Automated online data acquisition of pressure is made by the means of an in-house developed software (*BioCTR*).

Buoyancy forces must be taken into account in order to correct the influence of the gas density on the measured 'apparent' mass of sample. Displacements of gas by the sample holder, the adsorbent and the adsorbed phase must then be considered. The correction for the sample holder is obtained by a blank experiment where its mass and volume are determined. The buoyancy due to solid matrix of the adsorbent, that with increasing pressurization of the apparatus shows apparent mass decrease, is estimated as the product of the gas density and the skeletal volume of the adsorbent. The buoyancy effect exerted on the adsorbed phase is corrected in order to

obtain an absolute adsorption isotherm [98]. Equation 3.1. shows how the ('apparent') mass, measured by the balance, is the result of a net force exerted on the sample.

$$m = m_{\mathrm{h}}\left(1 - \frac{\rho_{\mathrm{g}}}{\rho_{\mathrm{h}}}\right) + m_{\mathrm{s}}\left(1 - \frac{\rho_{\mathrm{g}}}{\rho_{\mathrm{s}}} + q_{\mathrm{exc}}\right) \qquad (\mathrm{Eq.\,3.1.})$$

with m as weighed mass, m_h as mass of sample holder, ρ_g as density of bulk gas at the equilibrium pressure and temperature, ρ_h as density of sample holder, m_s as mass of adsorbent sample, ρ_s as density of adsorbent's solid matrix and q_{exc} as specific excess adsorption.

Since He measurements assume that the gas does is not adsorbed, Equation 3.1. is simplified (see Equation 3.2.).

$$m = m_{\mathrm{h}}\left(1 - \frac{\rho_{\mathrm{g}}}{\rho_{\mathrm{h}}}\right) + m_{\mathrm{s}}\left(1 - \frac{\rho_{\mathrm{g}}}{\rho_{\mathrm{s}}}\right) \qquad (\mathrm{Eq.\,3.2.})$$

Rearranging Equation 3.2., it's possible to obtain Equation 3.3.

$$m - m_{\mathrm{h}}\left(1 - \frac{\rho_{\mathrm{g}}}{\rho_{\mathrm{h}}}\right) = m_{\mathrm{s}} - \frac{m_{\mathrm{s}}}{\rho_{\mathrm{s}}}\rho_{\mathrm{g}} \qquad (\mathrm{Eq.\,3.3.})$$

This is a $y=mx+b$ linear type of equation. Whenever performing He measurements of this kind, one graph is essential: 'apparent' mass as a function of gas density. It should present a decreasing linear tendency with a $R^2 \approx 1$, although at very low pressures (0-0.5 bar) there might be a slight increase on the "apparent" mass, nevertheless negligible.

The gas density-dependent 'apparent' mass graph is essentially what is expressed in Equation 3.3., but overlooking the sample holder correction for buoyancy. So, one obtains the mass of the solid matrix by knowing the intercept and the volume of solid matrix by determining the slope. To both these values, one deducts the mass and the volume of the sample holder, respectively. The mass and volume of the solid matrix are finally obtained; a simple quotient between mass and volume gives the density of the solid matrix, pivotal for excess adsorption.

3.3.2. N_2 Adsorption-Desorption Isotherm at 77 K

N_2 adsorption equilibrium measurement at 77 K is a common but most relevant textural characterization technique for a given adsorbent material. It allows the determination several key properties of the adsorbent. These measurements were made using a Micromeritics ASAP (Accelerated Surface Area and Porosimetry System) 2010 static volumetric apparatus. Total pore volume, micropore volume, BET and Langmuir specific surface areas and pore size distribution (assuming slit-shaped pores) are determined.

3.3.3. Powder X-Ray Diffraction (PXRD)

Powder X-Ray Diffraction (PXRD) is a technique used to study the structure of a crystalline material, in this case an adsorbent. The obtained results identify the characteristic peaks of a material. For the IL@ZIF-8 materials it is an important analysis since the composite should present the characteristic peaks of ZIF-8; this would confirm the absence of structural changes from IL impregnation. PXRD patterns were obtained using a Rigaku MinFlex II equipment, carried out between 2Θ values of 2 ° and 50 ° with a step of 0.02 ° for all IL@ZIF-8 materials. ZIF-8 had been previously analysed between 2Θ values of 2 ° and 60 ° with a step of 0.02 °.

3.3.4. Fourier Transform Infrared Spectroscopy (FT-IR)

Fourier Transform Infrared Spectroscopy (FT-IR) gives useful information about the structure and interactions between the molecules; these interactions can be monitored by the shift in band positions. For IL@ZIF-8 materials, this technique is the 'confirmation' technique for IL impregnation since the infrared bands of the MOF and the incorporated IL should be present on the composite's spectra. For FT-IR measurements, a FT-IR Spectrometer Spectrum Two model (PerkinElmer) was used. For ILs, the ATR modulus was used for measurements and a single drop was necessary as long as the diamond square was completely covered with the liquid. As for ZIF-8 and IL@ZIF-8 composites, measurements were made using the Transmittance modulus that requires the manufacture of a KBr (Panreac) disc containing a small amount of material in order to produce the wanted spectra. Appendix E uncovers the procedure in the making of KBr tablets.

3.3.5. Scanning Electron Microscopy (SEM)

Scannig Electron Microscopy (SEM) permits to evaluate the structure (morphology) of a material. A focused beam of electrons scans the surface of the material and its morphology is observed and registered. SEM analysis was performed at Cenimat/i3N (FCT-UNL) on a Zeiss Auriga CrossBeam Workstation SEM-FIB equipment.

3.3.6. Adsorption Equilibrium Measurements using a Volumetric/Manometric Unit

The first adsorption equilibrium measurements for this thesis were made resorting to a volumetric/manometric apparatus constructed in-house [92]. It consists of an inlet of gas line and two experimental lines that can be used to simultaneously study two adsorbents, each line possessing a temperature indicator, a pressure transducer that can measure up to 20 bar, a reference volume and a cell that is inside an oven (Nabertherm Controller B170). The oven can operate over the range of 30-1100 °C, although a realistic range for application in typical adsorption studies can be 30-300 °C. Lines to exhaustion and to a vacuum pump (Edwards RV3 model) also exist should one need to decrease the pressure inside the apparatus or work below atmospheric pressure conditions, respectively. The lines are built with 1/16 stainless steel tubing. Though the apparatus has suffered some modifications since it was built and firstly tested, as of July 2017 the apparatus' design is the one presented in Figure 3.3.

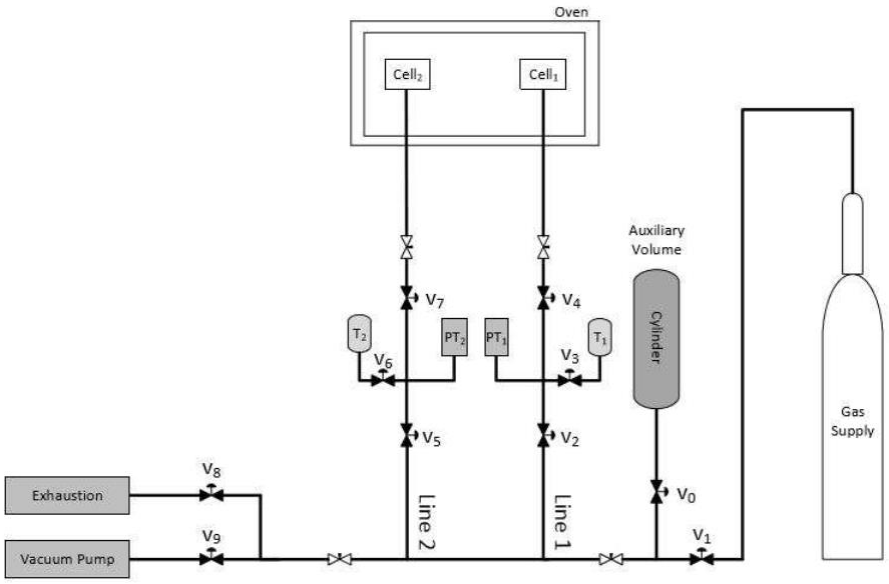

Figure 3.3. Volumetric apparatus schematic [99]. V – valves; PT – pressure transducer; T – temperature transducer.

In order to start an adsorption equilibrium measurement, the samples need to be degassed, i.e., impurities and/or moisture are removed by an *in situ* thermal treatment under vacuum. The adsorbent-containing cells are heated usually at a 2 °C/min rate until a temperature plateau (that is normally defined from the TGA analysis results) is reached, lasting 3-4 hours. The degassing temperature for ZIF-8 is 100 °C.

Figure 3.4. shows the volumetric apparatus whereas Figure 3.5. highlights the adsorbent cell parts, its interior and how they are coupled to the apparatus.

Figure 3.4. The actual volumetric apparatus.

Figure 3.5. Sample cell (left side) and its coupling to the apparatus (right side).

Before any kind of measurements, and even before degassing, the apparatus needs to be checked out for any gas leaks. Testing gas leaks is probably the trickiest, albeit crucial, part before the adsorption measurements *per se*. Since volumetric/manometric measurements are associated to a mass balance and any kind of pressure drop is interpreted as gas adsorbed by the sample, one can get erroneous results if a tiny leak exists. The leaks are tested by pressurizing the apparatus with He based on the assumption that this gas does not adsorb [100]. After that, the apparatus must be calibrated regarding the volumes of the lines. Any physical modification of the apparatus leads to a necessary re-calibration because the volumes of the lines will change. In that case, the reference volumes (V_{REF}) and cell volumes (V_{cell}) must also be determined. V_{REF1} stands for the reference volume on Line 1 and corresponds to the volume contained between

valves V_2 and V_4, with valve V_3 opened (see Figure 3.3.). V_{REF2} stands for the reference volume on Line 2 and corresponds to the volume contained between valves V_5 and V_7, with valve V_6 opened. These volumes are determined with the help of a previously calibrated auxiliary volume, whose volume is 334.11 cm^3 [101].

V_{cell1} and V_{cell2} are the $Cell_1$ and $Cell_2$ volumes, respectively. The former comprises of the volume contained between valve V_4 and the interior volume of $Cell_1$. The latter comprises of the volume contained between valve V_7 and the interior volume of $Cell_2$.

Appendix F contains a detailed description of the calibration procedure of the volumetric/manometric apparatus. Table 3.4. presents the reference and cell mean volumes for Lines 1 and 2 employed in this work, as well as their respective standard deviations.

Table 3.4. Volumetric/manometric unit reference and cell volumes.

	Line 1	**Line 2**
V_{REF} (cm^3)	41.73±0.10	42.15±0.46
V_{cell} (cm^3)	6.590±0.007	6.688±0.008

The calibration procedure finally allows the volumetric apparatus' user to perform adsorption equilibrium measurements. Because the cells weigh over 0.5 kg, weighing is performed on a Mettler PM1200 model analytical balance[2] (maximum weight of 1200±0.0001 g). It should be highlighted that the volumetric/manometric unit was given an upgrade during this thesis' elaboration with the new cell coupling that simplifies the connection and disconnection of the adsorption cells. The new coupling has a sealing mechanism that prevents air from entering the cell and, thus, the adsorbent remains impurity-free when the cells are disconnected from the unit for mass measurement.

After the cells are connected to their respective lines, degassing is the following step. Sample mass is then again measured and compared with the sample mass pre-degassing in order to quantify the (percentage of) mass loss during that process. The oven is then left cooling until the temperature programmed for the measurement is reached.

Figure 3.6. shows the in-house Labview developed software.

[2] Kindly lent by Professor Manuel Nunes da Ponte, Full Professor, LAQV-REQUIMTE, FCT/UNL, Lisbon, Portugal.

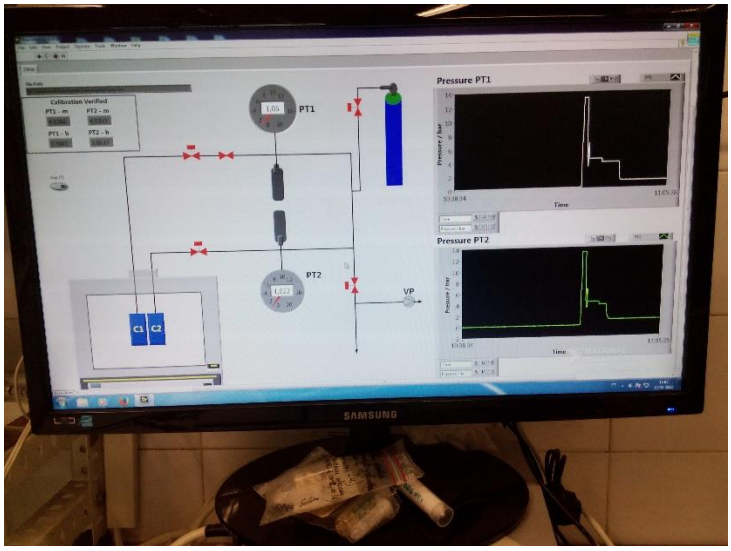

Figure 3.6. In-house developed software layout for pressure readings on the volumetric apparatus.

Adopting the nomenclature indicated in Figure 3.3., and only considering Line 1 (the process is analogous for Line 2, *mutatis mutandis*), an adsorption point measurement begins with valves V_2 and V_4 closed. An inlet of gas is fed to the apparatus by opening valve V_1. Valve V_2 then is opened and the gas enters the reference volume V_{REF1} until the desired pressure is reached, after which valve V_2 is closed. Usually, 10 minutes are considered enough for temperature and pressure stabilizations. After that 10-minute period, gas is expanded to the cell by opening valve V_4. It is noteworthy to point out that when in the adsorption branch, this expansion leads to a pressure drop whereas on the desorption branch it will result on a pressure increase. So, for instances, if a point at 3 bar is pretended, it's mandatory to pressurize V_{REF1} with a somewhat higher pressure. These variations in pressure upon expansion to the cell depend on the gas and adsorbent's natures. After the referred expansion, at least 1 hour is granted for temperature and pressure stabilization. Adsorption equilibrium is considered reached when the mean pressure is constant with variations smaller than 0.01 bar (the error of the pressure transducers employed). After adsorption equilibrium is reached, valve V_4 is closed, the apparatus feed line is purged with the supply gas and the reference volume V_{REF1} is again pressurized, following the above-mentioned procedure. When desorption is intended, the reference volume V_{REF1} is through the exhaustion or vacuum lines.

Appendix G indicates with additional detail of the procedure for volumetric/manometric adsorption equilibrium measurements using this in-house apparatus.

Adsorption equilibrium can be reported using different definitions. But first, it is important to clarify that, for adsorption on a two-dimensional surface, interactions between the gas and the surface will weaken with increasing distance until attractive forces cease to exist, becoming negligible. At this distance, an imaginary line called Gibbs dividing surface can be drawn, dividing the total free volume into adsorbed and bulk phases. The absolute amount adsorbed, m_{abs}, is the total number of molecules in the adsorbed area. Absolute adsorption cannot be directly measured since it's

impossible to determine where the Gibbs dividing surface is located or to define the size of the adsorbed region experimentally [102].

Because of that, normally measurements are given in excess adsorption, m_{exc}, which corresponds to the amount of adsorbate put into contact with the adsorbent discounting the amount of gas that remains in the gas phase after system stabilization [92]. All adsorption obtained data come intrinsically in excess. Equation 3.4. shows how excess adsorption can be calculated in grams, while Equation 3.5. denotes the excess gas adsorbed per unit mass of adsorbent (mol gas/kg adsorbent).

$$m_{\mathrm{exc,f}} = m_{\mathrm{exc,i}} + V_{\mathrm{REF}} \left(\rho_{\mathrm{REF,i}} - \rho_{\mathrm{REF,f}}\right) + \left(\rho_{\mathrm{cell,i}} - \rho_{\mathrm{cell,f}}\right) \left(V_{\mathrm{cell}} - V_s\right) \qquad (\mathrm{Eq.\,3.4.})$$

$$q_{\mathrm{exc}} = \frac{m_{\mathrm{exc}}}{m_s\, MW} \qquad (\mathrm{Eq.\,3.5.})$$

with $m_{exc,f}$ as final excess amount adsorbed, $m_{exc,i}$ as initial excess amount adsorbed, $m_{exc,f}$ as final excess amount adsorbed, V_{REF} as reference volume, $\rho_{REF,i}$ as initial density of bulk gas in the reference volume, $\rho_{REF,f}$ as final density of bulk gas in the reference volume, V_{cell} as cell volume, V_s as solid volume and MW as molecular weight of the gas.

Another way is to show data in total adsorption, which accounts for all the gas molecules within the pores of an adsorbent. It is an approximation to absolute adsorption in microporous materials and is related to excess adsorption [102], as shown by Equation 3.6 (expressed in mol gas/kg adsorbent).

$$q_{\mathrm{t}} = q_{\mathrm{exc}} + \frac{V_{\mathrm{p}}\, \rho_{\mathrm{cell,f}}}{MW} \qquad (\mathrm{Eq.\,3.6.})$$

with q_t as specific total adsorption and V_p as total pore volume.

Figure 3.7. illustrates excess and total adsorption concepts.

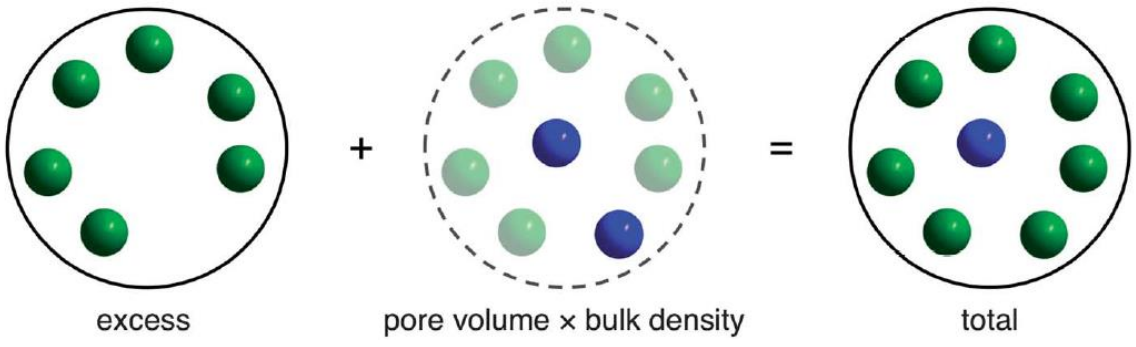

Figure 3.7. Schematic representation of excess and total adsorption. Green balls represent adsorbed molecules and blue ones denote bulk gas molecules [102]. Excess adsorption accounts only for the adsorbed gas molecules while total adsorption accounts for the same adsorbed gas molecules plus bulk gas that would have been present in the pore volume in the absence of adsorption, i.e., all gas molecules inside the total pore volume.

A more recent concept is the net adsorption, which can be described as 'the total amount of gas present in the container with the adsorbent minus the amount that would be present in the empty container (without the adsorbent) at the same temperature and pressure' [103]. It is a useful concept since it does not depend on the volume nor the density of the solid matrix. This way, reporting net adsorption equilibria data avoids the need for adsorbent characterization with He pycnometry which is based in the assumption this gas is not adsorbed. Equation 3.7. shows how net adsorption can be calculated in grams, while Equation 3.8. denotes the specific net gas adsorbed per unit mass of adsorbent (mol gas/kg adsorbent).

$$m_{\mathrm{net,f}} = m_{\mathrm{net,i}} + V_{\mathrm{REF}} \left(\rho_{\mathrm{REF,i}} - \rho_{\mathrm{REF,f}}\right) + \left(\rho_{\mathrm{cell,i}} - \rho_{\mathrm{cell,f}}\right) V_{cell} \qquad (\mathrm{Eq.\ 3.7.})$$

$$q_{\mathrm{net}} = \frac{m_{\mathrm{net}}}{m_{\mathrm{s}}\, MW} \qquad (\mathrm{Eq.\ 3.8.})$$

with $m_{\mathrm{net,f}}$ as final net amount adsorbed and $m_{\mathrm{net,i}}$ as initial net amount adsorbed,

Excess, total and net adsorption isotherms for the same system are presented on Figure 3.8.

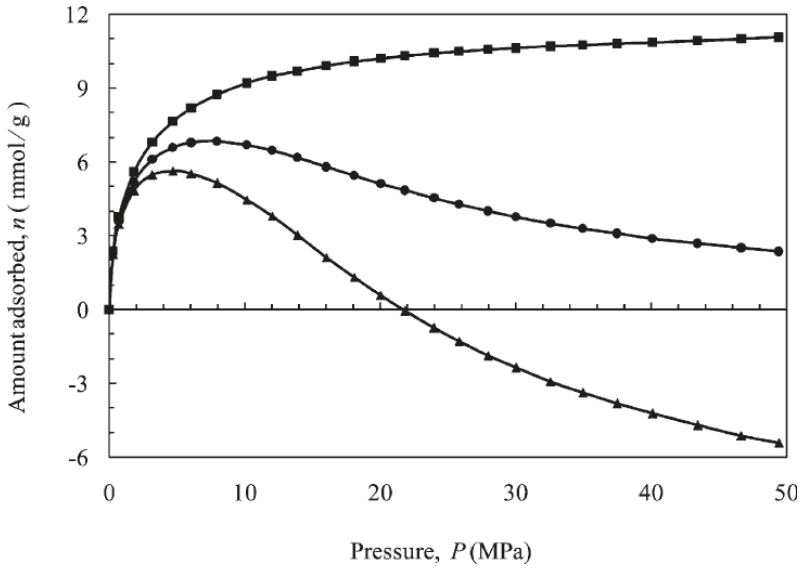

Figure 3.8. Difference between total (squares), excess (circles) and net (triangles) adsorption quantities [103]. Total adsorption increases monotonically with pressure while excess and net adsorptions have a maximum. Net adsorptions can have negative amount of gas adsorbed.

Another important aspect that must be taken into account is the selectivity of the material towards CO_2/CH_4 separation. The ideal CO_2/CH_4 selectivity, $S_{CO2/CH4}$, is defined by Equation 3.9. when considering a given pressure.

$$S_{\mathrm{CO2/CH4}} = \frac{q_{\mathrm{t\ CO_2}}}{q_{\mathrm{t\ CH_4}}} \qquad (\mathrm{Eq.\ 3.9.})$$

This parameter measures the affinity of CO_2 in comparison to CH_4 towards their adsorption in a given adsorbent material. It is particularly useful to screen the best adsorbent for the topical CO_2/CH_4 separation of interest.

It became apparent during the making of this thesis that the only possible gain in incorporating the chosen ILs into ZIF-8 would be an increased selectivity by comparison to the pristine MOF.

In order to obtain an ideal selectivity, Sips equation (Equation 3.10.) was used to predict the adsorption isotherms in terms of total adsorbed amount quantities of the pure gases [73]. The sum of the differences between the experimental and the predicted adsorbed amounts is minimized using the *Solver* add-in from *Microsoft Excel*, changing the q_s, n and b parameters.

$$q = \frac{q_s (bP)^{\frac{1}{n}}}{1 + (bP)^{\frac{1}{n}}} \qquad \text{(Eq. 3.10.)}$$

with q as specific adsorbed amount, q_s as the maximum specific adsorbed amount, b as the affinity constant, P as total pressure and n as the heterogeneity parameter.

The q_s parameter is the maximum adsorbed amount that a material can have. The n parameter characterizes the system heterogeneity and is usually greater than unity; the larger the parameter the more heterogeneous the system is. The b parameter is the affinity constant and it measures how strongly an adsorbate molecule is attracted onto a surface; large affinity constant indicates that the surface is covered more with adsorbate molecules.

With readjusted parameters, CO_2 and CH_4 (total) adsorbed amounts can be calculated for the desired pressure range and, using Equation 4.2., selectivities are finally obtained.

3.3.7. Adsorption Equilibria Measurements using a Gravimetric Unit

In the course of this thesis, adsorption equilibrium measurements were also performed using a gravimetric unit. Two samples can be tested at the same time, similarly to the volumetric/manometric apparatus. It has two inlet lines of gas, one for He and another for the gas of interest. A gravimetric high-precision balance ISOSORP 2000 (Rubotherm GmbH) is the main feature of the unit. Temperature control inside the jacket containing the gas and sample holders is guaranteed by a precise Julabo F32-HE refrigerated/heating circulator (±0.1 °C). The pressure is read by several pressure transducers with different ranges to ensure good measurement accuracy at all pressures: Baratron model 627D (MKS Instruments GmbH, Germany) for 0–1 bar; Omegadyne Inc. models PX01C1-150A5T, PX01C1-500A5T, and PX03C1-3KA5T for 0–10, 0–35 bar and 0–138 bar, respectively. As previously reported, the pressure is monitored and recorded online using in-house developed software (*BioCTR*). Lines to exhaustion and to a vacuum pump (Edwards RV5 model) also exist should one need to decrease the pressure inside the apparatus or work below atmospheric pressure conditions, respectively. The lines are with 1/8 stainless steel tubing. The schematic for the unit is presented in Figure 3.9.

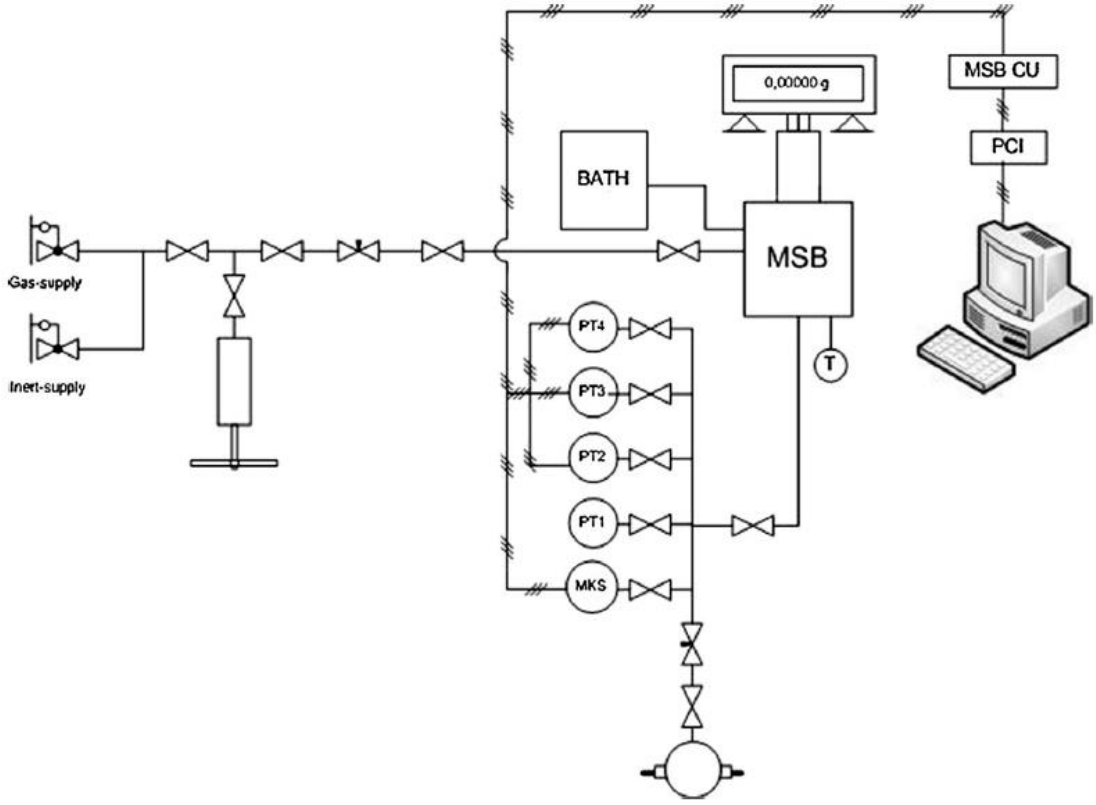

Figure 3.9. Schematic diagram of the gravimetric unit [97]. MSB – magnetic suspension balance; PT – pressure transducer; MKS - Baratron model 627D pressure transducer.

The microbalance can operate up to 100 °C and withstand 150. Figure 3.10 shows part of the experimental setup while Figure 3.11. shows the inside of the magnetic suspension balance.

Figure 3.10. Part of the gravimetric unit, highlighting the jacket containing the sample holders, the pressure transducers and the bath for temperature control (along with its respective probe).

Figure 3.11. The inside of the magnetic suspension balance.

In this apparatus, the measurement cell is coupled to a suspension magnet instead of hanging directly at the balance. Using this free suspension coupling, the measuring force is then transmitted contactlessly from the closed measurement cell to a Rubotherm microbalance, located outside under ambient atmosphere.

Adsorption measurements steps are quite similar to the volumetric apparatus. After guaranteeing the absence of leaks, the adsorbents are degassed. The IL@ZIF-8 samples are degassed at 100 °C for 3-4 hours under vacuum. After degassing, the system is set for the adsorption equilibrium measurements. The initial mass is measured (Point 0) and the apparatus is then pressurized with gas, logically disturbing temperature, pressure and mass readings The pressure, temperature and 'apparent' mass are then recorded after the adsorption equilibrium is reached, i.e., when the three quantities no longer present measurable variations (typically a minimum of 1 hour is needed to reach equilibrium)

An important feature of this experimental setup is the different ranges of pressure of each transducer. The Baratron gives pressure measurements between 0-1 bar; so, if a measurement is intended at 3 bar, the valve connecting this transducer to the balance must be closed. The same logic applies to the other transducers. Depressurizing the system is simply accomplished by opening the exhaustion valve as well as the one that gives admission to the transducers. Appendix H has additional details about the procedure for gravimetric adsorption equilibrium measurements using this setup. Figure 3.12. shows the layout of the software used for pressure recording and display.

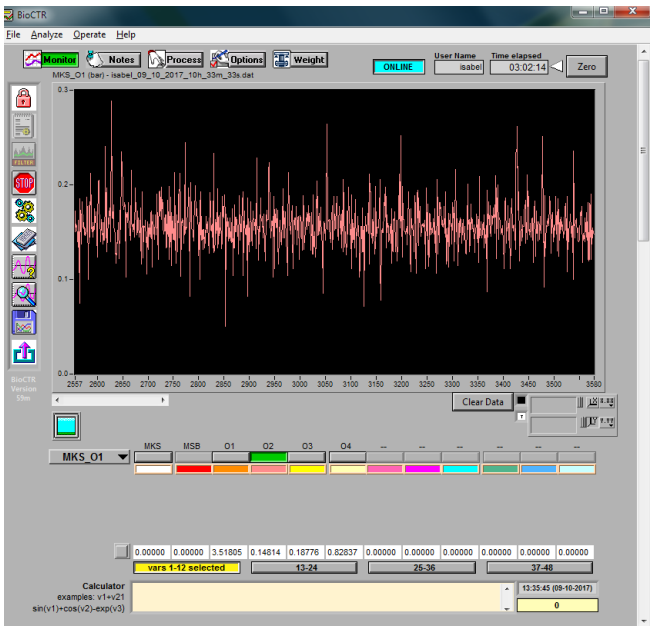

Figure 3.12. In-house developed software layout for pressure readings on the gravimetric apparatus.

As with volumetric measurements, gravimetric ones can be described in specific net, excess and total adsorption. Equations 3.11., 3.12. and 3.13. show how their respective calculations (expressed in mol gas/kg adsorbent) were done.

$$q_{\mathrm{net}} = \frac{m - m_{\mathrm{s}} - m_{\mathrm{h}} + V_{\mathrm{h}}\,\rho_{\mathrm{g}}}{m_{\mathrm{s}}\,MW} \qquad (\mathrm{Eq.\,311.})$$

$$q_{\mathrm{exc}} = q_{\mathrm{net}} + \frac{\frac{\rho_{\mathrm{g}}}{\rho_{\mathrm{s}}}}{MW} \qquad (\mathrm{Eq.\,3.12.})$$

$$q_{\mathrm{t}} = q_{\mathrm{exc}} + \frac{V_{\mathrm{p}}\,\rho_{\mathrm{g}}}{MW} \qquad (\mathrm{Eq.\,3.13.})$$

4. Experimental Results and Data Analysis

This chapter is divided into two parts:

- Evaluation of the influence of IL's structure on adsorption properties of the hybrid materials prepared, including all the textural characterization techniques indicated in Chapter 3, as well as adsorption equilibrium measurements of CO_2 and CH_4 on samples containing the same desired molar IL loading (see Table 3.3.);
- Testing IL's loading, in order to ascertain its impact on adsorption. Several characterization techniques included in Chapter 3 were performed in addition to adsorption equilibrium measurements.

4.1. Testing IL's Structure

The principal objective of this thesis is to assess how the impregnation of a ZIF-8 sample with an IL changes its adsorption capacity compared with the pristine adsorbent. Can one obtain higher adsorption capacities and/or improved selectivities with these new composites, thus enhancing the separation of CO_2/CH_4 gas mixtures by taking advantage of IL incorporation?

The next task is the interpretation of the obtained results, using the same molar IL loading. How can one understand the MOF-IL interaction responsible for the obtained adsorption results? For these purposes, nine IL-impregnated composite samples were fully characterized and adsorption equilibrium measurements for CH_4 and CO_2 were carried out.

Thermogravimetric Analysis

The degassing temperature of ZIF-8 is performed at 100 °C, as mentioned in section 3.3.6. This temperature is indicated by the ZIF-8 manufacturer (BASF SE, Germany) and it was confirmed through a thermogravimetric analysis of a ZIF-8 sample; the results can be seen in Figure 4.1.

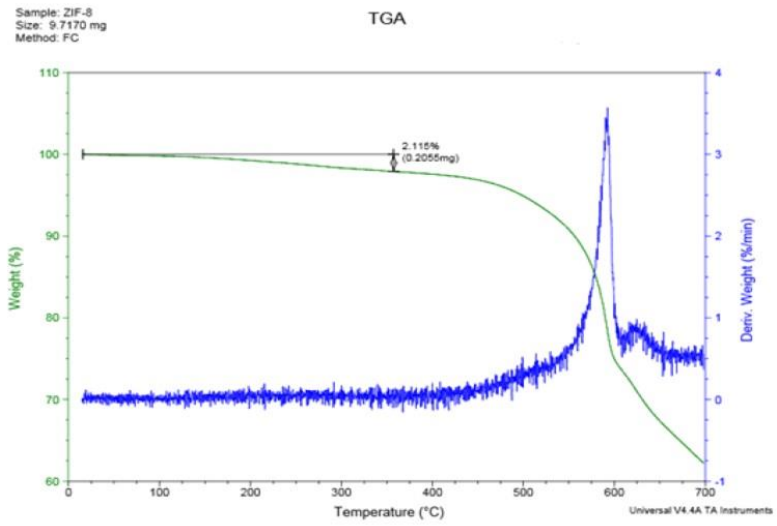

Figure 4.1. TGA of the ZIF-8 sample under N_2 atmosphere at heating rate of 5 °C/min.

By presenting the weight loss percentage (green curve) as a function of temperature, it is possible to observe in Figure 4.1. that the ZIF-8 structure is stable up to 400 °C. From this point on, ZIF-8 begins to degrade. This material 'can be activated at 100 °C (under vacuum)' according to BASF SE producer (Germany); its TGA confirms that degassing at this temperature can be done with negligible mass loss.

The thermogravimetric analysis for the ILs were not performed, since their usual degradation temperature is always higher than 100 °C, which is the degassing temperature assumed for ZIF-8 [104].

4.1.1. He Pycnometry

The density of the solid matrix of IL-impregnated ZIF-8 samples was obtained via He pycnometry. The calculations for obtaining the density from raw data are made according to the mathematical framework shown in section 3.3.1. The experimental measurements were performed with a gravimetric apparatus already available in the laboratory (see section 3.3.7.).

Table 4.1. presents the experimental solid matrix densities and the pure ILs density used for each composite at 60 °C and 1 bar. The He pycnometry was performed at the temperature of 60 °C in order to minimize the already minimal gas adsorption. Higher temperatures were avoided, since the apparatus was maintained overnight during the degassing, temperature stabilization and picnometry measurements. Appendix I has pure IL densities between 5 and 100 °C at 1 bar while Appendix J contains all the collected data related to He pycnometry.

Table 4.1. Experimental composites' solid matrix densities and respective pure IL density (60 °C, 1 bar).

Sample	ρ_s obtained (g/cm^3)	Pure IL density (g/cm^3)
ZIF-8	1.49	-
C2@ZIF-8	1.41	1.482
C10@ZIF-8	1.34	1.246
Bz@ZIF-8	1.54	1.457
C2OH@ZIF-8	1.48	1.540
C6B(CN)4@ZIF-8	1.29	0.966
C6N(CN)2@ZIF-8	1.43	1.008
C6Cl@ZIF-8	1.54	1.021
C2Ac@ZIF-8	1.42	1.078
P66614@ZIF-8	1.25	1.041

The density of the pure ILs used in this work varies from 0.966 to 1.540 g/cm^3. However, the changes on the solid matrix density of the composites cannot be explained only by the density of the IL used in the composite. This indicates that there should be some specific interactions between some ILs and ZIF-8 that are also responsible for the density values observed.

It should be pointed out that this technique presents a limitation. Solid matrix density is obtained considering the intercept and slope of plotting apparent mass as a function of helium density. Small errors on these values can modify the linear fitting significantly, changing (or at the very least, introducing uncertainty to) the density value.

4.1.2. N_2 Adsorption-Desorption Isotherms at 77 K

To determine the specific surface area of the composite samples, N_2 adsorption-desorption equilibrium measurements at 77 K were performed and analysed. The complete set of isotherms can be seen in Figure 4.2. and are all Type I, typical of microporous materials, according to IUPAC classification [70] (see Figure 2.14.). The adsorption-desorption data of ZIF-8 is consistent with results found in open literature [90].

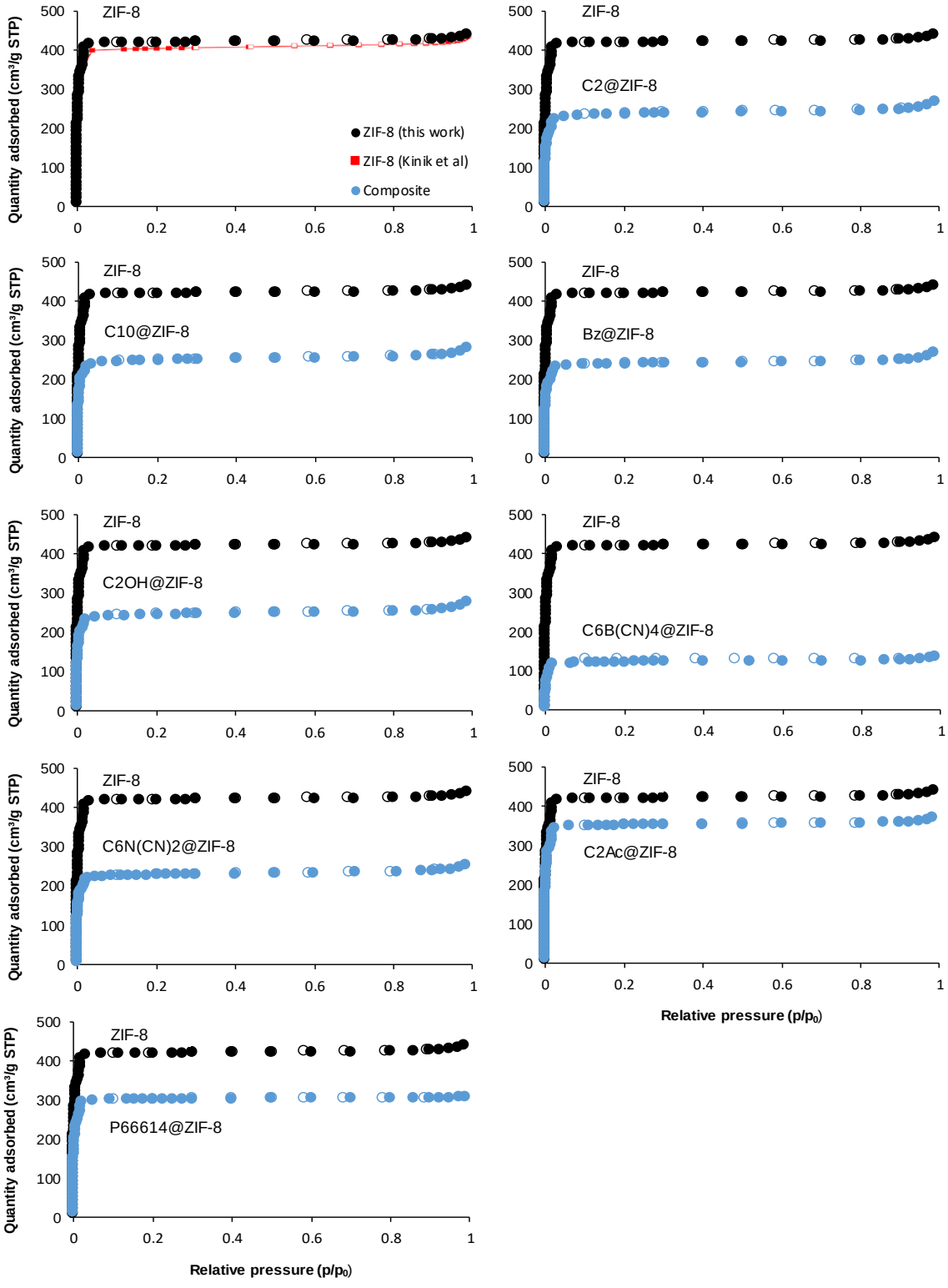

Figure 4.2. N_2 adsorption-desorption isotherms at 77 K of ZIF-8 and manufactured IL@ZIF-8 composites. Closed and open symbols denote adsorption and desorption data, respectively.

Table 4.2. shows the obtained BET and Langmuir specific surface areas, as well as the total pore volume of each material studied. Note that the classical BET data treatment assumes a general relative pressure p/p_0 in the range of 0.05 and 0.35, where p and p_0 are the equilibrium and

saturation pressures of the adsorbate at the temperature of adsorption. If the material under analysis is highly microporous, this range must be enlarged to include all the points at the lower pressure range. This was considered herein this thesis. Alternatively, for highly microporous materials of solids with narrow micropores that exhibit the typical Type I (see Figure 2.14.) adsorption-desorption isotherms of N_2 at 77 K, some authors consider more appropriate to use the Langmuir analysis. As can be seen in Table 4.2., the specific BET and Langmuir surface areas are quite comparable, although the Langmuir values are always slightly larger than their BET counterparts. The obtained values for BET and Langmuir specific surface areas along with the total pore volume of ZIF-8 are fairly consistent with the open literature reported results [105].

Table 4.2. BET specific surface area and respective *c* constant, Langmuir specific surface area, total pore volume and respective partial pressure for ZIF-8 and IL@ZIF-8 composites, obtained using the *MicroActive* software.

Sample	BET specific surface area (m^2/g)	*c*	Langmuir specific surface area (m^2/g)	Total pore volume (cm^3/g)	p/p_0
ZIF-8	1907±81	407	2008±83	0.67	0.97
ZIF-8 [105]	1851	-	2101	0.71	-
C2@ZIF-8	1055±58	339	1094±64	0.40	0.97
C10@ZIF-8	1075±20	445	1132±21	0.42	0.97
Bz@ZIF-8	1052±41	390	1093±47	0.40	0.97
C2OH@ZIF-8	1031±20	574	1096±19	0.41	0.97
C6B(CN)4@ZIF-8	552±33	402	566±36	0.20	0.97
C6N(CN)2@ZIF-8	1081±28	239	1140±29	0.38	0.97
C6Cl@ZIF-8	N.A.	N.A.	N.A.	N.A.	N.A.
C2Ac@ZIF-8	1558±60	448	1609±65	0.56	0.97
P66614@ZIF-8	1490±77	222	1553±84	0.47	0.97

Figure 4.3. shows that all composites reveal both specific surface area and total pore volume loss, when compared to pristine ZIF-8.

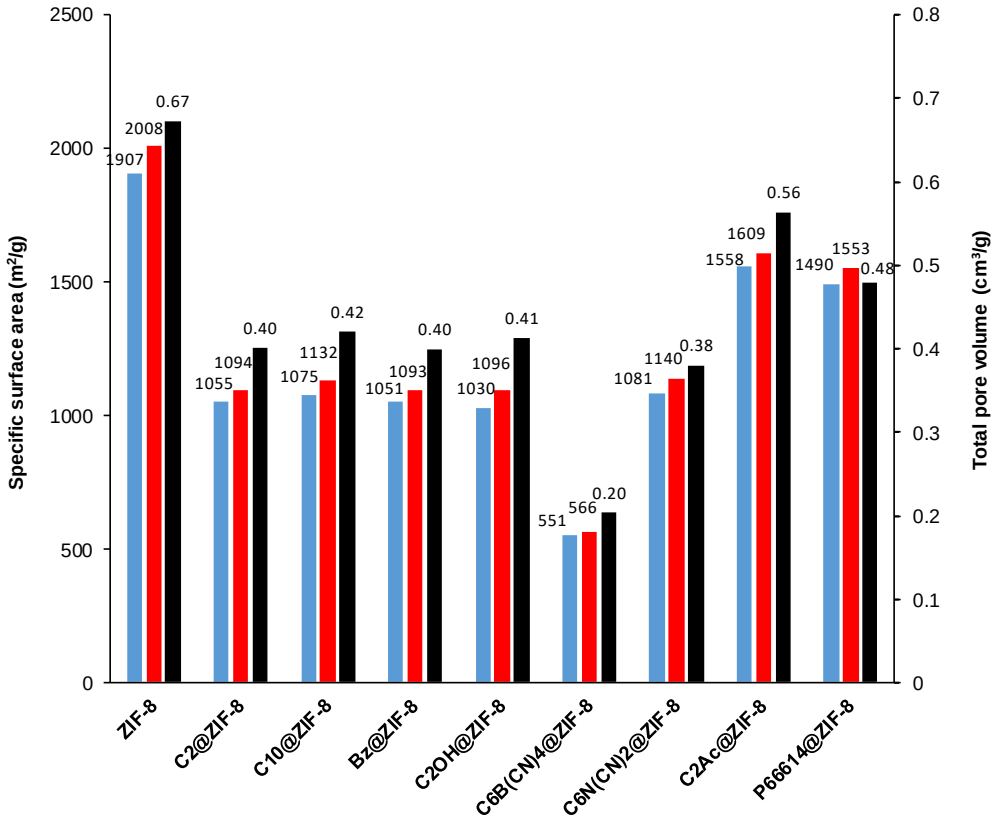

Figure 4.3. Obtained BET (**blue**) and Langmuir (**red**) specific surface areas and total pore volume (**black**) data for ZIF-8 and IL@ZIF-8 composites.

Specific surface area and total pore volume loss is the result of the IL partially occupying the pores. While for most composites specific surface area loss and total pore volume loss is between 20- 50% and 30-40% respectively, the C6B(CN)4@ZIF-8 composite has more than 70% loss in both properties. It is not yet clear why such a drastic decrease occurs. A possible explanation could be the size of the anion: being small, its arrangement inside the ZIF-8 structure can be such that it reduces specific surface area and total pore volume more considerably than other ILs. But C2Ac@ZIF-8 also has a small anion and has the largest specific surface areas and total pore volume of all composites. Nevertheless, the other results show good consistency: since the same amount of IL moles were incorporated in each sample, all materials should present similar specific surface areas and total pore volume.

Additionally, non-linear density functional theory (NLDFT) analysis was performed with the resulting data of N_2 adsorption/desorption at 77 K, providing the pore size distribution for each composite sample, as shown in Figure 4.4.

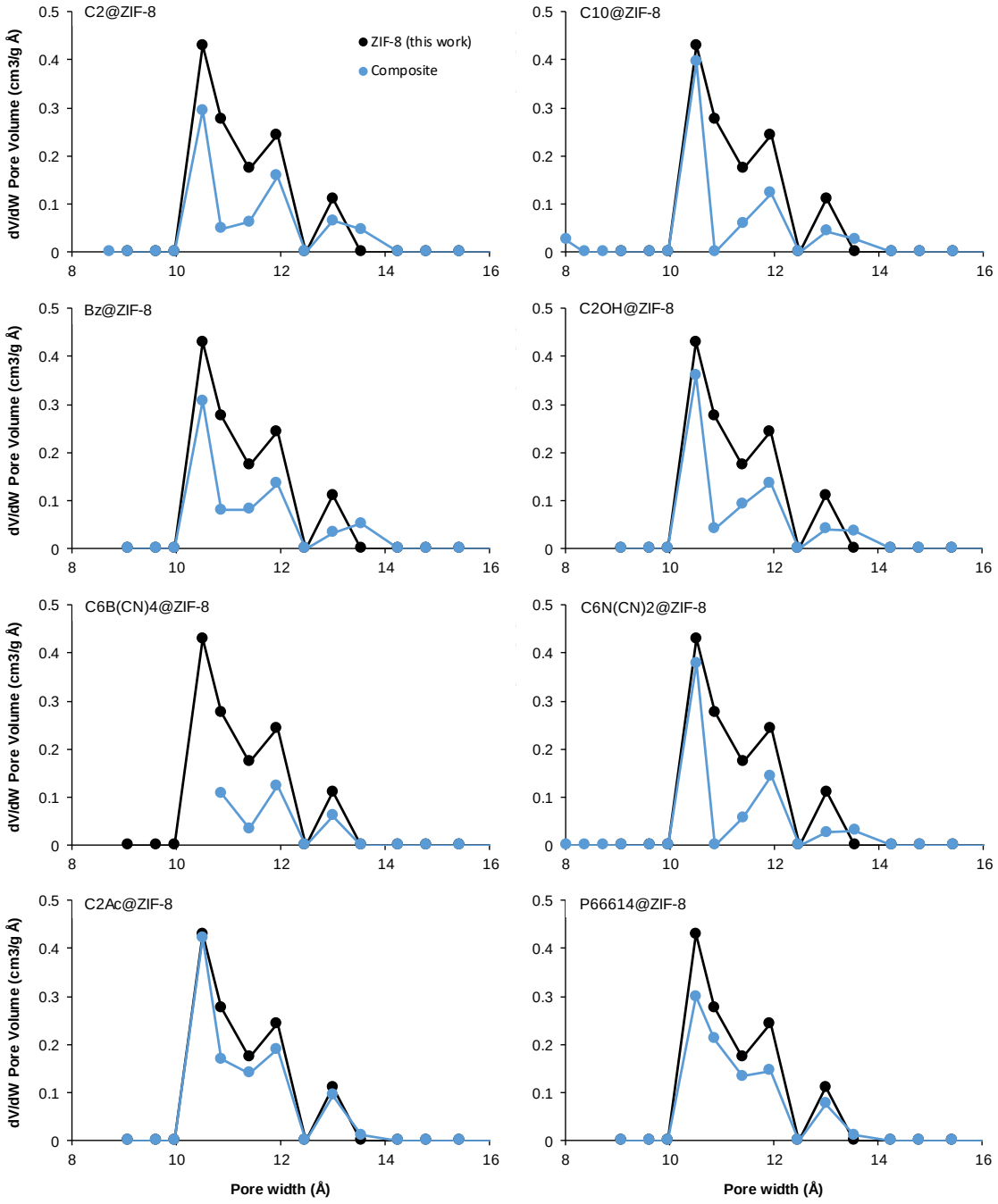

Figure 4.4. Pore size distribution through NLDFT analysis of ZIF-8 and IL@ZIF-8 composites.

This analysis shows that all composite samples seem to follow the ZIF-8 pore size distribution, with an evident and logical decrease on available pores due to IL partial occupancy. Furthermore, it confirms that ZIF-8 and IL@ZIF-8 composites are microporous materials, according to IUPAC definition [73].

It's worth noting that C6B(CN)4@ZIF-8 pore size distribution seems incomplete. An explanation for this fact could to be related to a different adopted experimental procedure when measuring the N_2 adsorption-desorption isotherm at 77 K.

4.1.3. Powder X-Ray Diffraction (PXRD)

This characterization technique can be used for several purposes, but the one of interest in this case is to evaluate if the structure within the framework of ZIF-8 upon IL incorporation is conserved. This can be verified by comparing the obtained pattern of ZIF-8 with the ones obtained for each composite material, as depicted in Figure 4.5. The ZIF-8 data are consistent with results reported in the open literature, where it is stated that ZIF-8 is a crystalline material [35, 106, 107].

PXRD data shows that there is little to no structural changes within the framework of ZIF-8 due to IL impregnation. The intensity of peaks of all composites, when comparing to ZIF-8, hardly changes; nevertheless, there are two common exceptions around 2Θ=7.5 ° and 2Θ=16.5 °. These two peaks usually decrease and increase in composites' spectra, respectively. These two particular alterations in all composites indicate that the electron density of ZIF-8 changes after IL impregnation. While this seems to be a consequence of the addition of IL into the ZIF-8 framework, changes in intensity can also be caused (but not limited to) by partial decomposition of the sample, sample preparation for PXRD analysis, preferred orientation of the material, instrument alignment, etc. [90]. PXRD results suggest that IL impregnation of ZIF-8 does not affect the MOF's structure and, for that reason, these composite materials are all crystalline.

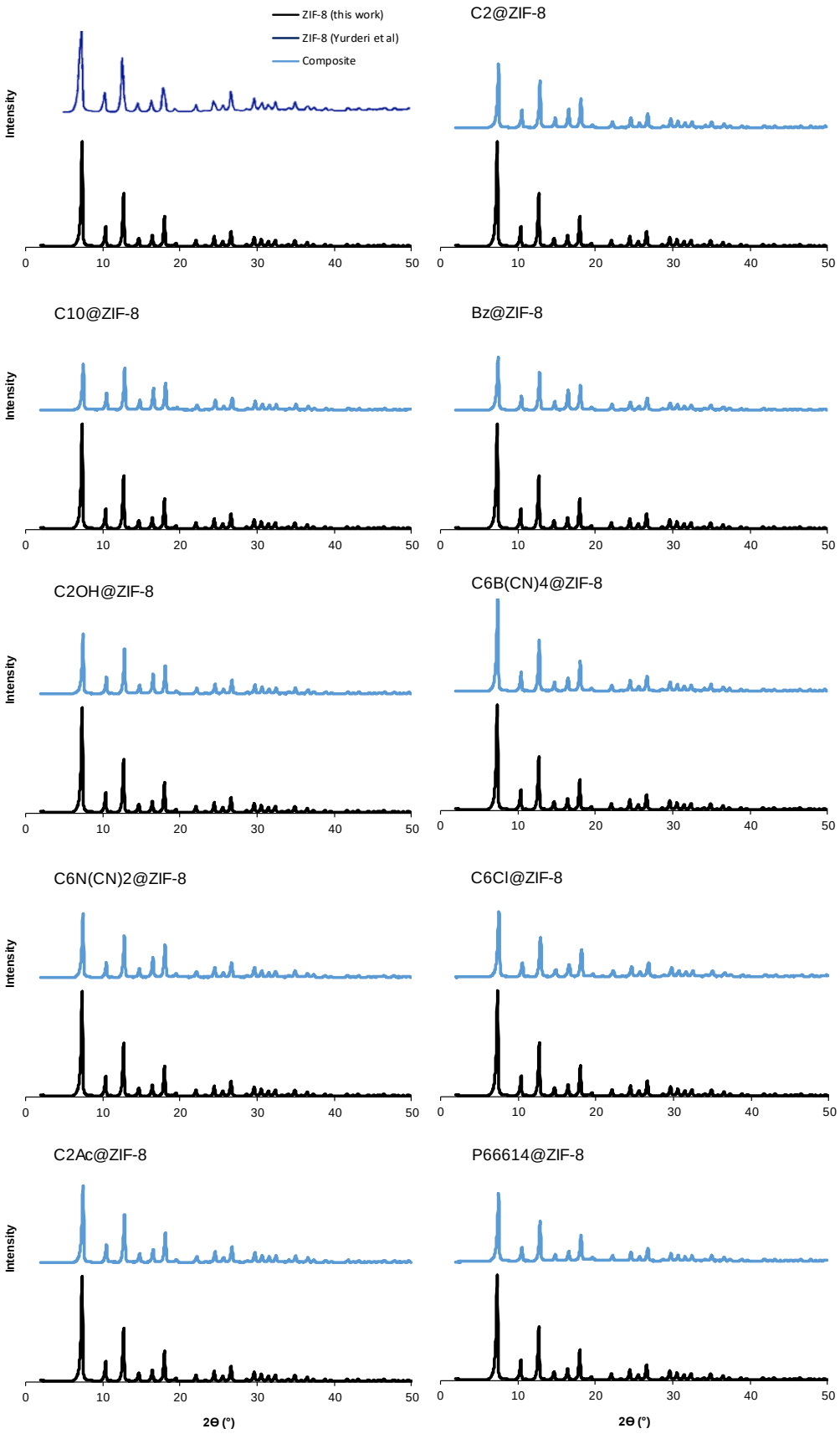

Figure 4.5. PXRD spectra of ZIF-8 and IL@ZIF-8 composites.

4.1.4. Fourier Transform Infrared Spectroscopy (FT-IR)

Changes in peaks' intensity found in the composites' PXRD pattern do somewhat corroborate the idea that IL impregnation was successful. In order to confirm this idea, FT-IR spectra of ZIF-8, of all ILs and all composite materials were acquired; they consist of bands that are associated to specific chemical bonds' vibrations. When a molecule is composed of *n* atoms, it has 3*n* degrees of freedom; six of them are translations and rotations of the molecule itself. This leaves 3*n*-6 degrees of vibrational freedom (or 3*n*-5 if the molecule is linear). Vibrational modes usually have descriptive names, such as stretching, bending, scissoring, rocking and twisting [108]. It was considered relevant for this thesis to mainly check if the IL's bands are present in the corresponding composite's pattern since this is what confirms a successful IL impregnation. Bands' analysis is therefore made in a non-exhaustive manner and band assignments can be done with the help of Table 4.3. Figure 4.6. shows that ZIF-8 FT-IR data are consistent with other reported results in the open literature [106, 109].

Table 4.3. FT-IR bands assignments.

Assignment	Characteristic absorption (cm^{-1})	Reference
C-H stretching (aromatic)	3100-3000	[110]
C-H stretching (aliphatic)	3000-2800	[110]
CH_3 symmetrical stretching	2960	[110]
CH_2 asymmetric stretching	2930	[110]
CH_3 asymmetric stretching	2870	[110]
CH_2 symmetric stretching	2850	[110]
C≡N stretching (aliphatic)	2260-2240	[108]
C-N stretching (aliphatic)	~2220-2120	[111]
C=O stretching	1740-1630	[110]
C=C stretching (imidazole ring)	1610	[110]
C=N stretching	1584	[112]
C=N stretching (imidazole ring)	1578	[110]
Imidazole ring stretching	1500-1350	[112]
CH_3 asymmetrical bending	1475	[110]
CH_2 scissoring	1465	[110]
C-F stretching	1400-1000	[110]
CH_3 symmetrical bending	1380	[110]
C-N stretching (aromatic)	1360-1250	[110]
O=S=O asymmetrical stretching	~1350	[113]
Imidazole ring bending in-plane	1350-900	[112]
CH_2 wagging	1305	[110]
CH_2 twisting	1300	[110]
C-H bending out-of-plane (aromatic)	1275-1000	[110]
$C-F_3$ stretching	~1250-1190	[113]

Table 4.3. continued

Assignment	Characteristic absorption (cm^{-1})	Reference
O=S=O symmetrical stretching	~1150	[113]
N-S stretching	~1060	[113]
N-S stretching	912-866	[114]
C-H bending in-plane (aromatic)	900-690	[110]
N shuttling	< 800	[113]
Imidazole ring bending out-of-plane	< 800	[112]
CH_2 rocking	720	[110]
C-S stretching	700-600	[110]
Zn-N stretching	421	[112]

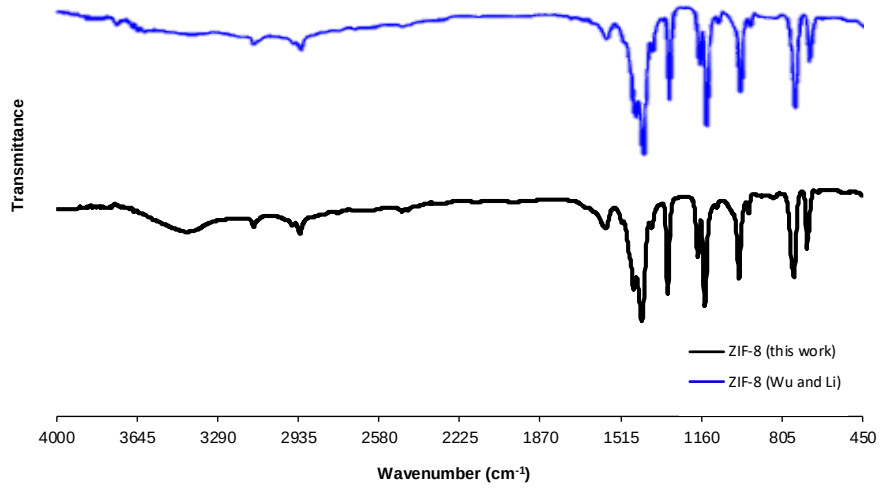

Figure 4.6. Comparison between obtained and open literature ZIF-8 FT-IR data.

Figure 4.7. shows FT-IR spectra of ZIF-8 and IL@ZIF-8 composites, detailing the low wavenumber region since it's where bending-related bands can appear.

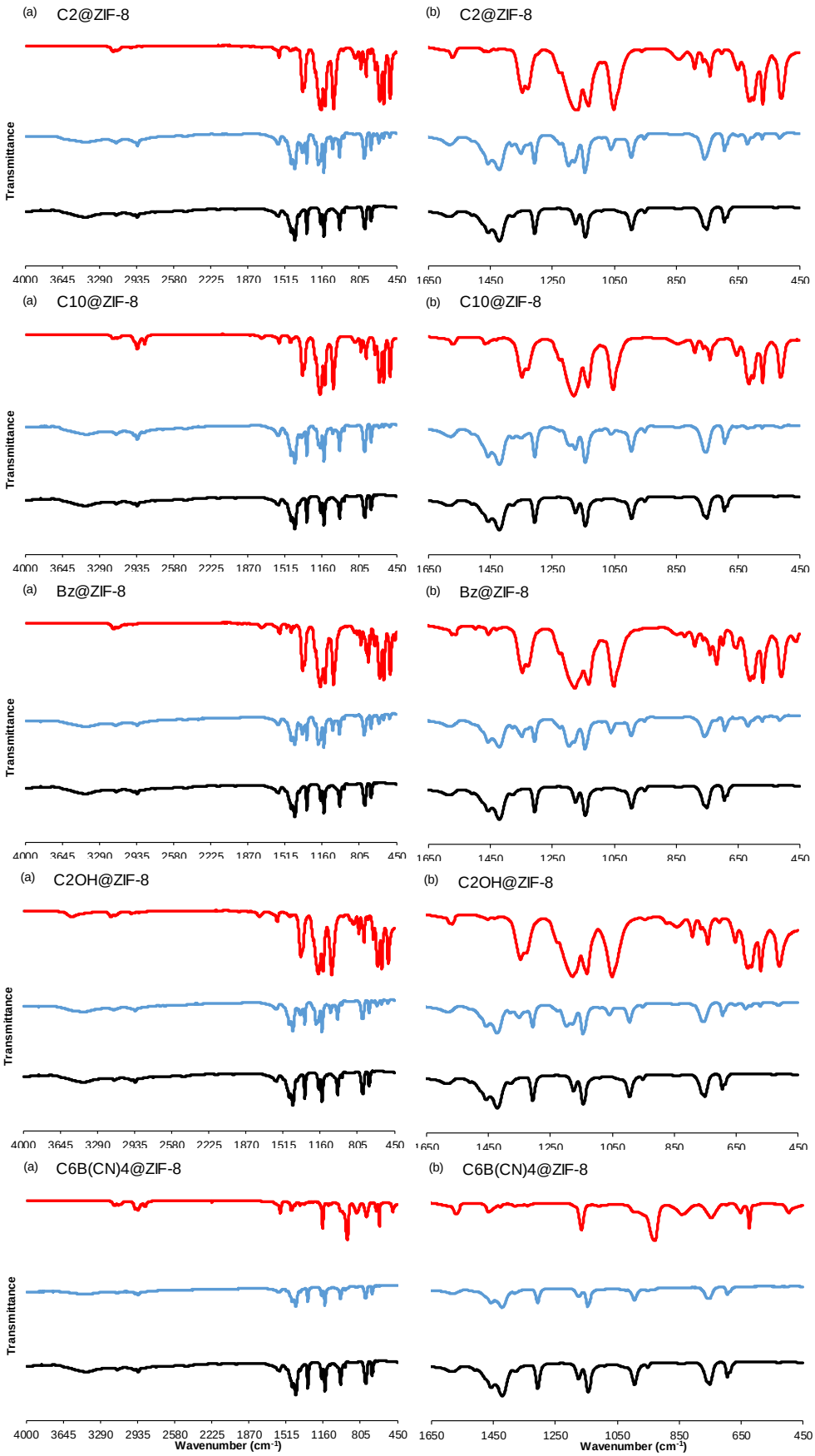

Figure 4.7. Obtained FT-IR spectra of ILs (**red**), IL@ZIF-8 composites (**blue**) and ZIF-8 (**black**), between (a) 4000 and 450 cm^{-1} and (b) 1650 and 450 cm^{-1} (part 1).

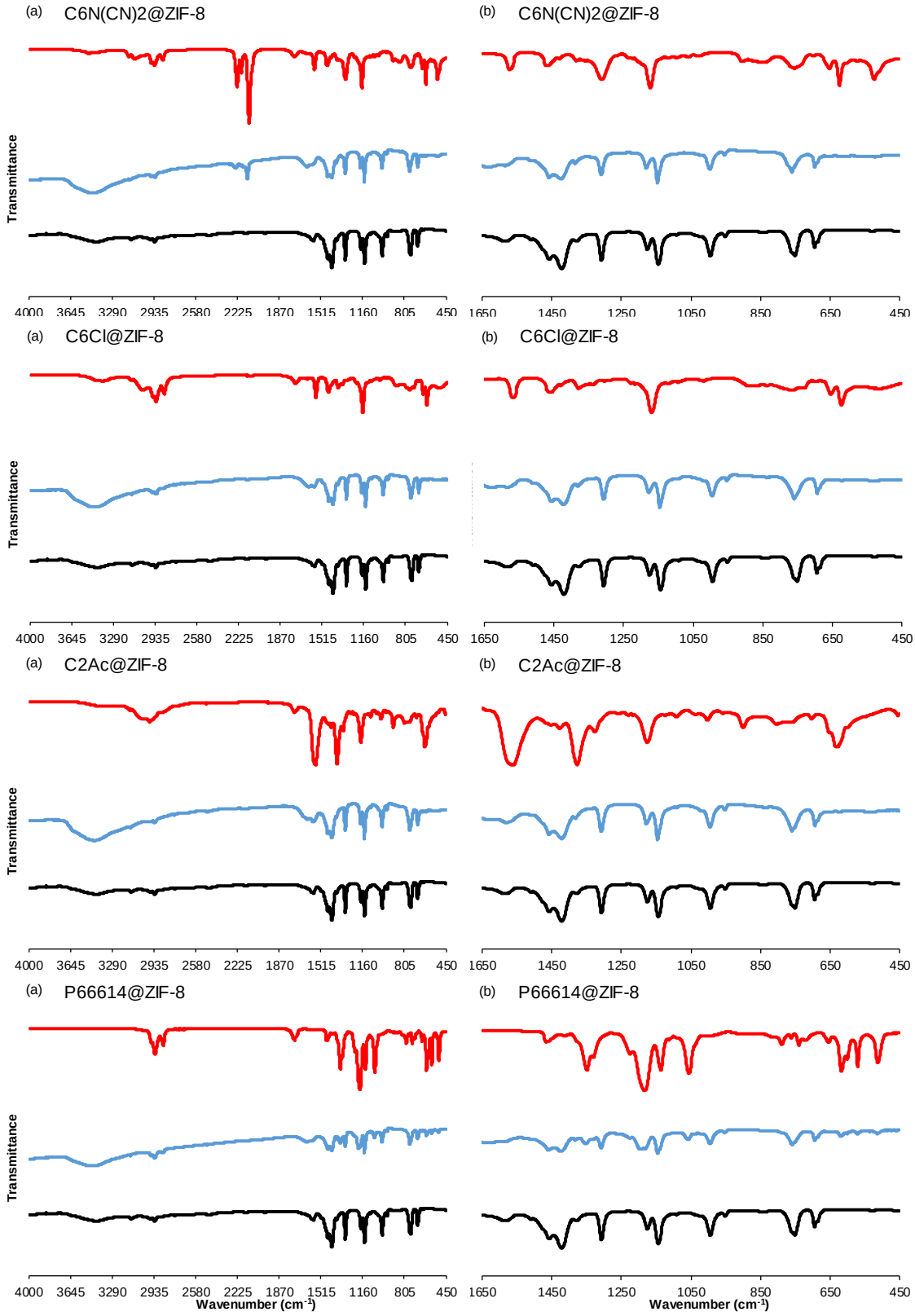

Figure 4.7. Obtained FT-IR spectra of ILs (**red**), IL@ZIF-8 composites (**blue**) and ZIF-8 (**black**), between (a) 4000 and 450 cm^{-1} and (b) 1650 and 450 cm^{-1} (part 2).

FT-IR spectra of composite materials are usually very similar to the ZIF-8. It makes sense since they are largely made of this MOF.

The obtained FT-IR spectra of C2@ZIF-8, C10@ZIF-8, Bz@ZIF-8, C2OH@ZIF-8 and P66614@ZIF-8 show the presence of bands associated with the $[NTf_2]^-$ anion such as the ones visible at around 1350 cm^{-1} (O=S=O asymmetrical stretching), 1225 cm^{-1} (presumed to be C-F_3 stretching), 1060 cm^{-1} (N-S stretching) and below 650 cm^{-1} (N shuttling). C6N(CN)2@ZIF-8 spectrum shows two bands at around 2225 and 2125 cm^{-1} associated to aliphatic C-N stretching and, in this case, to the $[N(CN)_2]^-$ anion. The presence of anion-related bands is indicative of the presence of IL on these composite materials.

The C6B(CN)4@ZIF-8, C6Cl@ZIF-8 and C2Ac@ZIF-8 spectra don't show any kind of IL-related bands. While one could be tempted to think that impregnations with these ILs didn't work, N_2 adsorption-desorption at 77 K data clearly show that all these samples lost specific surface area and total pore volume, when compared to pristine ZIF-8. Furthermore, ILs have negligible volatility, which means that they have to be incorporated either with the use of a solvent or by capillary action.

The sole $[C_6MIM][B(CN)_4]$ spectrum generates additional doubts since the aliphatic C-N stretching band at around 2220 cm^{-1} isn't present. Figure 4.8. shows a comparison between the spectrum of this IL with a poly($[Pyr_{11}][B(CN)_4]$) one [111] and the $[C_2MIM][B(CN)_4]$ one.

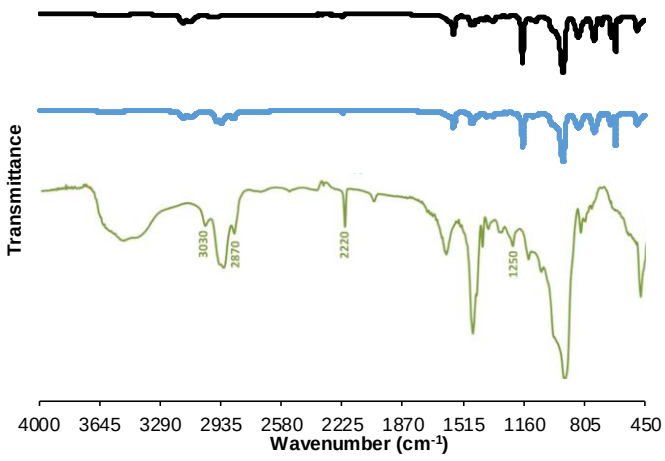

Figure 4.8. FT-IR spectra of $[C_2MIM][B(CN)_4]$ (**black**), $[C_6MIM][B(CN)_4]$ (**blue**) and poly($[Pyr_{11}][B(CN)_4]$) (**green**).

From this comparison, two aspects stand out: the $[C_6MIM][B(CN)_4]$ spectrum doesn't have the same band intensity as the poly($[Pyr_{11}][B(CN)_4]$) and, most importantly, aliphatic C-N stretching band at around 2220 cm^{-1} is barely present. Nevertheless, the $[C_6MIM][B(CN)_4]$ spectrum is very similar to the $[C_nMIM][B(CN)_4]$ one, confirming that the C-N aliphatic band at around 2220 cm^{-1} has weak intensity. Additionally, NMR spectra for ^1H and ^{13}C were asked for $[C_6MIM][B(CN)_4]$ and all expected peaks are present (see Appendix K).

4.1.5. Scanning Electron Microscopy (SEM)

SEM analysis was performed in order to visualize the morphology of selected composites and also to confirm the preservation of the ZIF-8 crystalline structure upon IL impregnation. Figure 4.9. shows some micrographs of ZIF-8 and some IL@ZIF-8 composites. SEM data collected in the open literature confirms the ZIF-8 morphology, even though the amplifications are different [90].

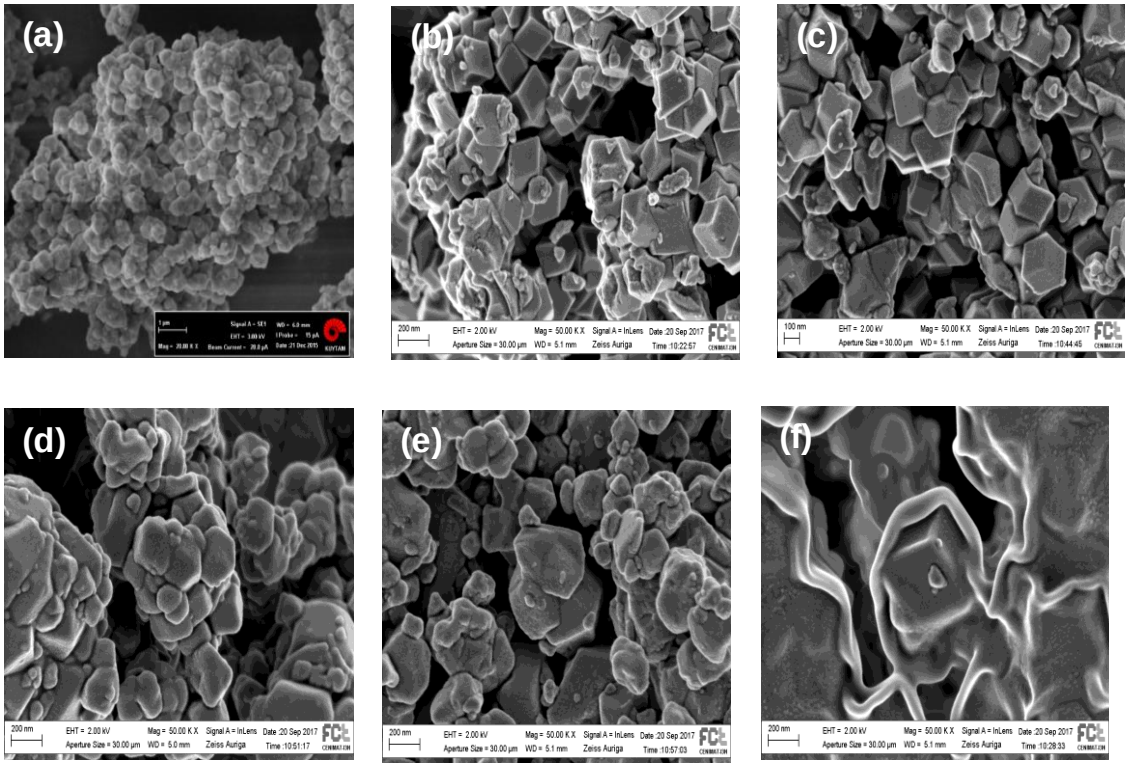

Figure 4.9. Micrographs of (a) ZIF-8 (Kinik et al *[90]*, 20K amplification); (b) ZIF-8 (this work, 50K amplification); (c) C2OH@ZIF-8 (50K amplification); (d) C6B(CN)4@ZIF-8 (50K amplification); (e) C6Cl@ZIF-8 (50K amplification) and (f) P66614@ZIF-8 (50K amplification).

From these micrographs it seems that, depending on their structure, ILs do interact differently with the ZIF-8. As an example, the morphology of P66614@ZIF-8 is different from the C2OH@ZIF-8. Though it is hard to evaluate in some cases, it seems that the crystal structure is mostly preserved during the incorporation of IL into ZIF-8.

Since C6B(CN)4@ZIF-8 characterization results are atypical, it was decided to obtain a micrograph of the material. Its morphology is quite similar to the C6Cl@ZIF-8, meaning both could interact in similar fashion with ZIF-8.

Coupled with the SEM imaging, Energy-Dispersive X-Ray Spectroscopy (EDS) was performed. This technique is usually used for the elemental analysis of a sample; while the elemental composition *per se* wasn't the main purposes, it uncovers which elements are found on the surface of the material. This technology also can map the elements on a micrograph; the brighter

it appears the more the element exists. Due to time restraints, EDS spectra were only obtained for the C6Cl@ZIF-8 and P66614@ZIF-8; they were chosen because of their anion and cation size, respectively. Figures 4.10. and 4.11. show three different magnifications of these two samples, their EDS spectrum and the mapping of some relevant elements.

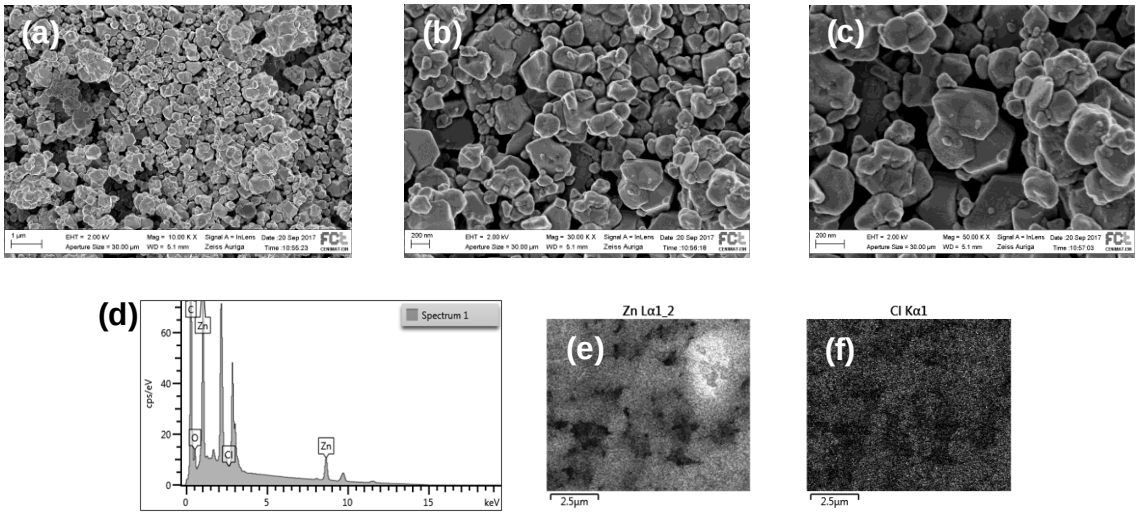

Figure 4.10. SEM and EDS data for C6Cl@ZIF-8. (a) 10K amplification; (b) 30K amplification; (c) 50K amplification; (d) EDS spectrum; (e) Zn mapping; (f) Cl mapping.

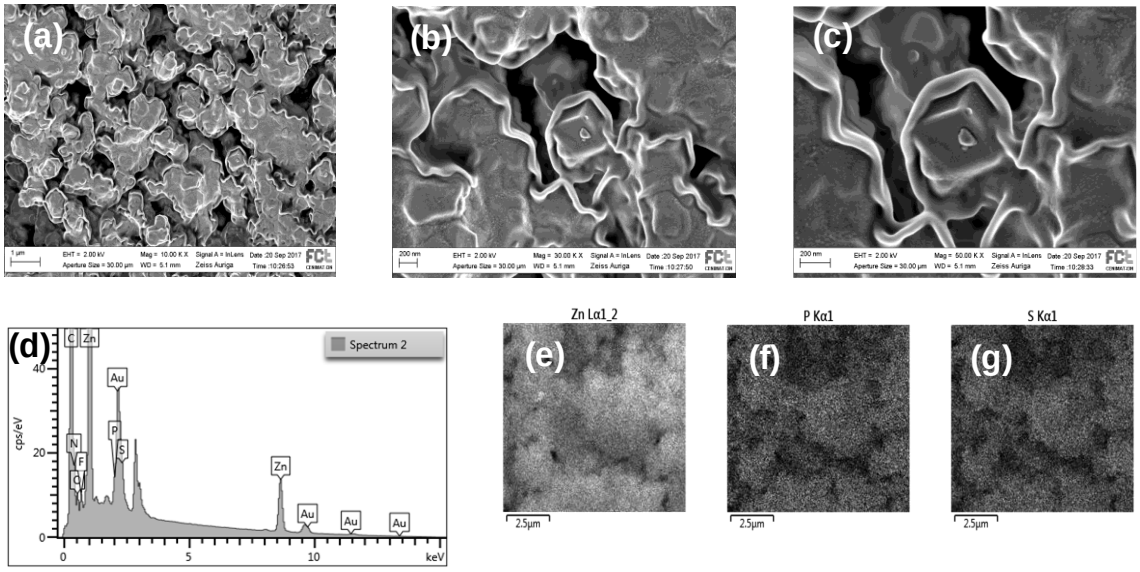

Figure 4.11. SEM and EDS data for P66614@ZIF-8. (a) 10K amplification; (b) 30K amplification; (c) 50K amplification; (d) EDS spectrum; (e) Zn mapping; (f) P mapping; (g) S mapping.

EDS data C6Cl@ZIF-8 shows no presence of Cl at the surface of the material. It could mean that $[Cl]^-$ has entered the composite's pores; this is supported by the element's mapping. As for P66614@ZIF-8, the P peak is mixed with the Au one and, because of that, it can't be accounted. The mappings of P and S elements suggest both are present at the composite's surface, meaning neither the cation nor the anion are fully incorporated within the pores.

4.1.6. Adsorption Equilibria of CO_2 and CH_4

Adsorption equilibria measurements are used to evaluate the performance of an adsorbent for a potential use on a cyclic process like PSA. Pure component CH_4 and CO_2 adsorption equilibrium measurements were performed at 30 °C, since it is an interesting temperature for biogas upgrading, and in a pressure interval from 0 to 16 bar. Due to the amount of samples measured, some experimental runs were firstly executed on the volumetric unit but afterwards the rest were performed on the gravimetric unit. One sample was tested in both units and the results are in complete agreement. Desorption data were always measured to assess the possible existence of hysteresis in these composite materials and also to test their regenerability.

Figure 4.12. presents CH_4 and CO_2 adsorption/desorption isotherms of ZIF-8 obtained by the group [47], showing consistent results with collected data in literature results [115, 116].

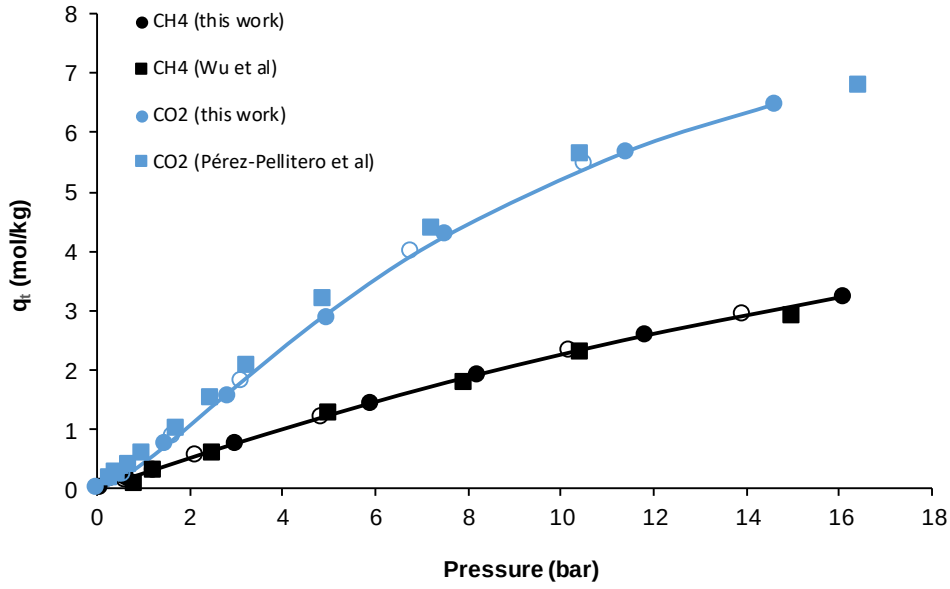

Figure 4.12. CO_2 (**blue**) and CH_4 (**black**) adsorption-desorption isotherms at 30 ºC of ZIF-8. Closed and open symbols denote adsorption and desorption data, respectively. Solid lines represent the fitting with Sips adsorption isotherm model.

Figure 4.13. shows CH_4 and CO_2 adsorption-desorption isotherms for each composite material studied and their comparison with adsorption results of pristine ZIF-8 obtained by the group [47]. Total adsorption (q_t) was the adsorbed amount chosen to present the results since it takes into account the density of the solid matrix as well as the total pore volume. Moreover, this is the usual quantity reported in the open literature. For C6Cl@ZIF-8, as of this writing, there is no available total pore volume value, so 0.4 cm^3/g was assumed in q_t calculations since the majority of the composite samples present total pore volumes similar to this value.

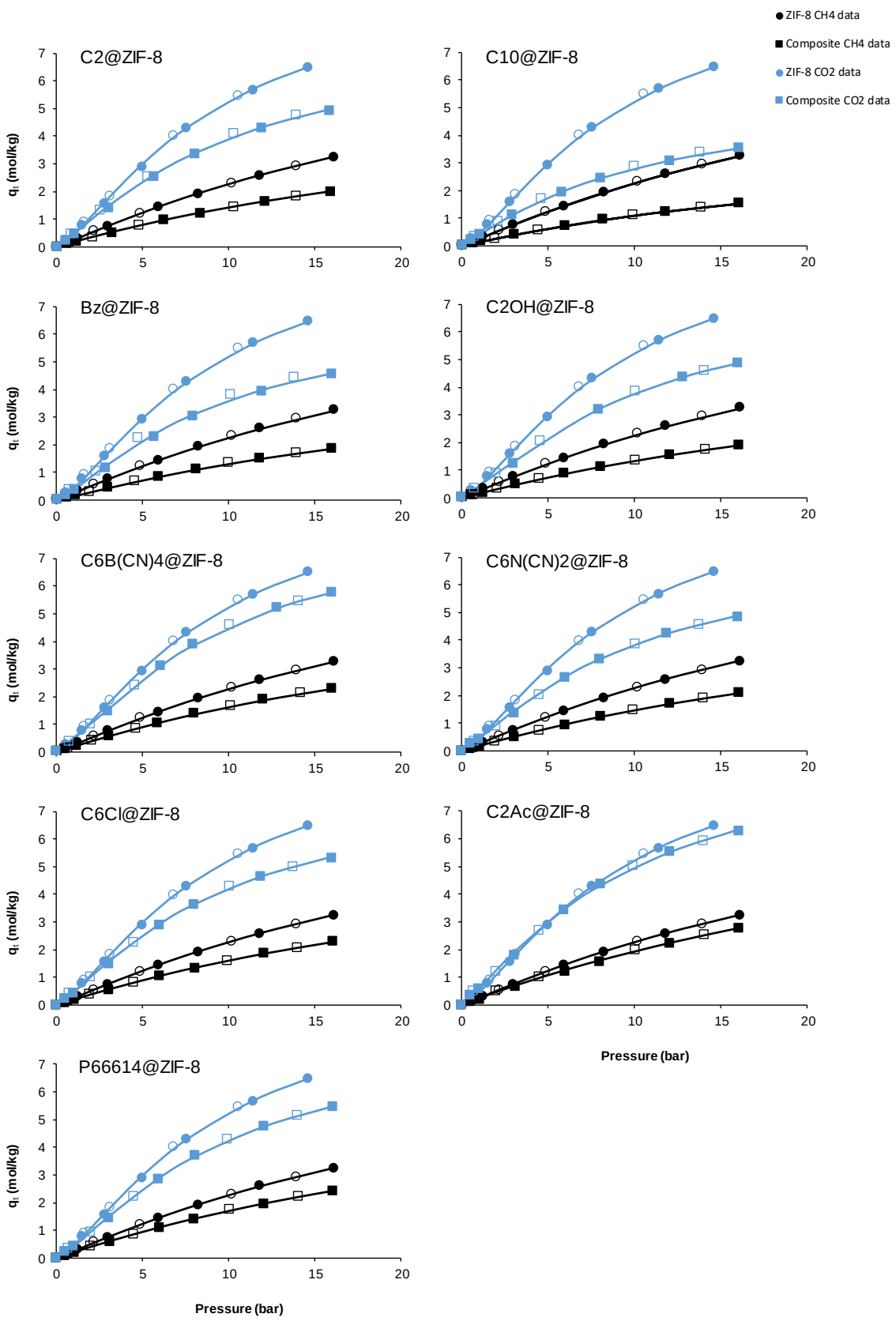

Figure 4.13. CO_2 (**blue**) and CH_4 (**black**) adsorption-desorption isotherms at 30 ºC of ZIF-8 (circle) and IL@ZIF-8 composites (square). Closed and open symbols denote adsorption and desorption data, respectively. Solid lines represent the fitting with Sips adsorption isotherm model.

CO_2 and CH_4 adsorption equilibria data and N_2 adsorption-desorption at 77 K are in accordance. Since all composites present total pore volume drops, these materials were expected to have inferior adsorption capacity, when comparing to pristine ZIF-8. The only exception is the CO_2 adsorption-desorption isotherm of C2Ac@ZIF-8 where, up to 5 bar, the composite presents a superior adsorption capacity. This can be explained by very strong interactions between the anion and the gas [117]. Adsorption-desorption results also confirm that IL is present within the framework of ZIF-8, once again explained by the verified adsorption capacity loss of the composites. All isotherms are Type I, like ZIF-8, according to IUPAC (see Figure 2.14.). No hysteresis was seen in both gases in any composites' isotherms. The higher critical temperature of CO_2 explains higher uptake in all composite materials, when compared to CH_4.

Figure 4.14. shows a comparison of the adsorption capacity of all composite materials for CH_4 and CO_2.

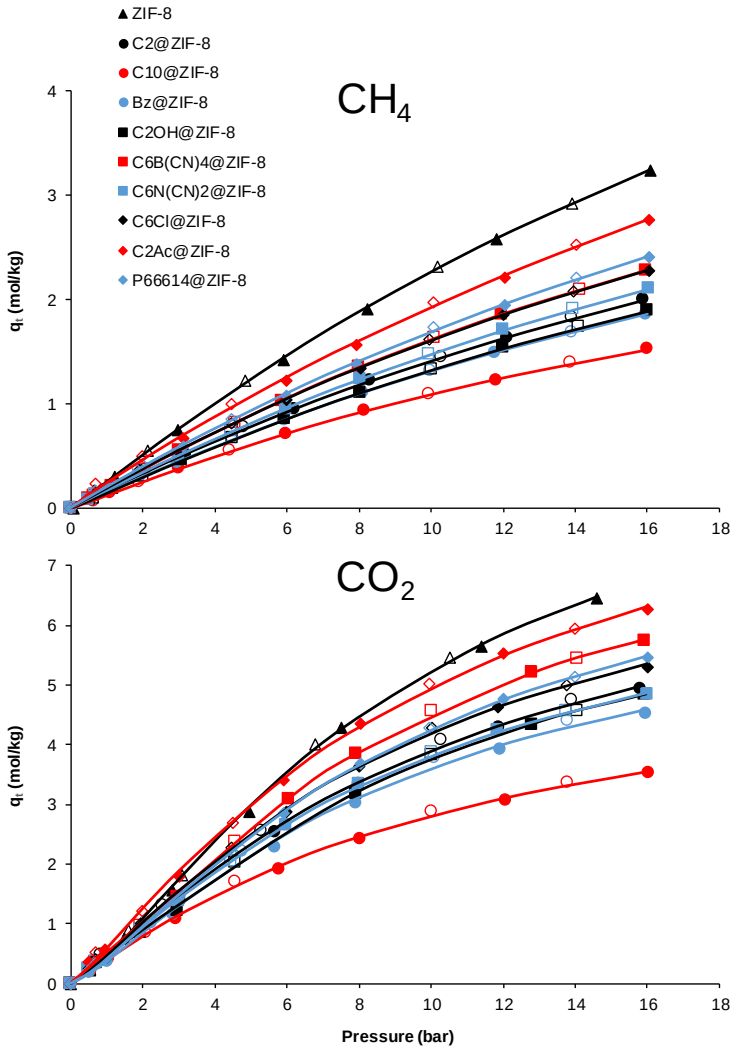

Figure 4.14. CH_4 (top) and CO_2 (bottom) adsorption-desorption isotherms at 30 ºC of ZIF-8 and IL@ZIF-8 composites. Closed and open symbols denote adsorption and desorption data, respectively. Solid lines represent the fitting with Sips adsorption isotherm model.

For all composites, CH_4 adsorption capacity loss is between 15 and 53% at 16 bar. Since no adsorption point at 16 bar exists for ZIF-8, its highest adsorption point was considered for comparison with the composite materials. CO_2 adsorption capacity loss is between 3 and 46%.

For both gases, C2Ac@ZIF-8 is the material that loses the least adsorption capacity. On the contrary, C2OH@ZIF-8, Bz@ZIF-8 and C10@ZIF-8 constitute the top-3 in terms of higher loss in the adsorption capacity.

Comparing the data for C2@ZIF-8, Bz@ZIF-8 and C10@ZIF-8, it seems clear that larger alkyl chains on the imidazolium cation of an IL compromise the most the adsorption capacity of the composite material.

A seemingly surprising result is that large cations can be impregnated in ZIF-8 structure and not compromise the adsorption capacity: P66614@ZIF-8 is in the top-3 of the composites having higher adsorption capacity for both gases.

The presence of an OH group on the C2OH@ZIF-8 very slightly affects the adsorption gas capacity, when comparing to C2@ZIF-8.

The choice of anion seems to be the pivotal aspect when choosing an IL for impregnation into a MOF. The acetate anion $[CH_3CO_2]^-$ seems to be the best choice, possibly confirming that the anion and CO_2 have very strong interactions as has been reported in the literature [117]. For the same cation, the descending order of the best anion to maximize adsorption capacity is $[B(CN)_4]^-$ > $[Cl]^-$ > $[N(CN)_2]^-$. This seems to corroborate the premise that, on nitrile-based ILs, the more –CN groups the anion has, the more CO_2 solubility it presents [118]

Assuming that a linear alkyl chain (C6) on the imidazolium cation should provide approximately the same adsorption capacity revealed by Bz@ZIF-8, $[B(CN)_4]^-$ is a better anion than $[NTf_2]^-$ in terms of adsorption capacity.

CO_2/CH_4 ideal selectivity using the Sips adsorption isotherm model were calculated between 1 and 16 bar. For both gases, the obtained Sips parameters and average relative errors (ARE) for ZIF-8 and each IL@ZIF-8 composite are presented in Table 4.4.

Table 4.4. Sips adsorption isotherm model parameters and average relative error obtained for ZIF-8 and IL@ZIF-8 composites.

Samples	CH_4				CO_2			
	q_s (mol/kg)	*b*	*n*	ARE (%)	q_s (mol/kg)	*b*	*n*	ARE (%)
ZIF-8	9.36	0.034	0.935	1.30	9.95	0.108	0.727	3.06
C2@ZIF-8	6.06	0.031	0.970	1.74	7.96	0.097	0.829	4.02
C10@ZIF-8	3.66	0.046	0.917	2.58	5.76	0.095	0.897	3.21
Bz@ZIF-8	5.25	0.035	0.944	1.13	6.88	0.108	0.781	5.63
C2OH@ZIF-8	5.33	0.036	0.931	1.61	7.47	0.101	0.775	3.83
C6B(CN)4@ZIF-8	6.10	0.039	0.932	1.18	8.41	0.111	0.734	3.58
C6N(CN)2@ZIF-8	6.12	0.034	0.948	2.31	7.56	0.102	0.810	4.55
C6Cl@ZIF-8	6.62	0.034	0.953	2.89	8.15	0.105	0.797	4.95
C2Ac@ZIF-8	10.64	0.022	1.014	3.42	9.95	0.099	0.832	5.10
P66614@ZIF-8	7.72	0.028	0.981	4.24	8.17	0.105	0.759	4.55

The obtained q_s parameters for both gases confirm the above-referred conclusions concerning the adsorption capacity of composites drawn from the experimental data; *n* parameters suggest that all systems (samples) are homogeneous and *b* parameters hint that the same amount of adsorbate molecules are covering the surface for all composites. The observed average relative errors show that Sips adsorption isotherm model is fitting well the experimental points.

Figure 4.15. reveals the obtained ideal CO_2/CH_4 selectivities of ZIF-8 and IL@ZIF-8 materials using the Sips adsorption isotherm model.

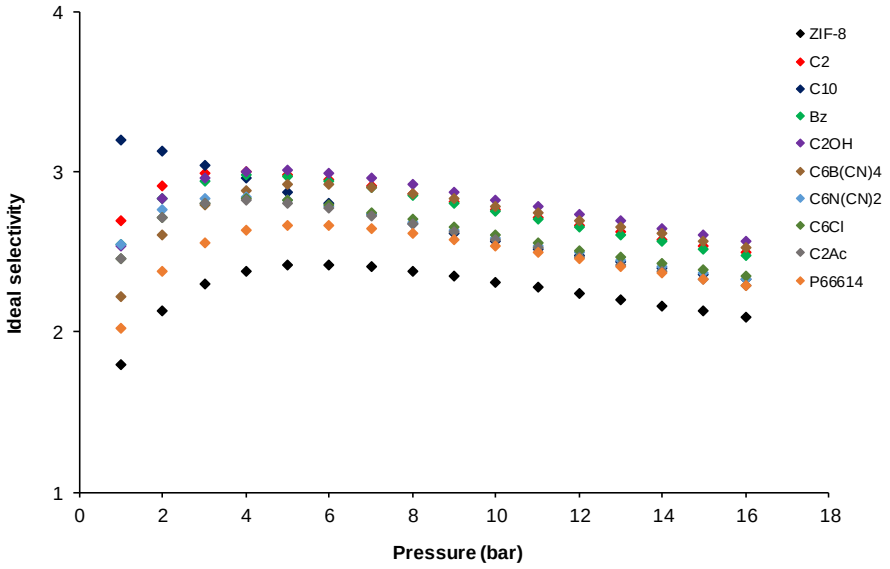

Figure 4.15. Obtained CO_2/CH_4 ideal selectivities for ZIF-8 and IL@ZIF-8 composites using the Sips adsorption isotherm model.

It can be observed that the ZIF-8 tendency is followed by all composites, exception made for C10@ZIF-8. This can be explained by the low adsorption capacity of the composite. Nonetheless, data suggest that this composite could be a potential adsorbent for low pressures (1-3 bar) application. At 1 bar it is nearly 80% more selective than ZIF-8. Nevertheless, there should be a balance between adsorption capacity and selectivity; C10@ZIF-8 presents good ideal CO_2/CH_4 selectivity at lower pressures, but it is the worst composite in terms of gas adsorption capacity.

Between 4 and 16 bar, C2OH@ZIF-8, C2@ZIF-8, Bz@ZIF-8 and C6B(CN)4@ZIF-8 are the most selective composites The first one has, for this pressure range, an average 23% ideal CO_2/CH_4 selectivity gain compared to ZIF-8. The second most selective composite is C6B(CN)4@ZIF-8, just barely outperformed by C2OH@ZIF-8 in this pressure range.

Data suggest that $[P_{66614}]^-$ cation-based ILs should not be considered if the main goal is to greatly improve CO_2/CH_4 selectivity. Imidazolium-based ionic liquids should be preferred and, depending on the desired working pressure range, larger or small alkyl chains should be considered.

As for anions $[Cl]^-$ and $[N(CN)_2]^-$, they should be overlooked with the choice falling over $[NTf_2]^-$ or $[B(CN)_4]^-$ for higher selectivities.

Results show that, generally speaking, the worst composites in terms of adsorption capacity are the most selective, while the ones with higher adsorption capacities have worse selectivities. In summary, considering the CO_2 and CH_4 adsorption capacities and the CO_2/CH_4 ideal selectivities found for each produced composite, the C6B(CN)4@ZIF-8 sample seems to be the best choice of the pair IL-MOF studied herein, namely to impregnate the ionic liquid $[C_6MIM][B(CN)_4]$ into the ZIF-8 material.

4.2. Testing IL's Loading

The previous subchapter presented two significant results: C2OH-impregnated material shows the highest selectivity of all the composites (at high pressures) and the C6B(CN)4-impregnated one has one of the highest adsorption capacity for both CO_2 and CH_4. For these reasons the two ILs were used to prepare new samples, this time with different IL loadings, i.e., composites with different amounts/concentrations of IL. Just like in subchapter 4.1., where an intermediate IL loading was stipulated, the amount of IL added to ZIF-8 was defined by the C2 IL. Higher IL loading (22.5 wt%) and a lower IL loading (7.5 wt%) samples were prepared, following the same protocol (see Appendix B).

Table 4.5. presents the added IL mass for these new composites.

Table 4.5. Desired IL in mass and weight percentage for different IL loadings.

C2 loading = 22.5%				
IL designation	Moles ($x10^{-4}$ mol)	Molar mass (g/mol)	IL mass (g)	Expected loading (%)
C2OH higher loading	7.4	407.31	0.3014	23.2
C6B(CN)4 higher loading	7.4	282.15	0.2088	17.3
C2 loading = 7.5%				
IL designation	Moles ($x10^{-4}$ mol)	Molar mass (g/mol)	IL mass (g)	Expected loading (%)
C2OH lower loading	2.1	407.31	0.0843	7.8
C6B(CN)4 lower loading	2.1	282.15	0.0584	5.5

The main purpose of this subchapter is to uncover the impact of different IL loadings in the adsorption capacity of CO_2 and CH_4, consequently, on the ideal CO_2/CH_4 selectivity. For this, adsorption equilibrium measurements were performed as well as the characterization techniques presented in the previous subchapter.

4.2.1. He Pycnometry

The density of the solid matrix of IL-impregnated ZIF-8 samples was obtained via He pycnometry. The calculations for obtaining the density from raw data are once again made according to the mathematical framework shown in section 3.3.1. The experimental measurements were performed with a gravimetric apparatus already available in the laboratory (see section 3.3.8.).

Table 4.5. presents the experimental solid matrix densities and the pure IL density used for each composite at 60 °C and 1 bar. The He pycnometry was again performed at the temperature of 60 °C. Appendix I has pure IL densities between 5 and 100 °C at 1 bar while Appendix J contains all the collected data related to He pycnometry.

Table 4.6. Experimental solid matrix densities and pure IL densities obtained for samples with different IL loadings.

Sample	ρ_s obtained (g/cm^3)	Pure IL density (g/cm^3)
ZIF-8	1.49	-
C2OH@ZIF-8 higher loading	1.46	1.540
C2OH@ZIF-8	1.48	
C2OH@ZIF-8 lower loading	1.41	
C6B(CN)4@ZIF-8 higher loading	1.35	0.966
C6B(CN)4@ZIF-8	1.29	
C6B(CN)4@ZIF-8 lower loading	1.39	

The solid matrix densities do not differ, within experimental error, from the original composite solid density. In a nutshell, the obtained density is almost loading-independent.

4.2.2. N_2 Adsorption-Desorption Isotherms at 77 K

In order to determine the specific surface area of the composite samples, N_2 adsorption-desorption equilibrium measurements at 77 K were performed and analysed. The set of obtained isotherms can be seen in Figure 4.16.

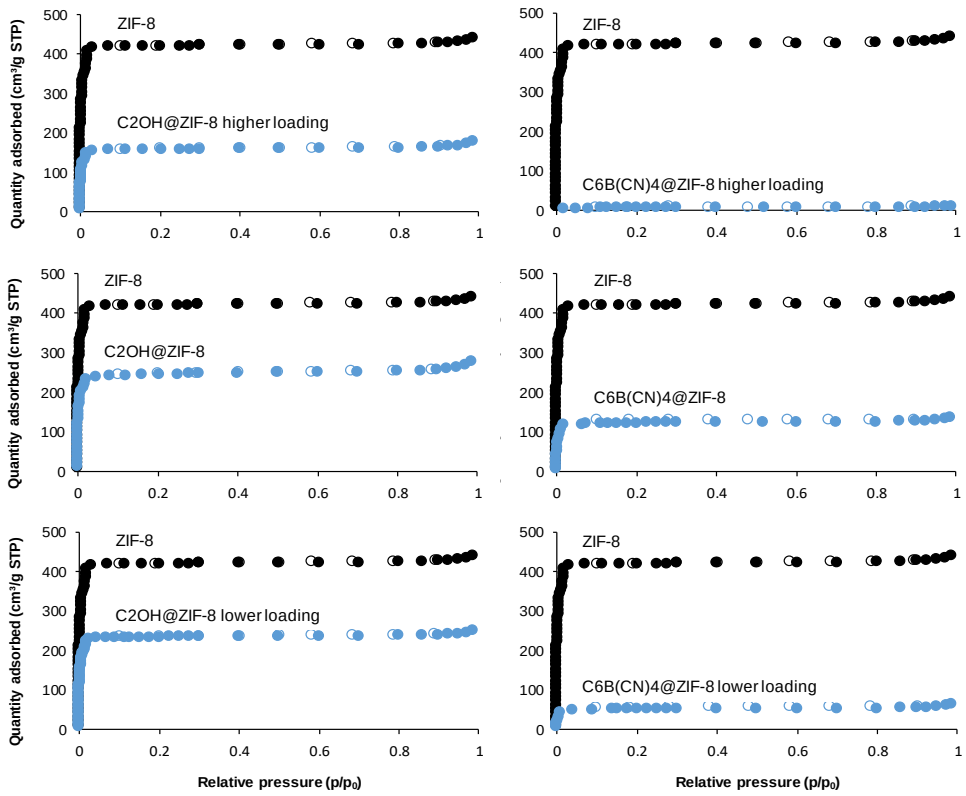

Figure 4.16. N_2 adsorption-desorption isotherms at 77 K of ZIF-8 and manufactured IL@ZIF-8 composites. Closed and open symbols denote adsorption and desorption data, respectively.

C2OH@ZIF-8 samples' isotherms are all Type I, typical of microporous materials, according to IUPAC classification. C6B(CN)4@ZIF-8 with lower and intermediate loadings also present Type I isotherms, while the higher loading result indicates that the material is nonporous.

Table 4.7. shows the obtained BET and Langmuir specific surface areas in addition to the total pore volume.

Table 4.7. BET specific surface area and respective *c* constant, Langmuir specific surface area, total pore volume and respective partial pressure obtained for samples with different IL loadings using the *MicroActive* software.

Sample	BET specific surface area (m^2/g)	*c*	Langmuir specific surface area (m^2/g)	Total pore volume (cm^3/g)	P/P_0
ZIF-8	1907±81	407	2008±83	0.67	0.97
C2OH@ZIF-8 higher loading	706±24	409	736±26	0.26	0.97
C2OH@ZIF-8	1031±20	574	1096±19	0.41	0.97
C2OH@ZIF-8 lower loading	1087±62	340	1141±65	0.38	0.97
C6B(CN)4@ZIF-8 higher loading	16±0	560	21±0	0.01	0.97
C6B(CN)4@ZIF-8	552±33	402	566±36	0.20	0.97
C6B(CN)4@ZIF-8 lower loading	215±10	398	223±0	0.09	0.97

Due to IL partial pore occupancy, all composites BET and Langmuir specific surface areas drop when compared to ZIF-8. Logic dictates that the higher the loading, the less specific surface area the material possesses. This is verified in the C2OH@ZIF-8 samples, though it was expected larger values for the lower loading sample given the obtained results for the intermediate loading sample. For C6B(CN)4 samples, the expected logic isn't confirmed. Also, they exhibit much lower specific areas than their C2OH@ZIF-8 counterparts, to the point where the higher loading sample can be considered a nonporous material. The distinct results for the C6B(CN)4@ZIF-8 composites can be related with experimental difficulties when dealing with these samples.

Total pore volume follows the same reasoning of specific surface area: the higher the loading, the less total pore volume the sample has. The two sets of IL-impregnated samples don't follow this reasoning. C2OH@ZIF-8 intermediate and lower loadings samples have, in essence, the same pore volume. C6B(CN)4@ZIF-8 samples again exhibit lower total pore volume than their C2OH@ZIF-8 counterparts, with both higher and lower samples showing little pore volume.

Additionally, non-linear density functional theory (NLDFT) analysis was performed with the resulting data of N_2 adsorption/desorption at 77 K, providing the pore size distribution for each composite sample, as shown in Figure 4.17. C6B(CN)4@ZIF-8 higher and lower loadings samples showed no kind of pore distribution, so only C2OH@ZIF-8 NLDFT data is presented.

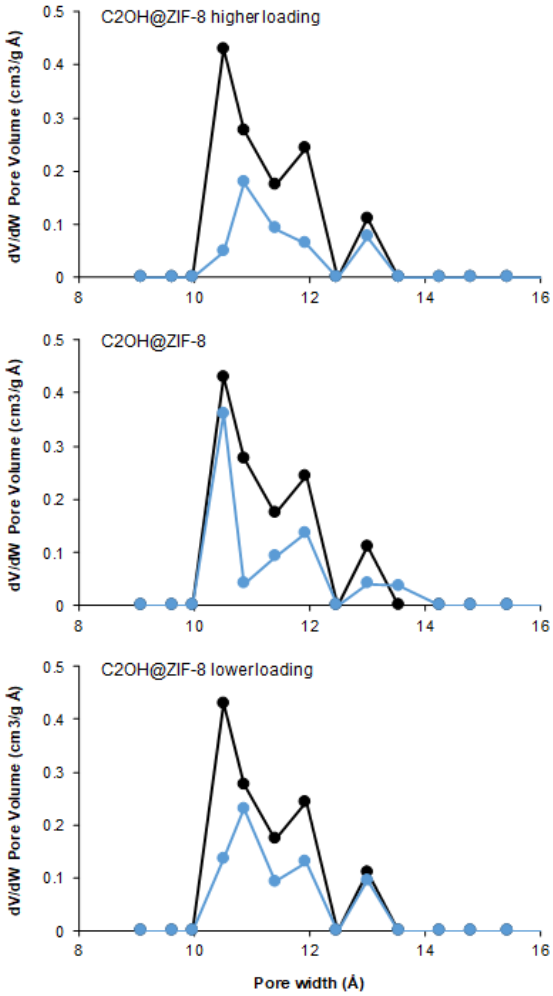

Figure 4.17. Pore size distribution through NLDFT analysis of ZIF-8 and C2OH@ZIF-8 composites.

This analysis shows that all C2OH@ZIF-8 samples have a similar pore distribution to ZIF-8 same, with a decrease on the available pores due to IL partial occupancy; it also confirms that these composites are all microporous materials, according to IUPAC definition [73].

4.2.3. Powder X-Ray Diffraction (PXRD)

This characterization technique can be used for several purposes, but the one of interest in this case is to assess if different (especially, higher) IL loadings can affect the structure within the framework of ZIF-8 upon IL incorporation. This can be verified by comparing the characteristic peaks of ZIF-8 with the ones obtained for each composite material, as depicted in Figure 4.18.

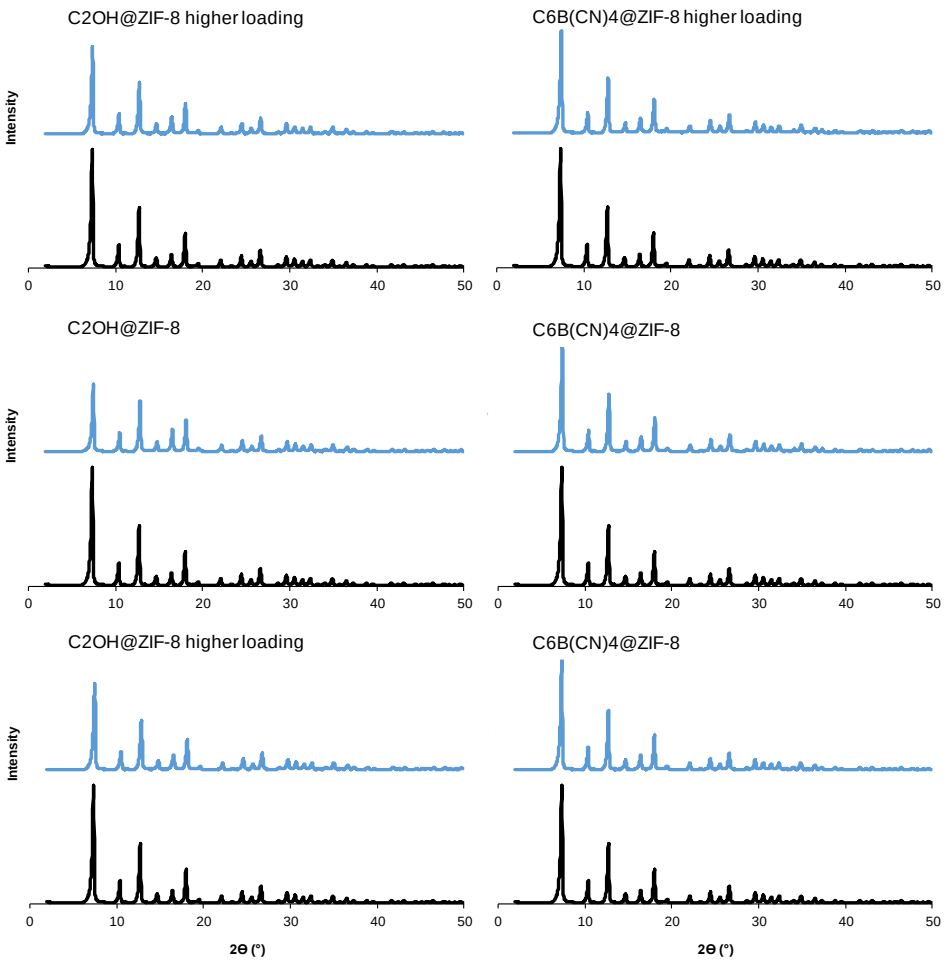

Figure 4.18. PXRD spectra for all C2OH@ZIF-8 and C6B(CN)4@ZIF-8 samples.

PXRD results for both set of samples indicate that IL loading does not affect the structure of the ZIF-8 framework upon IL impregnation (considering the loading percentages in this work) since no significant changes in peaks' intensity can be found, i.e., PXRD spectra of all C2OH@ZIF-8 samples are essentially the same; this is also verified in all C6B(CN)4@ZIF-8 samples. Since composites' spectra don't differ much from the ZIF-8 one, all these materials are crystalline.

It is possible, however, that high IL loading could change the ZIF-8 structure. But at that point, probably there is no advantage in designing such a material in terms of adsorption capacity. More IL would reduce the total pore volume and eventually the manufactured material would be a nonporous one.

4.2.4. Fourier Transform Infrared Spectroscopy (FT-IR)

There is a purpose in obtaining FT-IR spectra for both sets of composite materials. It expected that C2OH@ZIF-8 samples exhibit anion-related bands; C6B(CN)4ZIF-8 samples with higher and lower loadings are expected to have the similar spectra when compared to the intermediate loading sample. Figure 4.19. shows the obtained spectra.

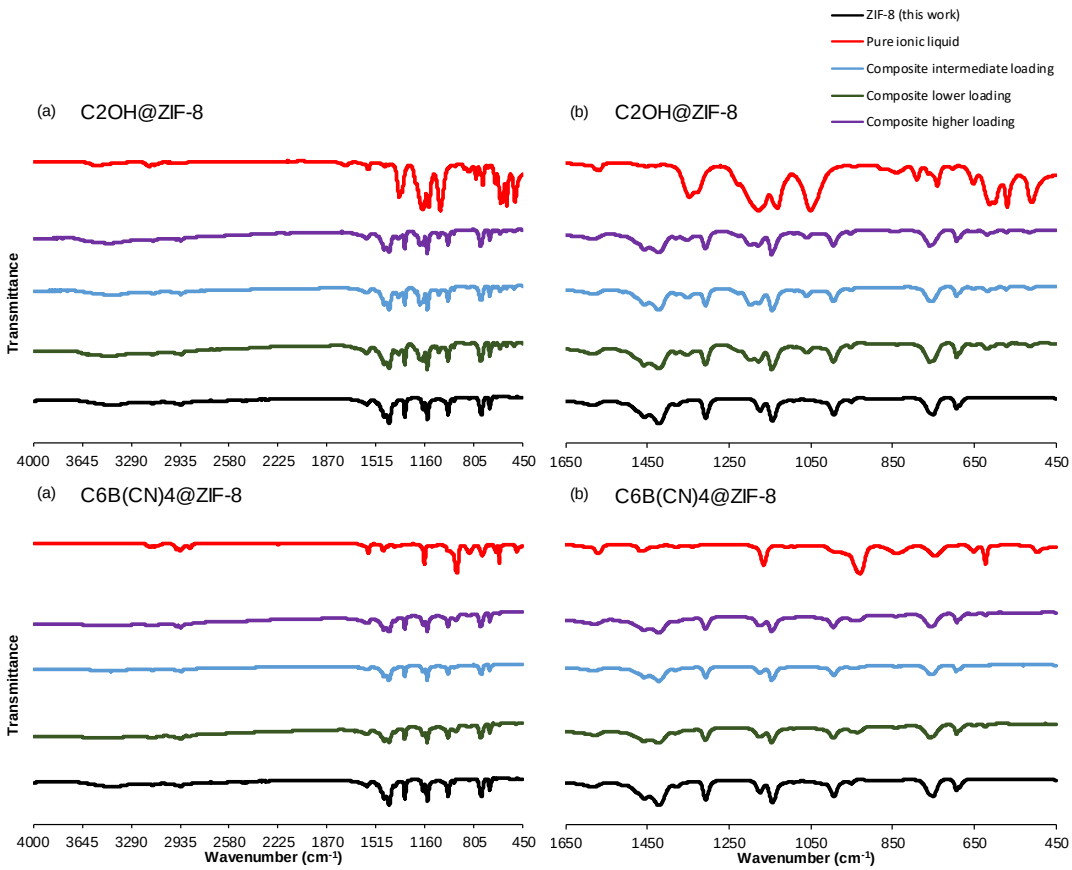

Figure 4.19. Obtained FT-IR spectra of both ILs (**red**), IL@ZIF-8 composites tested for IL loading effect (**purple**, **blue** and **dark green** for higher, intermediate and lower IL loading, respectively) and ZIF-8 (**black**), between (a) 4000 and 450 cm-1 and (b) 1650 and 450 cm^{-1}.

All C2OH@ZIF-8 spectra show the presence of bands associated with the $[NTf_2]^-$ anion such as the ones visible at around 1350 cm^{-1} (O=S=O asymmetrical stretching), 1225 cm^{-1} (presumed to be C-F_3 stretching), 1060 cm^{-1} (N-S stretching) and below 650 cm^{-1} (N shuttling). This confirms the presence of the IL within the framework of ZIF-8. As for the C6B(CN)4@ZIF-8 spectra, there are no bands at around 2225 and 2125 cm^{-1} (aliphatic C-N stretching), confirming a string of anomalous results associated to the impregnated IL. Nevertheless, N_2 adsorption-desorption isotherms at 77 K data indicate that there is impregnated IL, so much that the samples present the lowest of total pore volume (and specific surface area) of all the composites developed for this work. These spectra can't be quantitatively compared. For that to happen, the same amount of KBr and sample had to be used when producing the FT-IR tablet.

4.2.5. Scanning Electron Microscopy (SEM)

SEM analysis were performed to confirm PXRD data that a higher IL loading doesn't change too much the crystalline structure during the incorporation of IL into ZIF-8. The only sample analysed was C2OH@ZIF-8 with a higher loading since lower loadings would present micrographs similar to ZIF-8 and because C6B(CN)4 characterization results are transversally anomalous. Figure 4.20. presents SEM imaging for both C2OH@ZIF-8 intermediate and higher loadings.

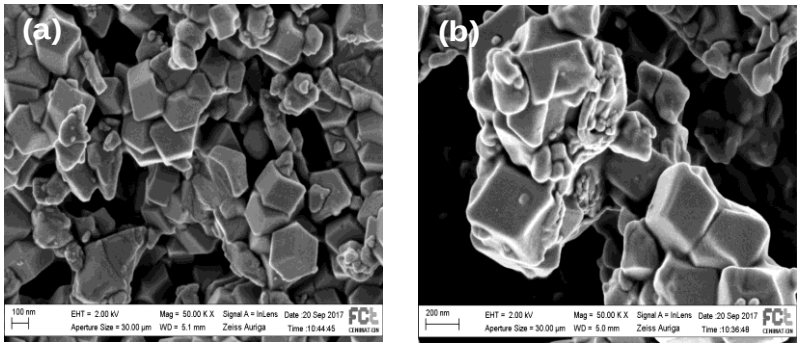

Figure 4.20. SEM micrographs of C2OH@ZIF-8 (a) intermediate loading and (b) higher loading (both at 50K amplification).

The morphologies of both materials are quite similar. The crystalline structure of both materials seems to be preserved after IL impregnation into ZIF-8. So, only higher IL loadings could potentially change the structure of the framework of ZIF-8.

4.2.6. Adsorption Equilibria of CO_2 and CH_4

Adsorption equilibria measurements were performed to study the effect of IL loading on adsorption and ideal CO2/CH_4 selectivity. Pure component CH_4 and CO_2 adsorption equilibrium measurements were all performed at 30 °C. The pressure interval was different for both sets of composites. All experimental runs were executed on the gravimetric unit. Desorption data were always measured to assess the possible existence of hysteresis in these composite materials and also test their regenerability.

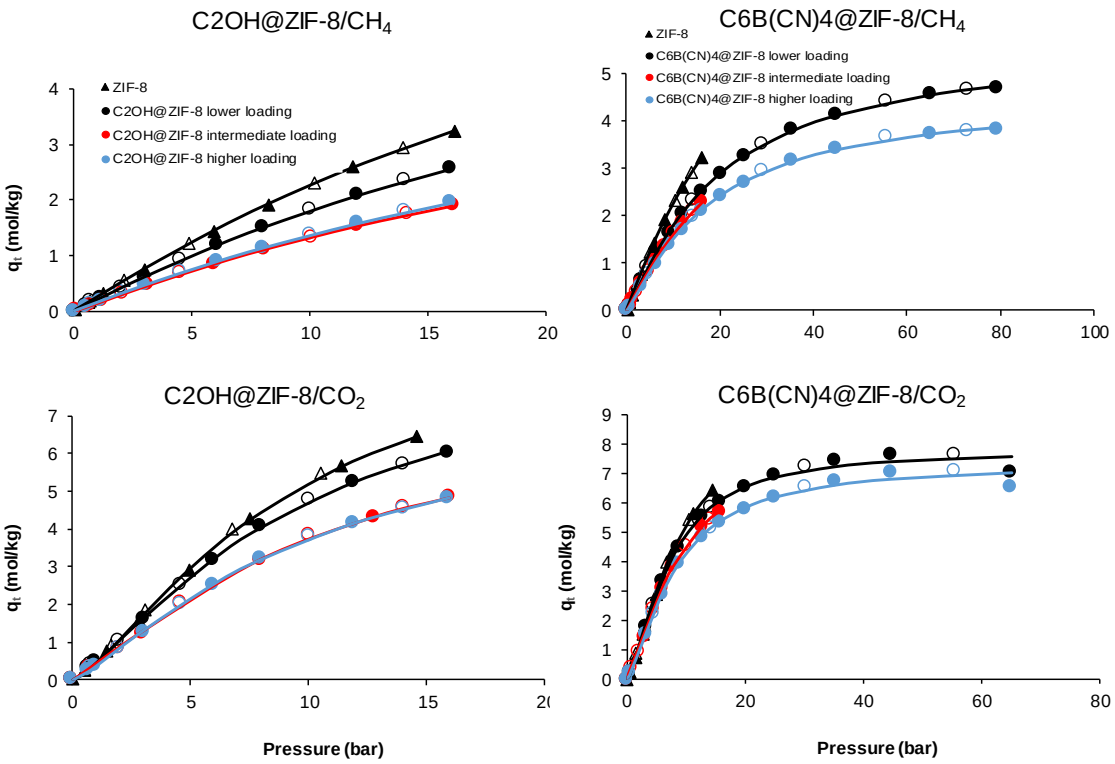

Figure 4.21. CO_2 and CH_4 adsorption/desorption isotherms at 30 ºC of C2OH@ZIF-8 and C6B(CN)4@ZIF-8 samples. Closed and open symbols denote adsorption and desorption data, respectively. Solid lines represent the fitting with Sips adsorption isotherm model.

Adsorption-desorption data obtained, shown in Figure 4.21. are coherent with N_2 adsorption-desorption isotherms at 77 K data. Comparing with ZIF-8, all composites present adsorption capacity loss related to total pore volume decrease.

The premise that higher IL loadings lead to larger adsorption capacity losses in not verified on the C2OH@ZIF-8 samples. The intermediate and higher IL loading samples present the same adsorbed amount of gas. However, C6B(CN)4@ZIF-8 samples do follow that premise, even though the lower and higher loading samples, for CO_2, are not well fitted by the Sips adsorption isotherm model. Total adsorption is supposed to keep increasing until a plateau is reached; this is not verified. This can be explained by the very low total pore volume of these two samples.

Ideal CO_2/CH_4 selectivities using the Sips adsorption isotherm model were calculated between 1 and 16 bar. For both gases, the obtained Sips parameters and average relative error (ARE) for ZIF-8 and each composite are presented in Table 4.8.

Table 4.8. Sips adsorption isotherm model parameters and average relative error obtained for ZIF-8 and IL@ZIF-8 composites.

	CH_4				CO_2			
Samples	q_s (mol/kg)	*b*	*n*	ARE (%)	q_s (mol/kg)	*b*	*n*	ARE (%)
ZIF-8	9.36	0.034	0.935	1.30	9.95	0.108	0.727	3.06
C2OH@ZIF-8 lower loading	7.64	0.033	0.958	1.71	9.24	0.103	0.766	3.56
C2OH@ZIF-8 intermediate loading	5.33	0.036	0.931	1.61	7.47	0.101	0.775	3.83
C2OH@ZIF-8 higher loading	6.30	0.029	0.971	1.63	7.55	0.098	0.785	3.25
C6B(CN)4@ZIF-8 lower loading	5.67	0.052	0.862	2.13	7.83	0.139	0.623	5.42
C6B(CN)4@ZIF-8 intermediate loading	6.10	0.039	0.932	1.18	8.41	0.111	0.734	3.58
C6B(CN)4@ZIF-8 higher loading	4.51	0.057	0.837	2.23	7.36	0.124	0.675	4.44

In C6B(CN)4@ZIF-8 samples, the expected sample with largest adsorption capacity is the one with intermediate IL loading while in reality the sample with lower IL loading shows the best gas adsorption capacity. The *n* parameters suggest that all systems (samples) are homogeneous and *b* parameters hints that the same amount of adsorbate molecules are covering the surface for all composites. The observed average relative error shows that Sips adsorption isotherm model is fitting well the experimental points. Figure 4.22. reveals the obtained ideal CO_2/CH_4 ideal selectivities of ZIF-8 and IL@ZIF-8 materials using the Sips adsorption isotherm model.

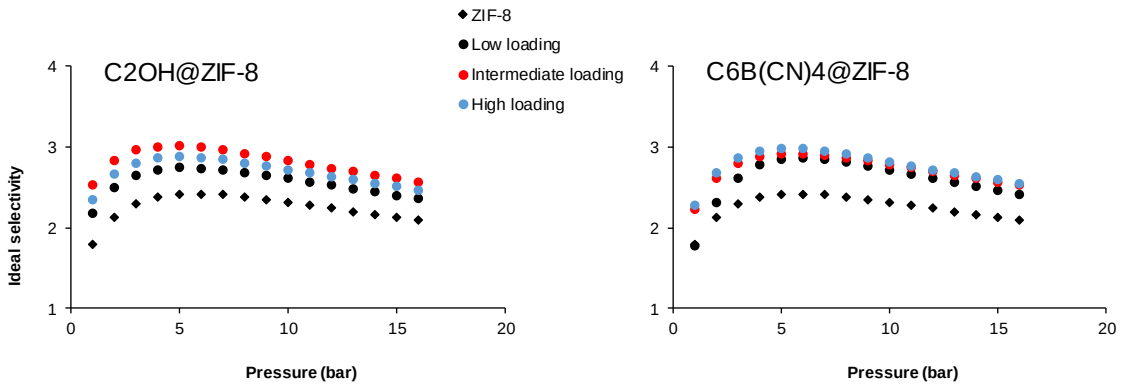

Figure 4.22. Obtained ideal CO_2/CH_4 selectivities for ZIF-8 and IL@ZIF-8 composites using the Sips adsorption isotherm model.

CO_2/CH_4 ideal selectivities results in both set of samples are inconsistent. While a higher IL loading helps on improving selectivity in C6B(CN)4@ZIF-8 samples, this is not verified in the C2OH@ZIF-8 samples.

5. Conclusions and Future Work

5.1. Conclusions

The focal point of the thesis is the determination of what happens to a MOF, namely the ZIF-8 one, upon IL impregnation. Since a plethora of ILs exists, 9 were chosen in order to understand the cation, anion and IL loading effects on CH_4 and CO_2 adsorption capacities, as well as on their ideal CO_2/CH_4 selectivities.

In order to assess the cation and anion effects, nine distinct ILs were impregnated into ZIF-8 with the same IL molar loading. After the manufacture of the composite materials, they were texturally characterized and had their adsorption capacity for CO_2 and CH_4 measured.

He picnometry results show a variety of solid matrix densities. The changes on the solid matrix density are not fully related with the IL in the composites, indicating that there should be some specific IL-ZIF-8 interactions responsible for observed values.

N_2 adsorption-desorption at 77 K reveals that composite samples have Type I isotherms (according to IUPAC) and, along with NLDFT analysis, shows that all manufactured composites maintain the ZIF-8 microporous nature. The obtained results also reveal that the incorporation of IL into the ZIF-8 framework decreases the specific surface area by 20-50% and total pore volume by 30-40% of the obtained material, by comparison to pristine ZIF-8.

Composites' PXRD spectrum show some changes in the intensity of two specific characteristic peaks, by comparison to pristine ZIF-8. This seems to indicate a change in the electron density of ZIF-8 upon IL impregnation. PXRD data, again by ZIF-8 comparison, show no significant changes and thus all composite materials are crystalline.

FT-IR spectra of most composite materials present IL-related bands, confirming that the impregnation was successful. While data acquired for C6B(CN)4@ZIF-8 samples, C6Cl@ZIF-8 and C2Ac@ZIF-8 can cause some doubts regarding the success of respective IL impregnation, since no IL-related bands appear in the composite's spectrum, N_2 adsorption-desorption at 77 K results clearly show the presence of IL within the ZIF-8 structure.

SEM analysis show that the selected composites present different morphologies. This further confirms the presence of IL within ZIF-8 and indicates that ILs can interact differently with ZIF-8, depending on their structure.

CH_4 and CO_2 adsorption equilibria measurements were performed at 30 °C, mostly in a pressure interval from 0 to 16 bar. Desorption data revealed no presence of hysteresis in any composite; these material revealed to be regenerable.

It was found that, for adsorption capacity, the C2Ac@ZIF-8 was the best of all composites for both gases. Other illations taken from these results are that larger alkyl chains in the imidazolium cation are more harmful than shorter ones (for gas adsorption); a big cation does not necessarily compromise the adsorption capacity; the presence of a OH group has a very slight negative effect on the adsorption capacity (as seen from the C2@ZIF-8 and C2OH@ZIF-8 adsorbed amounts of both gases) and that the anion plays a more important role than the cation. As an example, at 16 bar, total adsorbed amount of CO_2 is 5.7, 5.3 and 4.8 mol/kg for C6B(CN)4@ZIF-8, C6Cl@ZIF-8 and C6n(CN)2@ZIF-8 composites, respectively

Results suggest that the best anions are $[CH_3CO_2]^-$ > $[B(CN)_4]^-$ > $[Cl]^-$ > $[N(CN)_2]^-$. Assuming that a possible C6@ZIF-8 offers approximately the same adsorption capacity revealed by Bz@ZIF-8, $[B(CN)_4]^-$ is better than $[NTf_2]^-$ in terms of adsorption capacity.

The Sips adsorption isotherm equation was used to fit the experimental CH_4 and CO_2 data obtained. These results seem to fit well the experimental points, with parameters suggesting samples are homogeneous and that, for each gas, the same amount of adsorbate molecules existed on the surface of all composite. Ideal CO_2/CH_4 selectivities were then obtained from these predicted total adsorbed amounts. All composite materials had higher ideal CO_2/CH_4 selectivities than ZIF-8 and followed its tendency, with the exception of C10@ZIF-8, that presents 3.2 selectivity at 1 bar. Results show that composites with lower adsorption capacity proved to be the most selective like C2OH@ZIF-8 (the most selective at high pressures) along with the C6B(CN)4@ZIF-8. The latter showed good ideal CO_2/CH_4 selectivity along with good adsorption capacity, especially for CO_2. Given all adsorption equilibria data collected, it seems to balance well adsorption capacity with ideal CO_2/CH_4 selectivity, being considered as the best choice for impregnation despite the composite presenting a string of anomalous textural characterization results like the N_2 adsorption-desorption at 77 K data as well as the FT-IR spectrum.

Samples for the study of IL loading were produced with the C2OH and C6B(CN)4 ILs. Adding to their original (intermediate loading) sample, lower and higher IL loading samples were prepared. The same textural characterization was made for both sets of samples. IL loading did not have a significant effect on He pycnometry, PXRD, FT-IR and SEM results.

N_2 adsorption-desorption at 77 K revealed that C2OH@ZIF-8 new samples are microporous. C6B(CN)4@ZIF-8 with higher IL loading does not present a Type I isotherm (according to IUPAC) and results are indicative of a nonporous material. This sample, alongside with C6B(CN)4@ZIF-8 with lower IL loading, does not present pore size distribution.

Adsorption equilibria data for the composites with distinct loading values is inconclusive. The premise that higher IL loadings leads to greater adsorption capacity loss is only verified in C6B(CN)4@ZIF-8 samples. The Sips adsorption isotherm equation seems to fit well the experimental points for both sets, exception made for the CO_2 fitting of the new C6B(CN)4@ZIF-8 samples. Obtained parameters suggest samples are homogeneous and that, for each gas, the same amount of adsorbate molecules existed on the surface of all composite. Ideal CO_2/CH_4

selectivities were then obtained from these calculated total adsorbed amounts. All new composite materials had higher ideal selectivities than ZIF-8 and followed its tendency. The premise that higher IL loadings improve ideal CO_2/CH_4 selectivities is only observed once again in C6B(CN)4@ZIF-8 samples.

This work proves the possibility of using ILs to enhance the selectivity for CO_2/CH_4 separations using MOFs. The structural features of the IL used to prepare the composite clearly affect its performance. A better understanding of the interactions between the IL and the MOF that explain the experimental results is still needed, but the door is now open to exploit these composite materials in other separations. Moreover, tuning the used MOF can also create interesting new materials for gas separation.

5.2. Future Work

The biggest expectation for this thesis is that it helps laying some groundwork in the IL@MOF materials research for adsorption purposes. Since only a handful of related articles were published and hundreds of ILs and MOFs exist, several aspects can be studied:

1. Understand how the total pore volume difference between the pristine MOF and the composite material can be used to determine the actual IL loading or develop a method (possibly through absorbance measurements) for that;
2. Study with more detail the IL loading effect;
3. N_2 adsorption equilibrium measurements for studying potential application of these materials for CO_2/N_2 separations in flue gas streams;
4. Test the impact of new cations and especially anions (such as $[methide]^-$ or $[FAP]^-$) on the adsorption capacity and ideal CO_2/CH_4 and CO_2/N_2 selectivities. In particular, study the impact of fluorinated cations or the addition of an alkyl group to the C2 atom of the imidazolium cation;
5. Experiment IL impregnation on new MOFs with higher adsorption capacity and potential than ZIF-8;
6. Mixed impregnation with IL and amines and its impact on adsorption capacity and selectivity;
7. Prepare and optimize the manufacture of samples using the 'ship-in-a-bottle' technique;
8. Test the influence of the chosen solvent for IL impregnation, since it can attack the MOF structure and compromise the adsorption capacity and, possibly, ideal selectivity;
9. Perform TEM imaging as it can provide details about the internal composition of the composite, possibly enabling to understand the disposition of the IL inside the pore;
10. Further study the $[C_6MIM][B(CN)_4]$ IL in an attempt to understand the anomalous characterization results collected for respective composites.

6. References

[1] R. Monastersky (2013). Global carbon levels near worrisome milestone. *Nature,* vol. 497, pp. 13-14.

[2] Carbon Dioxide Information Analysis Center. Recent Greenhouse Gas Concentrations. Available online: http://cdiac.ornl.gov/pns/current_ghg.html. [Accessed 19th May 2017].

[3] National Oceanic & Atmospheric Administration. Trends in Atmospheric Carbon Dioxide. Available online: https://www.esrl.noaa.gov/gmd/ccgg/trends/. [Accessed 19th May 2017].

[4] H. Rodhe (1990). A Comparison of the Contribution of Various Gases to the Greenhouse Effect. *Science,* vol. 248, pp. 1217-1219.

[5] National Aeronautics and Space Administration. Greenhouse Gases: Refining the Role of Carbon Dioxide. March 1998. Available online: https://www.giss.nasa.gov/research/briefs/ma_01/. [Accessed 19th May 2017].

[6] R. Kirk and D. Othmer (1995). *Encyclopedia of Chemical Technology*. Volume 5. Wiley.

[7] International Panel on Climate Change (2007). *Climate Change 2007 - Synthesis Report*. IPCC.

[8] S. Rackley (2010). *Carbon Capture and Storage*. Elsevier.

[9] Renewable Energy Policy Network for the 21st Century (2016). *Renewables 2016 - Global Status Report*.

[10] Intergovernmental Panel on Climate Change (2005). *Carbon Dioxide Captrue and Storage*. Cambridge University Press.

[11] PBL Netherlands Environmental Assessment Agency (2016). *Trends in Global CO_2 Emissions - 2016 Report*. PBL and EC-JRC.

[12] NASA. NASA, NOAA Data Show 2016 Warmest Year on Record Globally. Available online: https://www.nasa.gov/press-release/nasa-noaa-data-show-2016-warmest-year-on-record-globally. [Accessed 24th May 2017].

[13] University of East Anglia. Low growth in carbon emissions continues for third year. Available online: https://www.uea.ac.uk/about/-/low-growth-in-global-carbon-emissions-continues-for-third-successive-year. [Accessed 24th May 2017].

[14] Human Development Reports. Human Development Index and its components. Available online: http://hdr.undp.org/en/composite/HDI. [Accessed 24th May 2017].

[15] International Union of Geodesy and Geophysics. List of developing countries. Available online: http://www.iugg2015prague.com/list-of-developing-countries.htm. [Accessed 24th May 2017].

[16] World Bank. Countries and Economies. Available online: https://data.worldbank.org/country/. [Accessed 20th March 2017].

[17] Intergovernmental Panel on Climate Change (2014). *Climate Change 2014 - Mitigation of Climate Change*. Cambridge University Press.

[18] V. Smil (2008). *Global Catastrophes and Trends: The Next 50 Years*. The MIT Press.

[19] National Research Council (2010). *Advancing the Science of Climate Change*. The National Academies Press.

[20] United Nations Framework Convention on Climate Change. First steps to a safer future: Introducing The United Nations Framework Convention on Climate Change. Available online: http://unfccc.int/essential_background/convention/items/6036.php. [Accessed 24th May 2017].

[21] United Nations Framework Convention on Climate Change. United Nations Framework Convention on Climate Change. Available online: https://unfccc.int/resource/docs/convkp/conveng.pdf. [Accessed 24th May 2017].

[22] United Nations Framework Convention on Climate Change. Kyoto Protocol. Available online: http://unfccc.int/kyoto_protocol/items/2830.php. [Accessed 24th May 2017].

[23] United Nations Framework Convention on Climate Change. Copenhagen Climate Change Conference. Available online: http://unfccc.int/meetings/copenhagen_dec_2009/meeting/6295.php. [Accessed 24th May 2017].

[24] European Comission. Paris Agreement. Available online: https://ec.europa.eu/clima/policies/international/negotiations/paris_en. [Accessed 24th May 2017].

[25] M. S. Andersen (2010). Europe's experience with carbon-energy taxation. *SAPIENS,* vol. 3, no. 2, pp. 1-11.

[26] H. Fukui and C. Miyoshi (2017). The impact of aviation fuel tax on fuel consumption and carbon emissions: The case of the US airline industry. *Transportation Research Part D,* vol. 50, pp. 234-253.

[27] H. Dong et al. (2017). Exploring impact of carbon tax on China's CO_2 reductions and provincial disparities. *Renewable and Sustainable Energy Reviews,* vol. 77, pp. 593-603.

[28] L.-C. Liu and G. Wu (2017). The effects of carbon dioxide, methane and nitrous oxide emission taxes: An empirical study in China. *Journal of Cleaner Production,* vol. 142, pp. 1044-1054.

[29] E. I. Privalova et al. (2012). Capturing CO_2: conventional versus ionic-liquid based technologies. *Russian Chemical Reviews,* vol. 81, pp. 435-457.

[30] D. M. D'Alessandro, B. Smit and J. R. Long (2010). Carbon Dioxide Capture: Prospects for New Materials. *Angewandte Chemie International Edition,* vol. 49, pp. 6058-6082.

[31] O. M. Yaghi et al. (2003). Reticular synthesis and the design of new materials. *Nature,* vol. 423, pp. 705-714.

[32] K. Sumida et al. (2012). Carbon Dioxide Capture in Metal-Organic Frameworks. *Chemical Reviews,* vol. 112, pp. 724-781.

[33] M. Hasib-ur-Rahman, M. Siaj and F. Larachi (2010). Ionic liquids for CO_2 capture - Development and progress. *Chemical Engineering and Processing,* vol. 49, pp. 313-322.

[34] Y. Chen et al. (2011). Ionic Liquid/Metal-Organic Framework Composite for CO_2 Capture: A Computational Investigation. *The Journal of Physical Chemistry,* vol. 115, pp. 21736-21742.

[35] K. Fujie et al. (2014). Introduction of an Ionic Liquid into the Micropores of a Metal–Organic Framework and Its Anomalous Phase Behavior. *Angewandte Chemie International Edition,* vol. 53, pp. 11302-11305.

[36] I. Cota and F. F. Martinez (2017). Recent advances in the synthesis and applications of metal organic frameworks doped with ionic liquids for CO_2. *Coordination Chemistry Reviews*.

[37] P. Smirniotis and K. Gunugunuri (2015). *Water Gas Shift Reaction: Research Developments and Applications*, Elsevier.

[38] H. van Dijk et al. (2009). Performance of Water-Gas Shift Catalysts under Sorption-Enhanced Water-Gas Shift Conditions. *Energy Procedia,* vol. 1, p. 639–646.

[39] H. Jin and M. Ishida (2004). A new type of coal gas fueled chemical-looping combustion. *Fuel,* vol. 83, p. 2411–2417.

[40] N. Stylianidis et al. (2017). Chemical kinetics and CFD analysis of supercharged micro-pilot ignited dual-fuel engine combustion of syngas. *Fuel,* vol. 203, pp. 591-606.

[41] H. I. Hollander (1983). *Thesaurus on Resource Recovery Terminology*, ASTM STP 832.

[42] D. J. Williams et al. (2001). *Greenhouse Gas Control Technologies: Proceedings of the 5th International Conference on Greenhouse Gas Control Technologies*. CSIRO Publishing.

[43] J. Xu and W. Lin (2017). A CO_2 cryogenic capture system for flue gas of an LNG-fired power plant. *International Journal of Hydrogen Energy*.

[44] E. Kokkinos et al. (2017). "Study of elemental mercury removal from flue gases using Tetravalent manganese Feroxyhyte," *Chemical Engineering Journal,* vol. 315, pp. 152-158.

[45] G. Leonzio (2016). Upgrading of biogas to bio-methane with chemical absorption process: simulation and environmental impact. *Journal of Cleaner Production,* vol. 131, pp. 364-375.

[46] OECD (2010). *Bioheat, Biopower and Biogas - developments and implications for agriculture*. OECD.

[47] A. F. P. Portela (2016). Caraterização de Metal Organic Frameworks (MOFs) e Carvão Ativado como meio para purificação do Biogás – Aplicações em adsorção e permeação.

[48] R. J. R. da Costa (2011). Produção e Aplicação de Biogás.

[49] S. Sutanto et al. (2017). CO_2 removal from biogas with supported amine sorbents: First technical evaluation based on experimental data. *Separation and Purification Technology,* vol. 184, pp. 12-25.

[50] R. Chandra et al. (2011). Performance evaluation of a constant speed IC engine on CNG, methane enriched biogas and biogas. *Applied Energy,* vol. 88, pp. 3969-3977.

[51] R. W. Baker and K. Lokhandwala (2008). Natural Gas Processing with Membranes: An Overview. *Industrial & Engineering Chemistry Research,* vol. 47, pp. 2109-2121.

[52] G. Kang et al. (2017). Removal of high concentration CO_2 from natural gas using high pressure membrane contactors," *International Journal of Greenhouse Gas Control,* vol. 60, pp. 1-9.

[53] R. A. El-Nagar et al. (2017)."Investigating the efficiency of newly prepared imidazolium ionic liquids for carbon dioxide removal from natural gas. *Journal of Molecular Liquids,* vol. 237, pp. 484-489.

[54] J. Benítez (2009). *Principles and Modern Applications of Mass Transfer Operations*. Wiley.

[55] R. Smith (2005). *Chemical Process Design and Integration*. John Wiley & Sons, Ltd.

[56] R. Kirk and D. Othmer (1995). *Encyclopedia of Chemical Technology*. Volume 1. Wiley.

[57] D. C. Prieve (2001). *Unit Operations of Chemical Engineering*.

[58] R. W. Rousseau (1987). *Handbook of Separation Process Technology*. Jon Wiley & Sons.

[59] W. G. Whitman (1923). A Preliminary Experimental Confirmation of The Two-Film Theory of Gas Absorption. *Chemical and Mettalurgic Engineering ,* vol. 29, pp. 146-148.

[60] M. Althuluth et al. (2017). High pressure solubility of methane in the ionic liquid 1-hexyl-3-methylimidazolium tricyanomethanide. *The Journal of Supercritical Fluids,* vol. 128, pp. 145-148.

[61] A. A. Khan et al. (2016). Experimental investigation of sorption characteristics of capturing carbon dioxide into piperazine activated aqueous 2-amino-2-methyl-1-propanol solution in a packed column. *International Journal of Greenhouse Gas Control,* vol. 44, pp. 217-226.

[62] R. Hayes et al. (2015). Structure and Nanostructure in Ionic Liquids. *Chemical Reviews,* vol. 115, pp. 6357-6426.

[63] P. G. Jessop et al. (2005). Reversible nonpolar-to-polar solvent. *Nature,* vol. 436, p. 1102.

[64] K. Fujie et al. (2015). Low temperature ionic conductor: ionic liquid incorporated within a metal–organic framework. *Chemical Science,* vol. 6, pp. 4306-4310.

[65] K. Fujie and H. Kitagawa (2016). Ionic liquid transported into metal–organic frameworks. *Coordination Chemistry Reviews,* vol. 307, pp. 382-390.

[66] X. Zhang et al. (2012). Carbon capture with ionic liquids: overview and progress. *Energy & Environmental Science,* vol. 5, pp. 6668-6681.

[67] F. Rouquerol, J. Rouquerol and K. Sing (1999). *Adsorption by Powders*. Academic Press.

[68] J. Keller and R. Staudt (2005). *Gas Adsorption Equilibria*. Springer.

[69] R. C. Bansal and M. Goyal (2005). *Activated Carbon Adsorption*. Taylor & Francis.

[70] M. Thommes et al. (2015). Physisorption of gases, with special reference to the evaluation of surface area and pore size distribution (IUPAC Technical Report). *Pure and Applied Chemistry,* vol. 87, pp. 1051-1069.

[71] W. Zhou et al. (2011). Upgrading of Methane from Biogas by Pressure Swing Adsorption. *Advanced Materials Research,* Vols. 236-238, pp. 268-271.

[72] M. Persson (2003). *Evaluation of upgrading techniques for biogas*. Swedish Gas Center.

[73] D. Do (1998). *Adsorption analysis: equilibria and kinetics*. Imperial College Press.

[74] D. M. Ruthven (1984). *Principles of adsorption and adsorption processes*. John Wiley & Sons.

[75] R. T. Yang (2003). *Adsorbents: fundamentals and applications*. John Wiley & Sons.

[76] L. R. MacGillivray (2010). *Metal-organic frameworks: Design and Application*. John Wiley & Sons.

[77] N. R. Dhumal et al. (2016). Molecular Interactions of a Cu-Based Metal−Organic Framework with a Confined Imidazolium-Based Ionic Liquid: A Combined Density Functional Theory and Experimental Vibrational Spectroscopy Study. *The Journal of Physical Chemistry,* vol. 120, p. 3295−3304.

[78] Jenkins Group - Department of Chemistry, University of Tennessee. Breathing MOFs. Available online: https://www.chem.utk.edu/jenkins/research/MOF.html. [Accessed 6th July 2017].

[79] M. Alhamami et al. (2014). A Review on Breathing Behaviors of Metal-Organic-Frameworks (MOFs) for Gas Adsorption. *Materials,* vol. 7, pp. 3198-3250.

[80] C. R. Murdock et al. (2013). Effects of Solvation on the Framework of a Breathing Copper MOF Employing a Semirigid Linker. *Inorganic Chemistry,* vol. 52, pp. 2182-2187.

[81] A. Phan et al. (2010). Synthesis, Structure, and Carbon Dioxide Capture Properties of Zeolitic Imidazolate Frameworks. *Accounts of Chemical Research,* vol. 43, pp. 58-67.

[82] D. Danaci et al. (2015). Assessment of ZIF materials for CO_2 capture from high pressure natural gas streams. *Chemical Engineering Journal,* vol. 280, pp. 486-493.

[83] B. Chen et al. (2014). Zeolitic imidazolate framework materials: recent progress in synthesis and applications. *Journal of Materials Chemistry A,* vol. 2, pp. 16811-16831.

[84] J. M. Vicent-Luna et al. (2013). Effect of Room-Temperature Ionic Liquids on CO_2 Separation by a Cu-BTC Metal−Organic Framework. *The Journal of Physical Chemistry,* vol. 117, pp. 20762-20768.

[85] J. J. Gutiérrez-Sevillano et al. (2013). Molecular Mechanisms for Adsorption in Cu-BTC Metal Organic Framework. *The Journal of Physical Chemistry,* vol. 117, pp. 11357-11366.

[86] H. Abroshan and H. J. Kim (2015). On the structural stability of ionic liquid-IRMOF composites: a computational study. *Physical Chemistry Chemical Physics,* vol. 17, pp. 6248-6254.

[87] W. Xue et al. (2016). Effects ofionicliquiddispersioninmetal-organicframeworks and covalent organic frameworks on CO_2 capture: A computational study. *Chemical Engineering Science,* vol. 140, pp. 1-9.

[88] A. Aijaz et al. (2014). From ionic-liquid@metal–organic framework composites to heteroatom-decorated large-surface area carbons: superior CO_2 and H_2 uptake. *Chemical Communications,* vol. 50, pp. 6498-6501.

[89] F. da Silva et al. (2015). CO_2 Adsorption on Ionic Liquid–Modified Cu-BTC: Experimental and Simulation Study. *Adsorption Science & Technology,* vol. 33, pp. 223-242.

[90] F. P. Kinik et al. (2016). [BMIM][PF6] Incorporation Doubles CO_2 Selectivity of ZIF-8: Elucidation of Interactions and Their Consequences on Performance. *ACS Applied Materials & Interfaces,* vol. 8, pp. 30992-31005.

[91] K. B. Sezginel et al. (2016). Tuning the Gas Separation Performance of CuBTC by Ionic Liquid Incorporation. *Langmuir,* vol. 32, pp. 1139-1147.

[92] R. P. P. L. Ribeiro et al. (2015). Development, Construction, and Operation of a Multisample Volumetric Apparatus for the Study of Gas Adsorption Equilibrium *Journal of Chemical Education,* vol. 92, pp. 757-761.

[93] S. R. Venna and M. A. Carreon (2010). Highly Permeable Zeolite Imidazolate Framework-8 Membranes for CO_2/CH_4 Separation. *Journal of the American Chemical Society,* vol. 132, pp. 76-78.

[94] L. A. Blanchard et al. (1999). Green processing using ionic liquids and CO_2. *Nature,* vol. 399, pp. 28-29.

[95] S. M. Mahurin et al. (2010). Performance of nitrile-containing anions in task-specific ionic liquids for improved CO_2/N_2 separation. *Journal of Membrane Science,* vol. 353, pp. 177-183.

[96] W. Morris et al. (2012). NMR and X-ray Study Revealing the Rigidity of Zeolitic Imidazolate Frameworks. *The Journal of Physical Chemistry,* vol. 116, pp. 13307-13312.

[97] B. C. R. Camacho et al. (2015). Adsorption equilibrium of carbon dioxide and nitrogen on the MIL-53(Al) metal organic framework. *Separation and Purification Technology,* vol. 141, pp. 150-159.

[98] I. A. Esteves et al. (2008). Adsorption of natural gas and biogas components on activated carbon. *Separation and Purification Technology,* vol. 62, pp. 281-296.

[99] A. Portela (2017). Procedimento de realização de uma isotérmica.

[100] S. Gumma and O. Talu (2003). Gibbs Dividing Surface and Helium Adsorption. *Adsorption,* vol. 9, pp. 17-28.

[101] A. J. P. Setim (2014). Upgrade of an Experimental Volumetric Unit for Gas Adsorption Equilibrium Studies.

[102] J. A. Mason et al. (2014). Evaluating metal-organic frameworks for natural gas storage. *Chemical Science,* vol. 5, pp. 32-51.

[103] S. Gumma and O. Talu (2010). Net Adsorption: A Thermodynamic Framework for Supercritical Gas Adsorption and Storage in Porous Solids. *Langmuir,* vol. 26, pp. 17013-17023.

[104] C. Maton et al. (2013). Ionic liquid thermal stabilities: decomposition mechanisms and analysis tools. *Chemical Society Reviews,* vol. 42, pp. 5963-5977.

[105] F. Hinterholzinger et al. (2012). One-dimensional Metal-Organic Framework Photonic Crystals Used as Platforms for Vapor Sorption (Supporting Information). *Journal of Materials Chemistry,* vol. 22, pp. 10356-10362.

[106] Y. Song et al. (2015). Fabrication of fluorescent SiO_2@zeolitic imidazolate framework-8 nanosensor for Cu^{2+} detection. *Analyst,* vol. 140, pp. 623-629.

[107] M. Yurderi et al. (2014). Ruthenium(0) nanoparticles stabilized by metal-organic framework (ZIF-8): Highly efficient catalyst for the dehydrogenation ofdimethylamine-borane and transfer hydrogenation of unsaturatedhydrocarbons using dimethylamine-borane as hydrogen source. *Applied Catalysis B: Environmental,* Vols. 160-161, pp. 534-541.

[108] Michigan State University. Infrared Spectroscopy. Available online: https://www2.chemistry.msu.edu/faculty/reusch/virttxtjml/spectrpy/infrared/infrared.htm. [Accessed 29th August 2017].

[109] J. Li et al. (2014). Zeolitic Imidazolate Framework-8 with High Efficiency in Trace Arsenate Adsorption and Removal from Water. *The Journal of Physical Chemistry C,* vol. 118, pp. 27382-27387.

[110] B. H. Stuart (2004). *Infrared Spectroscopy: Fundamentals and Applications*. John Wiley & Sons.

[111] L. C. Tomé et al. (2015). Novel pyrrolidinium-based polymeric ionic liquids with cyano counter-anions: High performance membrane materials for post-combustion CO_2 separation. *Journal of Membrane Science,* vol. 483, pp. 155-165.

[112] Y. Hu et al. (2011). In situ high pressure study of ZIF-8 by FTIR spectroscopy. *Chemical Communications,* vol. 47, pp. 12694-12696.

[113] K. Hanke et al. (2015). Understanding the ionic liquid $[NC_{4111}][NTf_2]$ from individual building blocks: an IR-spectroscopic study. *Physical Chemistry Chemical Physics,* vol. 17, pp. 8518-8529.

[114] C. N. R. Rao et al. (1964). Contribution to the Infrared Spectra of Organosulphur Compounds. *Canadian Journal of Chemistry,* vol. 42, pp. 36-42.

[115] X. Wu et al. (2014). Force field for ZIF-8 flexible frameworks: atomistic simulation of adsorption, diffusion of pure gases as CH_4, H_2, CO_2 and N_2. *RSC Advances,* vol. 4, pp. 16503-16511.

[116] J. Pérez-Pellitero et al. (2010). Adsorption of CO_2, CH_4 and N_2 on Zeolitic Imidazolate Frameworks: Experiments and Simulations. *Chemistry - A European Journal,* vol. 16, pp. 1560-1571.

[117] W. Shi et al. (2014). Contribution of the Acetate Anion to CO_2 Solubility in Ionic Liquids: Theoretical Method Development and Experimental Study. *The Journal of Physical Chemistry B,* vol. 118, pp. 7383-7394.

[118] K. M. Gupta and J. Jiang (2014). Systematic Investigation of Nitrile Based Ionic Liquids for CO_2 Capture: A Combination of Molecular Simulation and ab Initio Calculation. *The Journal of Physical Chemistry C,* vol. 118, pp. 3110-3118.

7. Appendixes

7.1. Appendix A – ILs' CH_4 and CO_2 Solubilities

Table 7.1. CO_2 and CH_4 solubilities found in the open literature for the ILs used in this thesis. An asterisk (*) means the presented value was extrapolated.

		CO_2			CH_4			
IL	**Designation adopted for this thesis**	**Solubility, x_A**	**Temperature (K)**	**Pressure (bar)**	**Solubility, x_A**	**Temperature (K)**	**Pressure (bar)**	**Solubility selectivity**
[C2MIM][NTf2]	C2	0.0126	315	0.5098	0.0004	312.35	0.5268	30.1
[C10MIM][NTf2]	C10	0.0274	313.15	1	DNF	-	-	N/A
[BzMIM][NTf2]	Bz	DNF	-	-	DNF	-	-	N/A
[C2OHMIM][NTf2]	C2OH	0.0090*	313.15	0.5	0.0014	313.15	0.5286	6.4
[C6MIM][B(CN)4]	C6B(CN)4	0.0147*	313.15	0.5	0.0010*	313.16	0.5	14.0
[C6MIM][N(CN)2]	C6N(CN)2	0.1254*	313.15	0.5	DNF	-	-	N/A
[C6MIM][Cl]	C6Cl	DNF	-	-	DNF	-	-	N/A
[C2MIM][Ac]	C2Ac	0.246	298.1	0.499	DNF	-	-	N/A
[P66614][NTf2]	P66614	0.0115	315.5	0.517	0.0042*	313.3	0.5	2.7

Solubility values usually are expressed in terms of molar fraction or Henry's constant and are temperature and pressure-dependent. The latter is merely the quotient of the molar fraction and partial pressure of a given species. In here, all results are presented as molar fraction. Finally, solubility selectivity is defined as the quotient of CO_2 and CH_4 solubility. Its calculation is only applicable when both solubilities were determined at near-identical temperature and pressure conditions.

7.2. Appendix B – Experimental Protocol for IL@ZIF-8 Materials Preparation

The following protocol is divided into two parts: the first one is related to the IL and the second one is about ZIF-8.

Regarding the IL, the procedure is described below:

1. Weigh the magnetic stir bar;
2. Weigh the IL according to the calculations made beforehand;
3. Add 10 mL of acetone and quickly close the vial with an appropriate lid;
4. Stir the content of the vial for 10-15 minutes on a magnetic stirrer. The IL should dissolve easily in acetone. After that, shake manually to check if the IL is dissolved.

Concerning ZIF-8, the procedure is described below:

1. Weigh the vial;
2. Weigh the previously activated ZIF-8 stipulated on the calculations made beforehand;
3. Quickly add the content of the vial with acetone and IL to the vial containing ZIF-8, weighing the mixture without a lid closing the vial;
4. Close the vial with a lid and stir its content overnight;
5. The next day, remove the lid and stir for 4-5 hours at room temperature;
6. Heat the vial (65 °C) to promote the evaporation of the acetone until the sample looks dry. Watch out for sample loss due to stirring, especially if the MOF is a pellet or extruded;
7. Activate the sample at the required activation temperature of ZIF-8 for 3-4 hours. The activation should consist of a temperature ramp of 2 °C/min until it reaches the plateau of the degassing temperature;
8. Weigh the sample to assess the mass loss;
9. Store the sample in a desiccator for future use.

7.3. Appendix C – Weighings of ILs and ZIF-8

Table 7.2. Weighings in the manufacture of IL@ZIF-8 composite materials. Yield is the quotient between mass sample after degassing and (IL+ZIF-8) mass.

	IL + Acetone				MOF		Sample		
Sample	$m_{stirrer}$ (g)	m_{IL} (g)	$m_{acetone}$ (g)	m_{vial} (g)	m_{MOF} (g)	$m_{IL+solvent+MOF+stirrer}$ (g)	m_{vial} (g)	m_{sample} (g)[3]	Yield (%)
C2@ZIF-8	0.5856	0.1737	7.9095	12.7100	1.0000	9.4787	4.0211	1.0947	93%
C10@ZIF-8	0.5844	0.2267	7.8885	12.4564	1.0014	9.5246	4.0282	1.2125	99%
Bz@ZIF-8	0.5799	0.2072	7.9163	12.5041	1.0004	9.5401	4.1481	1.1662	97%
C2OH@ZIF-8	0.5854	0.1817	7.8321	12.7646	1.0030	9.4217	4.0994	1.1741	99%
C6B(CN)4@ZIF-8	0.5774	0.1227	7.8968	12.4524	1.0016	9.4286	4.0746	1.1198	100%
C6N(CN)2@ZIF-8	0.5715	0.1081	7.9234	12.4280	1.0006	9.3153	4.1744	1.1047	99%
C6Cl@ZIF-8	0.5826	0.0919	7.9721	12.5423	1.0008	9.4818	4.1004	1.1014	99%
C2Ac@ZIF-8	0.5761	0.0766	7.8957	12.4752	1.0004	9.3947	4.1291	1.0729	98%
P66614@ZIF-8	0.5810	0.3456	7.8210	12.5463	1.0007	9.5761	4.0843	1.3458	99%
C2OH higher loading@ZIF-8	0.5833	0.2998	7.7914	12.5520	1.0031	9.4610	4.1842	1.3452	97%
C2OH lower loading@Zlf-8	0.5763	0.0835	7.9064	12.5229	1.0099	9.4081	4.0964	1.0742	97%
C6B(CN)4 higher loading@ZIF-8	0.5795	0.1312	7.9167	12.5716	1.0028	9.4398	4.1073	1.1046	96%
C6B(CN)4 lower loading@ZIF	0.5770	0.2090	7.8957	12.4324	1.0055	9.5529	4.1533	1.1860	95%
								Average	98%

[3] After degassing.

7.4. Appendix D – Theoretical and Experimental IL Loadings

Table 7.3. Comparison between expected and experimental IL loadings.

Sample	m_{IL} (g)	Expected m_{IL} (g)	Difference (g)	m_{MOF} (g)	% of added IL	% of expected IL	Difference (%)
C2	0.1737	0.1761	-0.0024	1.0000	14.80%	15.00%	-0.17%
C10	0.2267	0.2266	0.0001	1.0014	18.50%	18.50%	-0.01%
Bz	0.2072	0.2040	0.0032	1.0004	17.20%	16.90%	0.21%
C2OH	0.1817	0.1833	-0.0016	1.0030	15.30%	15.50%	-0.15%
C6B(CN)4	0.1227	0.1270	-0.0043	1.0016	10.90%	11.30%	-0.35%
C6N(CN)2	0.1081	0.1050	0.0031	1.0006	9.80%	9.50%	0.25%
C6Cl	0.0919	0.0912	0.0007	1.0008	8.40%	8.40%	0.05%
C2Ac	0.0766	0.0766	0.0000	1.0004	7.10%	7.10%	0.00%
P66614	0.3456	0.3438	0.0018	1.0007	25.70%	25.60%	0.09%
C2OH higher loading	0.2998	0.3014	-0.0016	1.0031	23.00%	23.20%	-0.15%
C2OH lower loading	0.0835	0.0843	-0.0008	1.0099	7.60%	7.80%	-0.14%
C6B(CN)4 higher loading	0.2090	0.2088	0.0002	1.0055	17.20%	17.30%	-0.06%
C6B(CN)4 lower loading	0.0630	0.0584	0.0046	1.0002	5.90%	5.50%	0.41%
Average (g)			0.0002	1.0021			0.00%
Standard deviation (g)			0.0025	0.0028			0.21%

7.5. Appendix E – Procedure for the Making of FT-IR Tablets

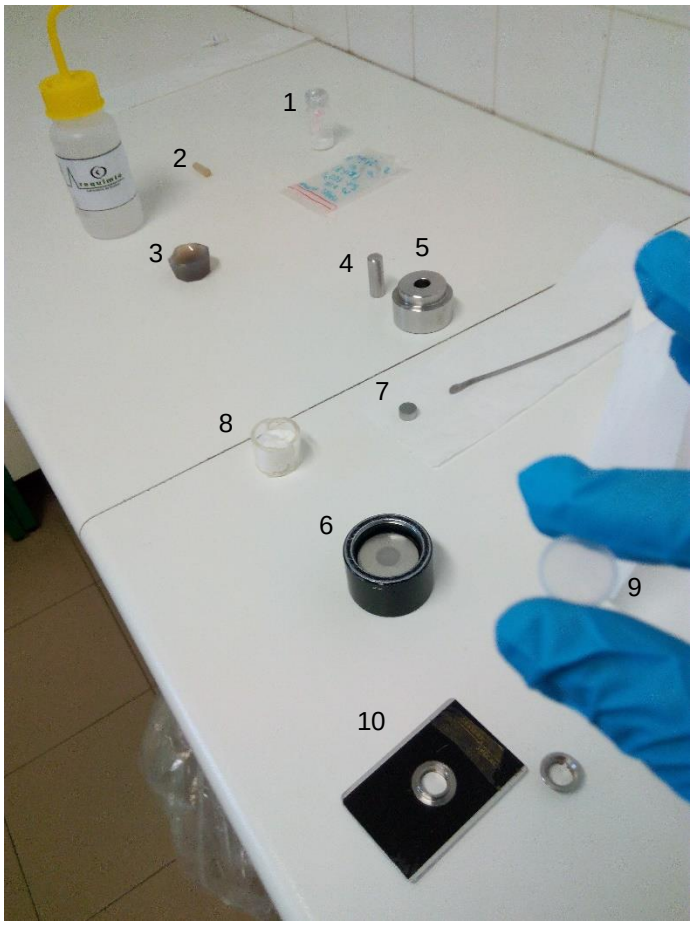

Figure 7.1. Required material for manufacture of FT-IR pellet. 1 – KBr sample; 2 – pestle; 3 – mortar; 4 – vessel cylinder; 5 – top part of vessel; 6 – bottom part of vessel; 7 – vessel disc; 8 – vessel support; 9 – FT-IR tablet; 10 – FT-IR tablet sample holder.

This procedure was followed for the manufacture of FT-IR tablets. Gloves should be used.

1. With the help of the spatula, add around two spoonsful of KBr into the the mortar, grinding into a fine powder. Next, add just a tiny amount of your sample. The desired visual proportion is about 100:1 of KBr and sample, respectively. Too much KBr is not desirable;
2. Grind again until your sample is also a fine powder. Assemble the vessel and insert the respective disc with the shiny part facing up. Add the powder to the vessel and insert the cylinder, grinding again the powder with it;
3. With the help of a hydraulic press, the top of the cylinder is pressed for 5 minutes at around 10-ton load;
4. Afterwards, the FT-IR should fall. If not, disassemble the top and bottom part and insert the plastic support in between. Use again the press to force the cylinder downwards and the tablet should fall;
5. Introduce the tablet inside the sample holder without touching with your hands, as results can then be compromised. Use the appropriate software for IR spectrum obtention.

7.6. Appendix F – Calibration Procedure for Volumetric/Manometric Apparatus

This calibration is related to the volumetric apparatus indicated in Figure 3.3.; the calibration experimental procedure will be presented, while the calculations in order to obtain the calibrated volumes will not. He (≥99.999% purity, Air Liquide) was used for this process since it is a small and light gas.

There are two types of calibration: one is related to the apparatus lines' volumes and another is made for the cells (to determine the cell volumes).

Lines' volumes cannot be calibrated at the same time, though calibration follows the same procedure for both volumes. A step-by-step calibration method will be presented for Line 1; this means pressure and temperature will be measured by pressure and temperature transducers of Line 2. The experimental procedure is as it follows:

1. Create vacuum inside the whole unit with Valves V_0, V_2, V_3, V_4, V_5, V_6, V_7 and V_9 opened for 15 minutes for system stabilization and register the temperature;
2. Since the procedure is for Line 1, close valves V_2, V_3, V_4 and V_7;
3. Stop the vacuum by closing valve V_9. Purge the system with He by closing valve V_5, opening valve V_1 and then valve V_8, keep the gas supply opened. Close valves V_8 and V_1 along with the gas supply;
4. Open valves V_5 and the V_6; the latter needs to be opened in order to check the temperature. By opening valve V_1, a gas inlet will occur. The desired pressure is about 15-18 bar, just enough to guarantee high pressure inside the apparatus. Close valve V_1 and wait for 15. Write down the temperature value;
5. Close valve V_0 and create vacuum inside the unit for 15 minutes, through the opening of valve V_9. Pressure inside the system is now only contained between the cylinder volume and the valve V_0;
6. After the mentioned 15 minutes of vacuum, open valve V_0 and gas will expand to the volume contained by valves V_0, V_1, V_2, V_7, V_8 and V_9. Wait 15 minutes and register the temperature value;
7. After that time, close valve V_0 and open valve V_2. This way gas will expand to a volume contained by valve V_2, V_3 and V_4. Wait 15 minutes and write down the temperature;
8. Open valve V_3, wait for 15 minutes and record the temperature value.
9. Open valve V_4, wait for 15 minutes and register the temperature value.

Pressures for posterior calculations can be obtained as averages of the pressure values obtained during the 15 minutes, when the system is stabilizing, for every volume expansion.

In order to try and find the most precise and accurate calibrated volumes, the procedure should be done at least five times.

Cell volume calibrations can be done simultaneously. The experimental procedure is as it follows:

1. Create vacuum inside the whole unit with Valves V_0, V_2, V_3, V_4, V_5, V_6, V_7 and V_9 opened for 15 minutes for system stabilization and register the temperature;
2. Close valve V_9 and afterwards valves V_2, V_4, V_5 and V_7. Purge the system with He by opening valves V_1 and V_8, with the gas supply opened. Then, close both valves as well as the gas supply;
3. Open valves V_2 and V_5. Then, open valve V_1 for gas inlet at 15-18 bar, just enough pressure to guarantee high pressure inside the apparatus. Wait 15 minutes and then write down the temperature value;
4. Open valves V_4 and V_7. This will expand the gas to the inside of the cells. Wait 15 minutes and register the temperature.

Pressures for posterior calculations can be obtained as averages of the pressure values obtained during the 15 minutes, when the system is stabilizing, for every volume expansion.

In order to try and find the most precise and accurate calibrated cell volumes, the procedure should be done at least five times.

7.7. Appendix G – Volumetric/Manometric Procedure for Adsorption Equilibrium Measurements

The procedure for measuring using the volumetric unit presented in Figure 3.3., considering the use of both cells, is as follows:

1. Weigh both cells without any kind of sample;
2. Add the samples to the cells and weigh again. The mass difference between this and the previous weighing is the mass sample. Test for gas leaks with He.
3. Since samples can contain impurities and/or moisture, a compulsory degassing step is performed. A 2 °C/min ramp is defined until a temperature plateau is achieved, corresponding to the degassing temperature of the material. This value can be retrieved from TGA data. This plateau should last between 3-4 hours, under vacuum. So, valves V_2, V_3, V_4, V_5, V_6, V_7 and V_9 must be open;
4. After degassing, the cells are weighed to assess the mass;
5. Define the desired temperature for adsorption measurement that should only start after the cells are guaranteed to be at room temperature or below the defined temperature;
6. After ensure both cells are at the defined temperature (give 2-3 hours, under vacuum, for this), measurements can be started. With valves V_2, V_3, V_4, V_5, V_6, V_7 and V_9, register the temperature value (this is called point 0). Every point has a reference volume temperature and cell temperature according to the calculations. Pressure values should be considered as averages of the registered pressures for 10 minutes. The file created by the pressure recording software can be opened with *Microsoft Excel*;
7. Close valve V_9 and, afterwards, valves V_2, V_4, V_5 and V_7. Purge the system by opening valves V_1 and V_8, with the gas supply open. Close these valves as well as the gas supply.
8. Open valves V_2 and V_5. Pressure will increase and then, by controlling valve V_1 gas inlet, administer the required pressure. Keep in mind that, for instances, if want to measure adsorption at 0.5 bar you should insert a higher pressure than that on the reference volume since, when gas is allowed inside the cells, pressure will drop. For desorption, insert a lower pressure and, when gas enters the cells, the pressure will increase. Close valves V_2 and V_5;
9. The system will stabilize for around 10 minutes. Register the reference volume temperatures and open valves V_4 and V_7. Let the system stabilize at least 1 hour. After that, every 10 minutes, register the cell volume temperature and calculate the pressure averages. When the last temperature value and pressure average is equal to the previously 10 minutes-collected values, the system is considered in adsorption equilibrium;
10. Close valves V_4 and V_7. Repeat steps 7. through 9. for higher pressures, beginning with the gas purge and valves V_2 and V5 closed. Desorption measurements are similar to the adsorption ones but don't require gas purge. To release pressure open and later close V_8 to the desired value.

7.8. Appendix H - Gravimetric Procedure for Adsorption Equilibrium Measurements

While the apparatus is different (see Figure 3.9.), the procedure for gravimetric adsorption equilibrium measurements partly follows the volumetric/manometric one as is as follows:

1. Add the samples to the sample holders and weigh;
2. The apparatus must be 'closed' and tested for gas leak with He;
3. Since samples can contain impurities and/or moisture, a compulsory degassing step is performed. If the sample's degassing temperature is up to 100 °C (like ZIF-8 and its composites), it can be done inside the apparatus and under vacuum. Since temperature can be controlled, set points are defined until it reaches the degassing temperature. As an examples, set points of 60, 75, 85 and 100 °C can be defined, this way preventing violent and quick temperature sample variation. If the degassing temperature is over the referred 100 °C, degassing is made externally and, resourcing to helium-filled plastic bags, sample holders are incorporated into the apparatus. Only then can it be 'closed' and tested for gas leaks;
4. Define as set point the temperature of the adsorption equilibrium measurement. Keep in mind that the temperature variation of the samples can't be abrupt. Since the system at this point is under vacuum, the first mass, temperature and pressure registered values are for point 0. The software can be used to obtain a pressure average;
5. Purge the system and increase the pressure until the desired pressure. Keep in mind the maximum pressure reading of each sensor. Leave the system stabilizing at least 1 hour. Write down the mass, temperature and pressure values. Check every 10 minutes and when these variables don't change, register them and proceed to the next experimental point by repeating this step.
6. When in the desorption branch, open the exhaustion valve for releasing pressure. Once again keep in mind the maximum pressure reading of each sensor.

7.9. Appendix I – Pure ILs' Densities

Table 7.4. ILs densities between 5-100 °C. An asterisk (*) denotes an extrapolated value. Data retrieved from the Ionic Liquids Database - ILThermo.

Temperature (°C)	$[C_2MIM][NTf_2]$	$[C_{10}MIM][NTf_2]$	$[BzMIM][NTf_2]$	$[C_2OHMIM][NTf_2]$	$[C_6MIM][B(CN)_4]$	$[C_6MIM][N(CN)_2]$	$[C_6MIM][Cl]$	$[C_2MIM][Ac]$	$[P_{66614}][NTf_2]$
5	-	-	1.512	-	1.005	1.042	-	1.112	-
10	-	-	1.508	1.589	1.002	1.038	-	1.109	1.077
15	-	-	1.503	1.584	0.998	1.035	-	1.106	-
20	1.526	1.282	1.498	1.579	0.995	1.032	1.044	1.102	1.070
25	-	1.278	1.493	1.574	0.991	1.029	1.041	1.099	-
30	1.514	1.274	1.488	1.569	0.987	1.026	1.038	1.096	1.063
35	-	-	1.483	1.564	0.984	1.023	1.035	1.094	-
40	1.503	1.265	1.478	1.559	0.980	1.020	1.032	1.090	1.055
45	-	-	1.473	1.554	0.977	1.017	1.030	1.087	-
50	1.493	-	1.468	1.549	0.973	1.014	1.027	1.084	1.048
55	-	-	-	1.545	0.970	1.011	1.024	1.081	-
60	1.482	1.246	1.457*	1.540	0.966	1.008	1.021	1.078	1.041
65	-	-	-	1.535	0.963	1.005	1.018	1.075	-
70	1.472	-	-	1.530	0.959	1.002	1.016	1.072	-
75	-	-	-	1.526	0.956	0.999	1.013	1.069	-
80	1.461	1.229	-	1.521	0.952	0.996	1.010	1.066	-
85	-	-	-	-	0.949	0.993	1.007	1.063	-
90	-	-	-	-	0.946	0.990	1.004	1.061	-
100	-	1.210	-	-	-	-	-	-	-

7.10. Appendix J – He Pycnometry Data

Firstly, a blank measurement was made in order to obtain the sample holders' mass and volume. The obtained values are shown in Table 7.5.

Table 7.5. Sample holders' mass and volume (gravimetric unit).

	Sample holder 1	Sample holder 2
Mass (g)	5.35086	6.32864
Volume (cm^3)	0.68146	0.80339

Only afterwards He pycnometry samples' measurements can be performed. Tables through this appendix contain the collected data, while figures show apparent mass as a function of pressure as well as He density. The included trendline is relative only to adsorption points.

- C2@ZIF-8

Temperature (°C)	Pressure (bar)	Apparent mass (g)	Helium density (kg/m^3)
59.92	0.00000	5.71216	0.0000
60.33	0.50830	5.71209	0.0734
60.22	1.51578	5.71196	0.2188
60.24	7.50413	5.71117	1.0803
60.12	14.46752	5.71024	2.0777
60.02	25.00963	5.70883	3.5774
59.94	31.96040	5.70789	4.5599
59.99	28.51638	5.70832	4.0736
60.11	21.00742	5.70931	3.0090
60.16	16.95403	5.70987	2.4320
60.17	10.01167	5.71081	1.4401
60.20	4.43331	5.71154	0.6391
60.11	0.20050	5.71211	0.0290

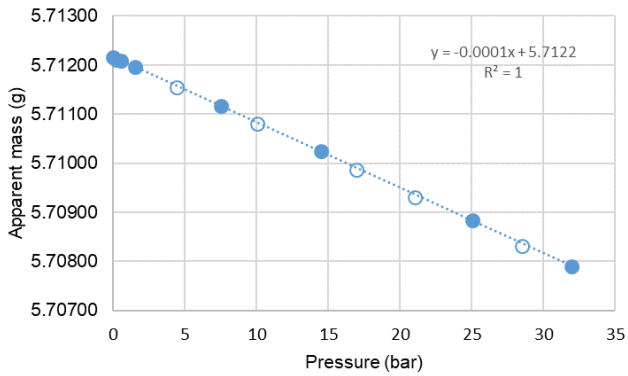

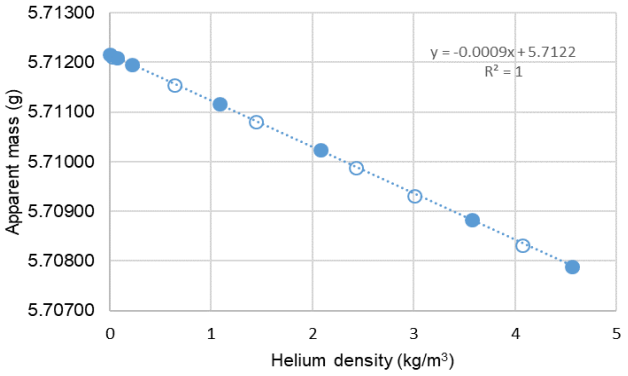

- C10@ZIF-8

Temperature (°C)	Pressure (bar)	Apparent mass (g)	Helium density (kg/m^3)
59.92	0.00080	6.68995	0.0000
60.33	0.50830	6.68985	0.0734
60.22	1.51578	6.68974	0.2188
60.24	7.50413	6.68881	1.0803
60.12	14.46752	6.68773	2.0777
60.02	25.00963	6.68609	3.5774
59.94	31.96040	6.68503	4.5599
59.99	28.51638	6.68557	4.0736
60.11	21.00742	6.68674	3.0090
60.16	16.95403	6.68733	2.4320
60.17	10.01167	6.68839	1.4401
60.20	4.43331	6.68928	0.6391
60.11	0.20050	6.68985	0.0290

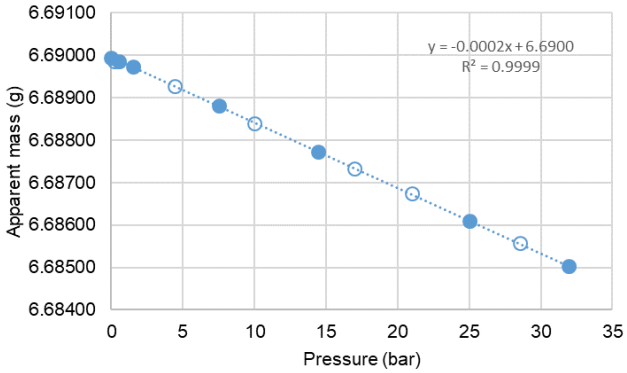

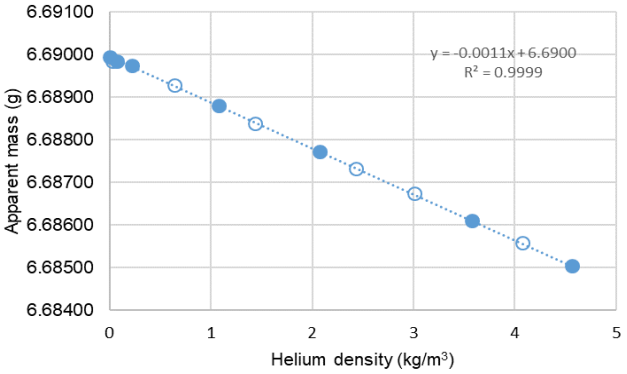

- Bz@ZIF-8

Temperature (°C)	Pressure (bar)	Apparent mass (g)	Helium density (kg/m^3)
59.99	0.00000	5.68811	0.0000
60.26	0.50020	5.68805	0.0722
60.15	1.50509	5.68790	0.2173
60.13	7.53482	5.68711	1.0851
60.01	14.46239	5.68621	2.0776
59.98	24.87349	5.68489	3.5585
59.89	32.52420	5.68394	4.6400
60.04	28.49845	5.68444	4.0705
60.12	20.75734	5.68540	2.9734
60.10	17.13061	5.68590	2.4576
60.04	10.99521	5.68666	1.5816
60.06	4.43989	5.68755	0.6403
60.07	0.20250	5.68806	0.0293

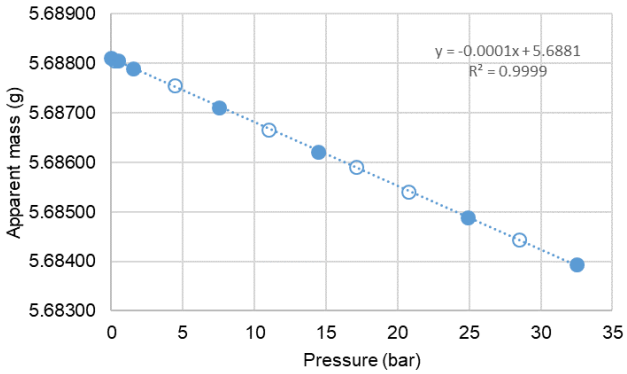

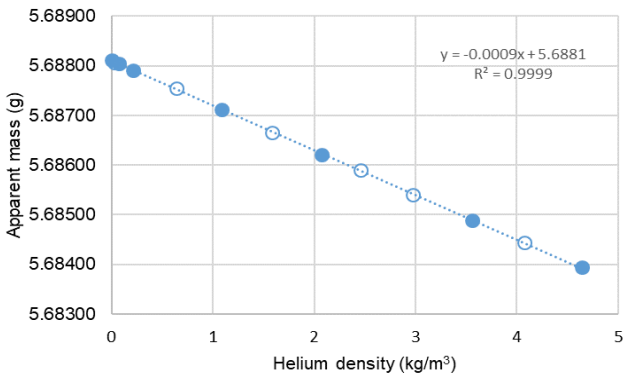

- C2OH@ZIF-8

Temperature (°C)	Pressure (bar)	Apparent mass (g)	Helium density (kg/m^3)
59.78	0.00000	5.71092	0.0000
60.33	0.50190	5.71091	0.0724
60.25	1.50815	5.71076	0.2176
60.09	7.60961	5.70996	1.0959
60.17	14.51049	5.70904	2.0835
60.00	25.21220	5.70762	3.6063
59.92	32.53013	5.70663	4.6404
60.00	29.29710	5.70708	4.1837
60.13	16.75643	5.70873	2.4041
60.15	10.59724	5.70956	1.5241
60.12	4.01916	5.71042	0.5796
60.16	0.63880	5.71083	0.0922
60.12	0.14980	5.71091	0.0216

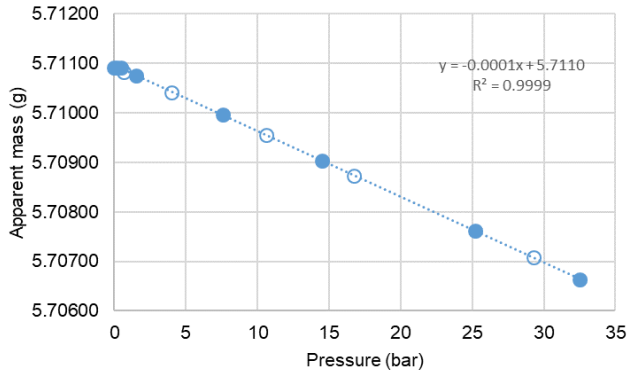

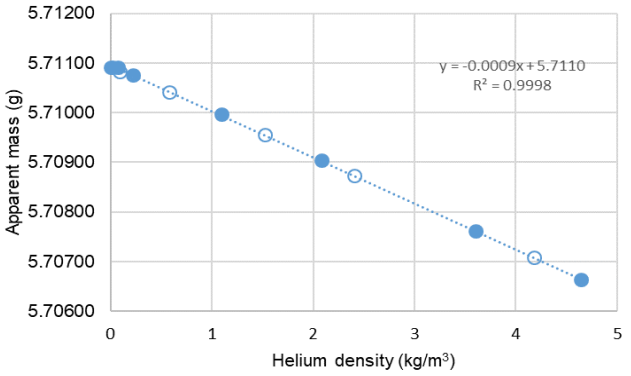

- C6B(CN)4@ZIF-8

Temperature (°C)	Pressure (bar)	Apparent mass (g)	Helium density (kg/m^3)
59.99	0.00000	6.65811	0.0000
60.26	0.50020	6.65804	0.0722
60.15	1.50509	6.65795	0.2173
60.13	7.53482	6.65702	1.0851
60.01	14.46239	6.65590	2.0776
59.98	24.87349	6.65437	3.5585
59.89	32.52420	6.65318	4.6400
60.04	28.49845	6.65376	4.0705
60.12	20.75734	6.65497	2.9734
60.10	17.13061	6.65550	2.4576
60.04	10.99521	6.65639	1.5816
60.06	4.43989	6.65735	0.6403
60.07	0.20250	6.65798	0.0293

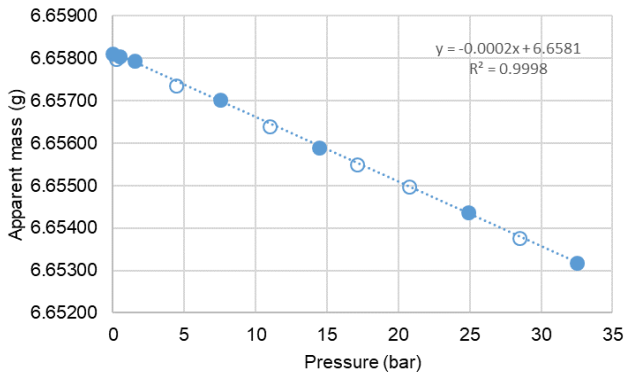

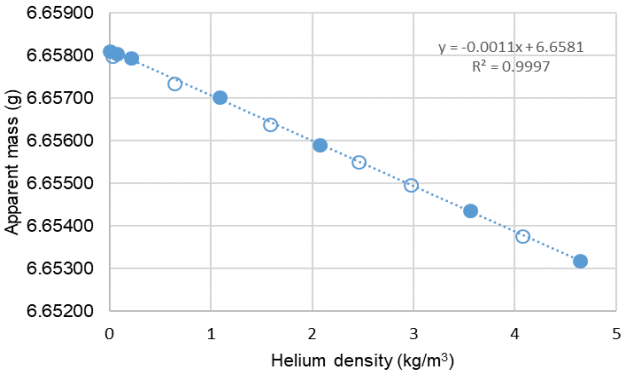

- C6N(CN)2@ZIF-8

Temperature (°C)	Pressure (bar)	Apparent mass (g)	Helium density (kg/m^3)
59.93	0.00000	5.73024	0.0000
60.15	0.50030	5.73021	0.0722
60.12	1.57326	5.73007	0.2271
60.08	7.60540	5.72925	1.0954
60.04	14.64374	5.72830	2.1033
59.95	24.96167	5.72688	3.5714
59.98	32.39708	5.72587	4.6209
60.03	28.40037	5.72642	4.0568
60.06	20.96848	5.72745	3.0039
60.08	16.95511	5.72798	2.4327
60.08	10.83089	5.72880	1.5579
60.08	4.49657	5.72967	0.6484
60.02	0.19970	5.73019	0.0289

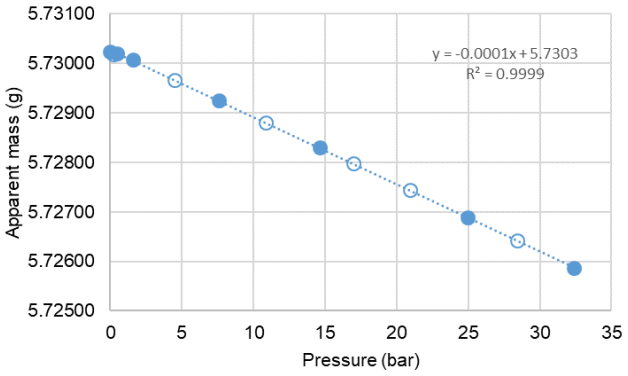

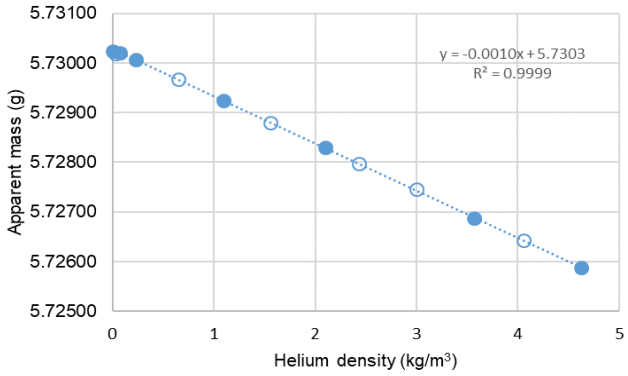

- C6Cl@ZIF-8

Temperature (°C)	Pressure (bar)	Apparent mass (g)	Helium density (kg/m^3)
59.93	0.00000	6.64043	0.0000
60.15	0.50030	6.64043	0.0722
60.12	1.57326	6.64031	0.2271
60.08	7.60540	6.63940	1.0954
60.04	14.64374	6.63835	2.1033
59.95	24.96167	6.63686	3.5714
59.98	32.39708	6.63586	4.6209
60.03	28.40037	6.63641	4.0568
60.06	20.96848	6.63746	3.0039
60.08	16.95511	6.63804	2.4327
60.08	10.83089	6.63893	1.5579
60.08	4.49657	6.63985	0.6484
60.02	0.19970	6.64043	0.0289

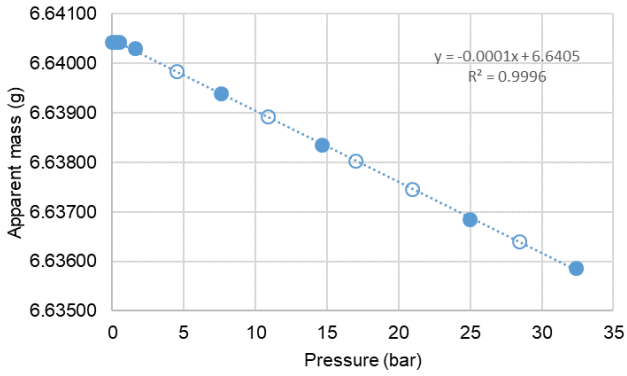

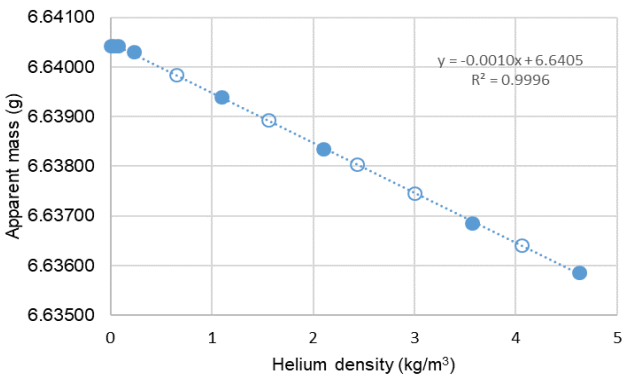

- C2Ac@ZIF-8

Temperature (°C)	Pressure (bar)	Apparent mass (g)	Helium density (kg/m^3)
59.92	0.00000	5.66175	0.0000
60.03	0.51470	5.66173	0.0744
60.00	1.41667	5.66163	0.2046
59.97	7.54790	5.66084	1.0875
60.03	14.58325	5.65991	2.0947
59.88	25.06091	5.65856	3.5862
59.85	32.50982	5.65762	4.6385
59.91	27.17891	5.65831	3.8856
60.09	19.68480	5.65928	2.8212
60.19	14.40681	5.65998	2.0686
60.18	10.89498	5.66044	1.5666
60.13	4.55773	5.66127	0.6571
60.13	0.19980	5.66179	0.0289

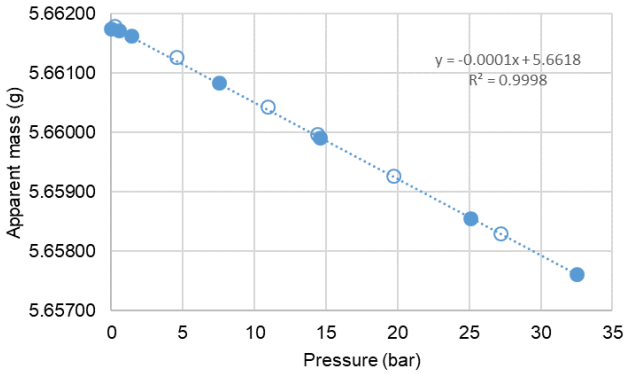

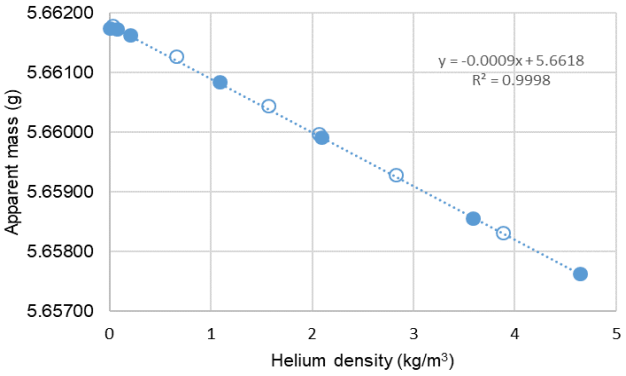

- P66614@ZIF-8

Temperature (°C)	Pressure (bar)	Apparent mass (g)	Helium density (kg/m^3)
59.92	0.00000	6.62488	0.0000
60.03	0.51470	6.62485	0.0744
60.00	1.41667	6.62473	0.2046
59.97	7.54790	6.62381	1.0875
60.03	14.58325	6.62275	2.0947
59.88	25.06091	6.62119	3.5862
59.85	32.50982	6.62009	4.6385
59.91	27.17891	6.62088	3.8856
60.09	19.68480	6.62198	2.8212
60.19	14.40681	6.62277	2.0686
60.18	10.89498	6.62329	1.5666
60.13	4.55773	6.62426	0.6571
60.13	0.19980	6.62487	0.0289

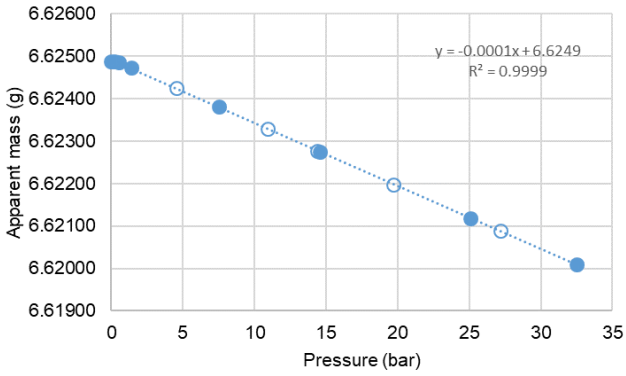

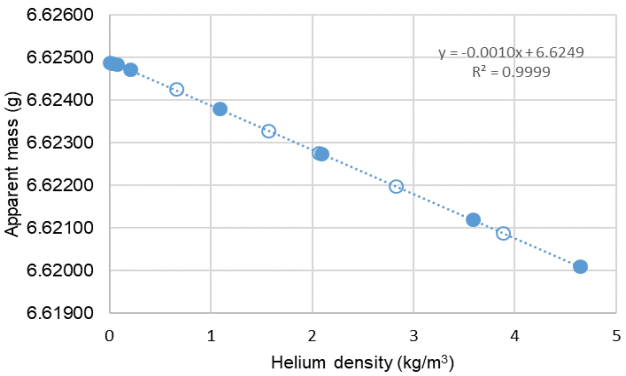

- C2OH@ZIF-8 higher loading

Temperature (°C)	Pressure (bar)	Apparent mass (g)	Helium density (kg/m^3)
59.87	0.00000	5.68068	0.0000
60.29	0.50040	5.68061	0.0722
60.10	1.75391	5.68040	0.2532
60.08	7.49411	5.67968	1.0794
60.01	14.50130	5.67881	2.0832
60.00	25.12439	5.67740	3.5939
59.93	32.51153	5.67643	4.6377
59.92	28.60263	5.67692	4.0866
60.02	21.02144	5.67791	3.0118
60.05	16.93374	5.67847	2.4299
60.17	10.98780	5.67922	1.5799
60.07	4.50466	5.68002	0.6496
60.05	0.20010	5.68057	0.0289

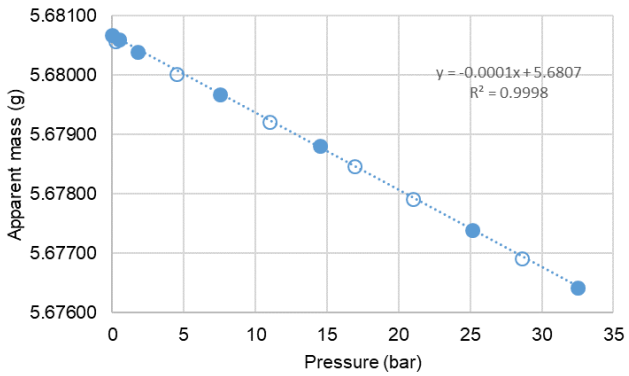

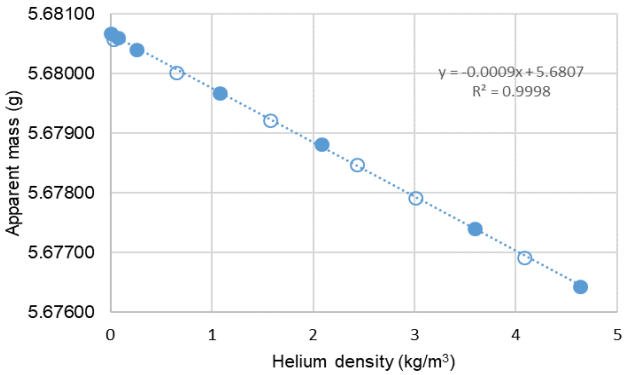

- C2OH@ZIF-8 lower loading

Temperature (°C)	Pressure (bar)	Apparent mass (g)	Helium density (kg/m^3)
59.87	0.00000	6.65799	0.0000
60.29	0.50040	6.65794	0.0722
60.10	1.75391	6.65773	0.2532
60.08	7.49411	6.65692	1.0794
60.01	14.50130	6.65583	2.0832
60.00	25.12439	6.65425	3.5939
59.93	32.51153	6.65316	4.6377
59.92	28.60263	6.65373	4.0866
60.02	21.02144	6.65486	3.0118
60.05	16.93374	6.65544	2.4299
60.17	10.98780	6.65631	1.5799
60.07	4.50466	6.65725	0.6496
60.05	0.20010	6.65787	0.0289

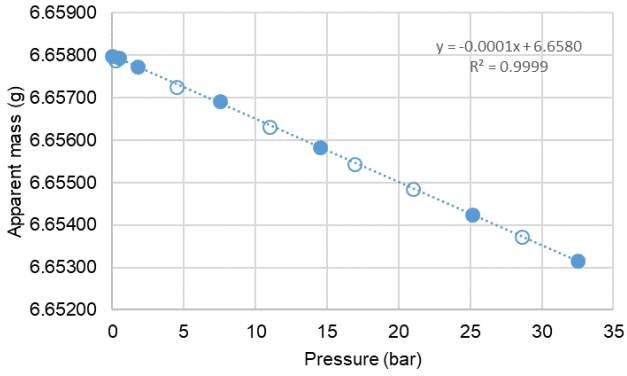

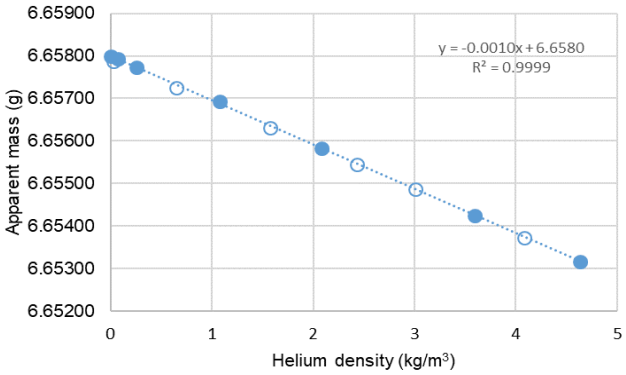

- C6B(CN)4@ZIF-8 higher loading

Temperature (°C)	Pressure (bar)	Apparent mass (g)	Helium density (kg/m^3)
60.00	0.00000	5.68818	0.0000
60.07	1.64856	5.68813	0.2380
60.10	7.53311	5.68734	1.0849
60.07	14.84062	5.68633	2.1312
59.98	24.83609	5.68499	3.5532
59.84	32.47882	5.68391	4.6343
59.99	28.49997	5.68451	4.0713
60.10	18.55194	5.68583	2.6600
60.11	11.87382	5.68673	1.7070
60.08	8.96519	5.68712	1.2905
60.09	4.47359	5.68769	0.6451
60.06	0.50180	5.68820	0.0725
60.05	0.20450	5.68823	0.0295

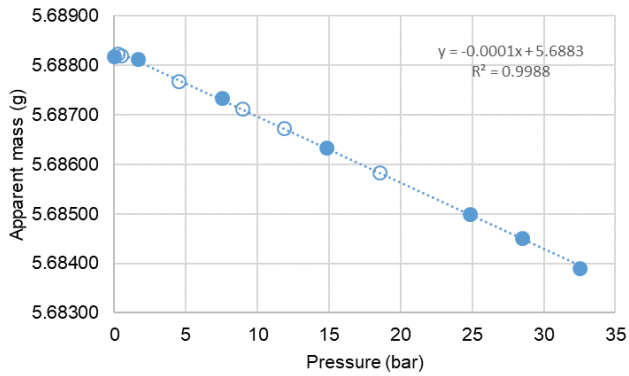

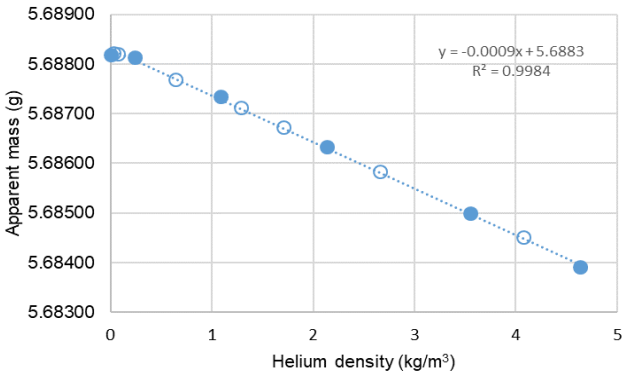

- C6B(CN)4@ZIF-8 lower loading

Temperature (°C)	Pressure (bar)	Apparent mass (g)	Helium density (kg/m^3)
60.00	0.00000	6.65772	0.0000
60.07	1.64856	6.65751	0.2380
60.10	7.53311	6.65664	1.0849
60.07	14.84062	6.65554	2.1312
59.98	24.83609	6.65406	3.5532
59.84	32.47882	6.65291	4.6343
59.99	28.49997	6.65346	4.0713
60.10	18.55194	6.65495	2.6600
60.11	11.87382	6.65592	1.7070
60.08	8.96519	6.65640	1.2905
60.09	4.47359	6.65709	0.6451
60.06	0.50180	6.65761	0.0725
60.05	0.20450	6.65766	0.0295

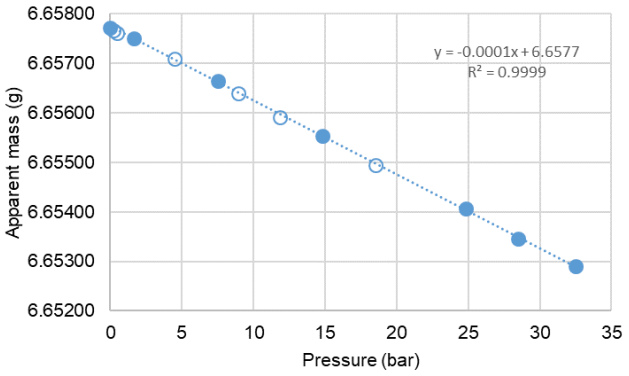

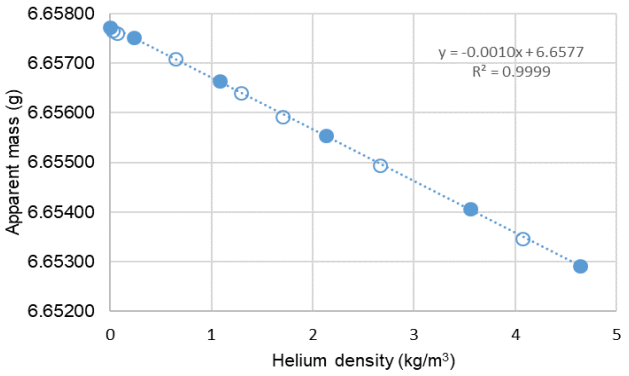

A *y=mx+b* linear equation is expected when plotting the apparent mass as a function of the helium density. The intercept value is the sample mass while the slope value is the sample volume. A mere quotient is then enough to obtain the solid matrix density.

Table 7.6. contains the solid matrix density for every IL@ZIF-8 manufactured composites.

Table 7.6. Solid matrix densities obtained for IL@ZIF-8 composites.

Sample	Sample mass (g)	Sample volume (cm^3)	Sample solid matrix density (g/cm^3)
C2@ZIF-8	0.36130	0.26	1.41
C10@ZIF-8	0.36130	0.27	1.34
Bz@ZIF-8	0.33724	0.22	1.54
C2OH@ZIF-8	0.36009	0.24	1.48
C6B(CN)4@ZIF-8	0.32945	0.25	1.29
C6N(CN)2@ZIF-8	0.37941	0.26	1.43
C6Cl@ZIF-8	0.31184	0.20	1.54
C2Ac@ZIF-8	0.31095	0.22	1.42
P66614@ZIF-8	0.29628	0.24	1.25
C2OH@ZIF-8 higher loading	0.32979	0.23	1.46
C2OH@ZIF-8 lower loading	0.32933	0.23	1.41
C6B(CN)4@ZIF-8 higher loading	0.33743	0.25	1.35
C6B(CN)4@ZIF-8 lower loading	0.32908	0.24	1.39

7.11. Appendix K – ^{1}H and ^{13}C NMR Spectra for $[C_6MIM][B(CN)_4]$

^{1}H NMR in Dmso

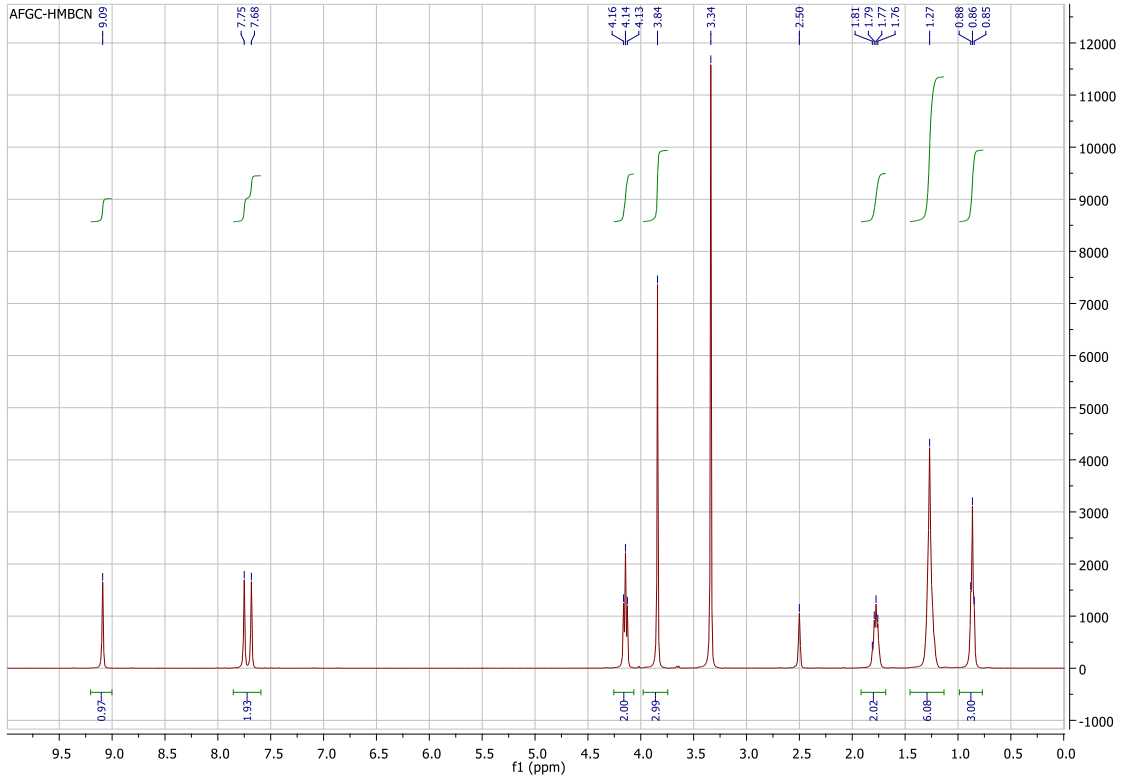

^{13}C NMR in Dmso